

Developing new nano-structures for SERS and its applications in small molecule binding in proteins and plasmonic enhancement in solar cell efficiency

A thesis submitted for the partial fulfillment
for the degree of
MASTER OF SCIENCE
as a part of the
Integrated Ph. D. programme
(Materials Science)

by

SHANTANU AGGARWAL



CHEMISTRY AND PHYSICS OF MATERIALS UNIT
JAWAHARLAL NEHRU CENTRE FOR ADVANCED SCIENTIFIC
RESEARCH
(A Deemed University)
Bangalore – 560 064

MARCH 2015

DECLARATION

I hereby declare that the matter embodied in the thesis entitled “**Developing new nano-structures for SERS and its applications in small molecule binding in proteins and plasmonic enhancement in solar cell efficiency**” is the result of investigations carried out by me at the Chemistry and Physics of Materials Unit, Jawaharlal Nehru Centre for Advanced Scientific Research, Bangalore, India under the supervision of Prof. Chandrabhas Narayana and that it has not been submitted elsewhere for the award of any degree or diploma.

In keeping with the general practice in reporting scientific observations, due acknowledgment has been made whenever the work described is based on the findings of other investigators.

Shantanu Aggarwal

CERTIFICATE

I hereby certify that the matter embodied in this thesis entitled “**Developing new nano-structures for SERS and its applications in small molecule binding in proteins and plasmonic enhancement in solar cell efficiency**” has been carried out by Mr. Shantanu Aggarwal at the Chemistry and Physics of Materials Unit, Jawaharlal Nehru Centre for Advanced Scientific Research, Bangalore, India under my supervision and that it has not been submitted elsewhere for the award of any degree or diploma.

Prof. Chandrabhas Narayana
(Research Supervisor)

Contents

Preface	3
1 Introduction	7
1.1 Raman scattering	9
1.1.1 Classical picture of Raman scattering	10
1.1.2 Quantum picture of Raman scattering	12
1.2 Surface Enhanced Raman Scattering(SERS)	14
1.2.1 Electromagnetic enhancement mechanism	15
1.2.2 Chemical enhancement mechanism	17
1.2.3 Experimental calculation of SERS enhancement factor	18
1.3 Secondary structure of proteins	19
1.4 Raman spectroscopy of proteins	22
1.5 SERS of proteins	25
2 Experimental Techniques	29
2.1 Instrumentation	29
2.2 Spectral Measurements	31
2.3 Calibration of Raman spectra	33
2.4 Analysis of Raman spectra	33
2.5 Acquiring SERS spectra from Proteins	34
2.6 Temperature dependent measurements	39
3 Plasmonic Nanocermetes as a versatile SERS sensors	41
3.1 Introduction	41
3.2 Experimental methods	43
3.3 Results and Discussions	49
3.4 Conclusions	62
4 Surface enhanced Raman spectroscopic insights into an interaction of serum albumins with dihydropyridine based hypertensive drugs	65
4.1 Introduction	65
4.2 Experimental methods	67
4.3 Results and Discussions	69

4.4	Conclusions	83
5	Surface enhanced Raman spectroscopy of Restriction Enzyme R-Kpn1	85
5.1	Introduction	85
5.2	Experimental methods	86
5.3	Results and Discussions	88
5.4	Conclusions	102
6	Plasmonic Features of Low temperature melting alloys in Organic Solar Cells	105
6.1	Introduction	105
6.2	Experimental Methods	108
6.3	Results and Discussions	110
6.4	Conclusions	118
7	Outlook	119
	References	121

Acknowledgments

I would like to extend my sincere gratitude to my mentor and guide Prof. Chandrabhas Narayana, who has been a constant source of inspiration for me. His guidance and support have enabled me to develop a detailed understanding in the subject. I am grateful to him for providing me enormous freedom at the workplace.

I would like to acknowledge Prof. C. N. R. Rao for being a huge source of inspiration. I feel very fortunate to be able to listen to his inspirational talks.

I am thankful to the Chairman of our unit, Prof Balasubramanian, for his guidance during the course work.

I thank all my teachers in JNC, Prof. Bala, Prof. Kulkarni, Prof. Maji, Prof. Eswaramoorthy, Prof. Waghmare, Prof. Sundaresan, Prof. Narayan, Prof. Shobhana, Prof. Shivaprasad, Prof. Aloknath, Dr. Vidyadhiraja, Dr. Ranjan Dutta, Dr. Shridhar Rajaram, Dr. Rajesh Ganapathy, and all the NCU faculty for their valuable coursework and guidance.

I would also like to acknowledge my collaborators Prof. Harish C Barshilia (NAL), Prof. K.S. Narayan, Prof. V. Nagaraja, Prof. Kundu, Nitant, Disha, Malli, Prashant, Dr. Karthigeyan and Arnab. It has been a pleasure to work and learn from them.

I would like thank Integrated Ph.D. coordinators Prof. Maji.

The technical staff in JNC have been very helpful. Special thanks to Vasu and

Usha madam. I would also like to thank all the admin and support staff of JNC.

I learnt a lot from my labmates Dr. Soumik, Dr. Srinu, Dr.Partha, Gayatri, Dhanya, Rajaji, Jyoti, Dr. Sorb, Priyank. I feel privileged to have such a wonderful group.

I would also like to thank my classmates Shivakumar, Vikas, Sohini, Promit, Kushagra, Ananya M, Rajkumar and Ananya B with whom I have spent most of my time and who have made my stay here quite enjoyable. I also thank all my friends in JNC Raagesh, Debanjan, Krishnamohan and Varun and friends in college Nikhil, Aman, Aditya, Siddharth and Diptendera.

I thank my Mother, Father and Amma (Grandmother) for their encouragement, love and support. I am deeply thankful to my cousin sister Neha.

Preface

Recent advances in the field of optical technology and nano fabrication have led to development of new techniques using Raman spectroscopy. Surface enhanced raman scattering and Tip enhanced Raman scattering are two such techniques. This thesis Surface enhanced Raman scattering (SERS) in most of the experiments.. One of the foremost advantages of SERS is the rich blend of high sensitivity and chemical imaging capability, which vastly caters to the needs of ultra trace analysis of molecules. Strategies for SERS detection can be optimized by harnessing the electromagnetic and chemical enhancement mechanisms of SERS. This thesis have been divided in the following chapters:

Chapter 1 provides an introduction to Raman spectroscopy and surface enhanced Raman spectroscopy (SERS) and methodologies related to it. **Chapter 2** accounts the details of the design and construction of custom-built Raman microscopy system compatible for SERS measurements and sample preparation for a SERS experiment. **Chapter 3** describes a fabrication of a SERS sensor. Silicon can be chemically etched to form micro pyramids. These micro pyramids leads to optical phenomenon of light trapping and promotes enhancement of local electric field. A layer of silicon nitride with silver nanoparticles was deposited to fabricate a Nanocermet based sensor. This sensor is stable under harsh environment and can be used for multianalyte detection. **Chapter 4** describes the interaction of two antidepressant drugs, amlodipine and nimodipine, with two proteins, Human

serum albumin (HSA) and Bovine Serum Albumin (BSA). These two proteins are structurally very similar. SERS has been used to study their structural similarity and predicting the nature of binding with the two drugs. Docking studies were also done to support SERS experimental data. In **Chapter 5**, structure of a restriction enzyme, Kpn1, has been studied with help of SERS. Kpn1 is activated by metal ions belonging to both the alkaline earth and transition groups. The enzyme exhibits promiscuous activity with Mg^{2+} , Mn^{2+} and Co^{2+} while other Ca^{2+} , Cd^{2+} , Ni^{2+} and Zn^{2+} support high fidelity DNA cleavage. The effect of these metal ions on the structure and activity of Kpn1 was studied using SERS. **Chapter 6** talks about the plasmonic features in an organic solar cell. Two low temperature melting alloys were fabricated to increase the efficiency of solar cells. These alloys exhibit plasmonic behaviour in the visible region due to the presence of plasmonic metals like lead, tin and Indium. These plasmonic features contribute to an increase in current density of the solar cells.

Publications

1. *Thermally stable plasmonic nanocermets grown on micro-engineered surfaces as versatile SERS sensors for multi-analyte detection*

Nitant Gupta, Disha Gupta, **Shantanu Aggarwal**, Soumik Siddhanta, Chandrabhas Narayana and Harish Chandra Barshilia

ACS Applied Materials Interfaces, 2014, 6 (24), pp 2273322742

All authors contributed equally

2. *Vacuum free processing of Organic Solar Cells with Plasmonic Features using Low temperature melting alloys*

Prashant Kumar, **Shantanu Aggarwal**, Chandrabhas Narayana and K. S. Narayan

submitted(2015).

3. *Surface enhanced Raman spectroscopic insights into interaction of serum albumins with dihydropyridine based hypertensive drugs*

Shantanu Aggarwal*, Soumik Siddhanta*, Dhanasekaran Karthigeyan, Tapas K. Kundu and Chandrabhas Narayana

Manuscript under preparation.

* Authors contributed equally

CHAPTER 1

INTRODUCTION

The field of molecular spectroscopy has developed very rapidly in the last century. This has led to better understanding of molecular structure and studying interactions at molecular levels. All this has been possible due to advancements in various fields of optical instrumentation, nanoscience and biotechnology. As a result, molecular spectroscopy has become one of the widely researched areas with a huge range of applications from physical, chemical, biological sciences to astronomy. The blue color of the sky is due to light scattered by macroparticles in the atmosphere consisting of dust, water droplets or ice crystals. James Clark Maxwell, a brilliant Scottish scientist of the middle 19th century, showed, by constructing an oscillating electrical circuit, that electromagnetic waves could move through space. Light eventually was proved to be electromagnetic. In his electromagnetic theory of light, he predicted that the scattered radiation from a molecule carries information about the molecule's properties, and the molecule itself acts as the scattering center. Theoretical analysis of light scattering from suspended particles was given by Lord Rayleigh [1]. In 1928, Sir C.V. Raman and K.S. Krishnan studied the inelastic scattering of light by molecules and discovered the now famous Raman Effect [2]. This proved to be very helpful in studying molecular excitations and predicting their structures. C.V. Raman was awarded Nobel prize for this discovery in 1930. Two Russian scientists, Landsberg, and Mendelstam were also credited for this similar phenomena [3]. Raman effect is the shift in frequency of light after

getting scattered from a molecule [4].

The field of molecular spectroscopy can be used for probing different energy scales and thus it can be categorized as electronic, vibrational or rotational spectroscopy. Vibrational spectroscopy probes the vibrational energy levels of a molecule by infrared radiation or Raman scattering. These vibrational energy states lie in the electronic energy states due to coupling of electronic and vibrational energy levels. Lasers play a significant role in spectroscopy techniques due to their ability to produce monochromatic photons with a high degree of spatial and temporal coherence, leading to the increased sensitivity and higher resolution. Vibrational spectroscopy is one of the most efficient methods for studying both the dynamics as well as structure of various molecules in different phases. Each molecule has its fingerprint, a characteristic vibrational spectrum. This unique spectrum is advantageous in sensing, detection and characterization of the various functional groups present in the molecule.

The use of Raman scattering has grown tremendously in the last few decades in various fields. This technique needs no sample preparation and Raman scattering measurements can be done in any state of the sample: solid, liquid or gas. Raman scattering is a weak process i.e. only one part in a billion of total intensity of the incident light is Raman scattered. This is one of the major drawbacks of this technique, and it is overcome by using resonant Raman and surface enhanced Raman scattering (SERS). In 1974, Fleischmann et al. observed intense Raman scattering from pyridine adsorbed on etched silver electrode surface [5]. In SERS, the signal intensity is enhanced by the use of nanoscale roughened metal electrodes substrates or metal nanoparticles. In this thesis we use SERS as a molecular probe. In this chapter, we will introduce the Raman scattering and the phenomena related to it in the context of light scattering.

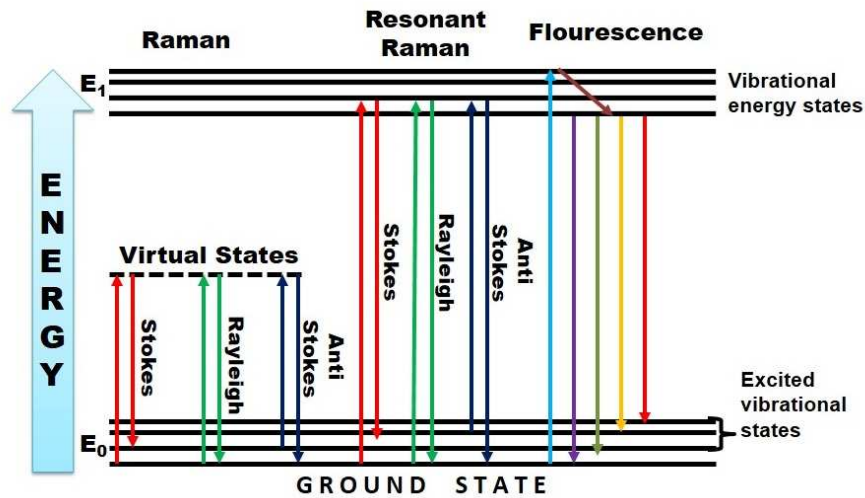


Figure 1.1: Energy level diagram comparing Raman, resonant Raman Scattering and Fluorescence

1.1 Raman scattering

On Interaction of light with molecules, they get excited and make the transition from stable ground state to higher energy states via several energy pathways. Since the excited state has the finite lifetime, these molecules lose energy to come back to the ground state from the excited state, by emitting photons (Fig.1.1). This can happen either by elastic or inelastic scattering of light. Inelastic scattering of light, the emitted photons have the same energy i.e. there is no change in energy. This is known as Rayleigh scattering. In inelastic scattering, the emitted photons either lose or gain energy due to various interactions between photons and molecules. One such interaction which is principally attributable to an inelastic scattering mechanism is called as Raman scattering. When the emitted photons have less energy, it is known as Stokes Raman scattering and when they have higher energy, it is known as anti-Stokes Raman scattering. Raman scattering is a two-photon process as compared to infrared absorption, where the photon gets absorbed

by the molecule, and the molecule undergoes a transition to higher vibrational energy levels. Raman effect can be considered as an optical analog of Compton Effect in molecular systems.

1.1.1 Classical picture of Raman scattering

A molecule upon interaction with Electromagnetic wave having static electric field E , experiences an induced dipole moment. The positively charged nuclei and the negatively charged electrons get spatially distorted which leads to the separation of charges. This polarizes the molecule and creates induced dipole moment, P . The classical approach to Raman scattering is based on the first order of this induced dipole moment. The induced dipole moment of the molecule depends upon the applied electric field given by the following equation [6].

$$P = \alpha \cdot E; \quad (1.1)$$

Where α is the polarizability of the molecule. Both P and E are three-dimensional vectors; so α can be expressed as a 3×3 tensor, whose components can be represented as elements of a matrix. This tensor is sensitive to changes in nuclear coordinates as well as vibrational frequencies. The Eq.1.1, can be represented in tensor form as:

$$\begin{bmatrix} p_x \\ p_y \\ p_z \end{bmatrix} = \begin{bmatrix} \alpha_{xx} & \alpha_{xy} & \alpha_{xz} \\ \alpha_{yx} & \alpha_{yy} & \alpha_{yz} \\ \alpha_{zx} & \alpha_{zy} & \alpha_{zz} \end{bmatrix} \begin{bmatrix} E_x \\ E_y \\ E_z \end{bmatrix} \quad (1.2)$$

When the molecule interacts with time varying electric field, having oscillation frequency ν and the oscillatory electric field

$$E = E_0 \sin 2\pi\nu t \quad (1.3)$$

then the induced dipole moment is also oscillatory in nature and is given by

$$P = \alpha \cdot E = \alpha E_0 \sin 2\pi\nu t \quad (1.4)$$

This oscillatory dipole moment gives rise to the Rayleigh scattering and represents the elastic scattering component. If the molecule is comprising of N atoms it has $(3N - 6)$ vibrational modes. In the case of linear molecule it is $(3N - 5)$. Hence the polarizability will be a function of these independent normal vibrational modes of this molecule. Let the nuclear displacement be q , of a normal vibrational mode with frequency ν_{vib} , is represented as:

$$q = q_0 \cos 2\pi\nu_{vib}t \quad (1.5)$$

where q_0 is the amplitude of vibration. The Taylor's series expansion of polarizability for a small amplitude of vibration is expressed as:

$$\alpha = \alpha_0 + \beta \sin 2\pi\nu_{vib}t; \quad (1.6)$$

where α_0 is the equilibrium polarizability, β is the rate of change of polarizability with respect to this q_0 and ν_{vib} is vibrational frequency of the molecule. Hence, the induced dipole moment P is now give as

$$P = \alpha E_0 \sin 2\pi\nu t + \frac{1}{2}\beta E_0 \{\cos 2\pi(\nu - \nu_{vib}) - \cos 2\pi(\nu + \nu_{vib})\} \quad (1.7)$$

From the above Eq.1.7 it can be seen that the oscillating dipole has three

frequency components, ν , $\nu - \nu_{vib}$ and $\nu + \nu_{vib}$. The inelastic scattering of light then is represented as Stokes ($\nu - \nu_{vib}$) and anti-Stokes ($\nu + \nu_{vib}$) Raman. For a vibration to be Raman active, the rate of change of polarizability (β) should be non zero.

1.1.2 Quantum picture of Raman scattering

The origin of Stokes and anti-Stokes lines can be well understood from classical theory of Raman scattering. But, the anomaly about the intensities of Stokes and anti-Stokes lines is not understood in this picture. The classical theory predicts them to be equal which is not true as in reality, the Stokes lines are much stronger in intensity than the anti-Stokes. The intensity ratios of Stokes and anti-Stokes lines is well accounted in the quantum mechanical picture. The molecule is treated quantum mechanically whereas the radiation is treated as classically. This theory of Raman scattering was derived by Placzek [7] using the dispersion theory given by Kramers and Heisenberg [8]. The quantum mechanical picture of Raman scattering is a two-photon process and is based on second-order perturbation theory.

According to the fundamental principles of quantum mechanics, the energy associated with electronic, vibrational and rotational degrees of freedom of a molecule are discrete. A molecule can undergo a transition from one vibrational quantum having energy E_1 to another state having energy E_2 , through a virtual state having energy E_ν . The virtual state refers to a transition state which does not correspond to an eigenstate of the molecule, so it is only an imaginary state. The electromagnetic radiation is treated as the source of perturbation of the molecular system. Any direct transition between two energy levels is accompanied by emission or absorption of radiation if the dipole moment of the transition is nonzero. The

amplitude concerning a transition from an initial state i to a final state f induced by radiation of wavenumber $\tilde{\nu}_0$ is given as:

$$[\mu]_{fi} = \langle \psi_f | \alpha | \psi_i \rangle \cdot E; \quad (1.8)$$

where ψ_f and ψ_i are the wavefunctions of the initial and the final states respectively. The transition polarizability tensor determines the intensity of Raman scattered radiation. Considering the wavefunctions as similar to harmonic oscillator wavefunctions. The Electrical and the mechanical anharmonicity can be neglected. It can be realized that only those matrix elements are non-zero for which one vibrational quantum number changes by unity and all the other vibrational quantum numbers remain unchanged. The transition polarizability associated with Stokes Raman scattering is:

$$[\alpha_{xy}] = b\beta\sqrt{v+1}; \quad (1.9)$$

where v is the vibrational quantum number and $b = \hbar/(4\pi c\tilde{\nu})$, is the quantum mechanical analog of the amplitude of a classical oscillator. Just like the classical theory, in quantum theory, any transition is Raman active only if at least one component of the derived polarizability tensor is non-zero. Quantum mechanical treatment is dependent on quantum numbers, and this gives information about intensities of Raman scattering. The distribution of molecules in various vibrational states is a function of temperature T . This leads us to an important quantity which is the ratio of intensities with respect to Stokes to anti-Stokes line given by,

$$\frac{I_{Stokes}}{I_{anti-Stokes}} = \left(\frac{\tilde{\nu}_0 - \tilde{\nu}_k}{\tilde{\nu}_0 + \tilde{\nu}_k} \right)^4 \exp\left(\frac{hc\tilde{\nu}}{kT} \right) \quad (1.10)$$

Eq.10 can be used to determine the insitu temperature of the sample. Scattering cross-sectional area of a molecule interacting with the incident radiation is represented by Raman cross section. The general expression for Raman cross section is as follows:

$$\sigma(i \rightarrow f) = \frac{8\pi\omega_s^4}{9\hbar c^4} \left| \sum_j \left(\frac{\langle \alpha_{ij} \rangle \hat{e}_L \langle \alpha_{jf} \rangle \hat{e}_s}{\omega_{ij} - \omega_L - i\gamma_L} + \frac{\langle \alpha_{ji} \rangle \hat{e}_L \langle \alpha_{jf} \rangle \hat{e}_s}{\omega_{jf} - \omega_L - i\gamma_j} \right) \right|^4; \quad (1.11)$$

where \hat{e}_L and \hat{e}_s are unit vectors representing the polarization of the incident laser beam and the scattered light. The sum extends over all virtual intermediate levels j with homogeneous width γ . The initial and final state have the same parity as they are connected by two-photon transitions.

1.2 Surface Enhanced Raman Scattering(SERS)

Surface-enhanced Raman spectroscopy (SERS) was first observed on roughened electrodes by Fleischmann et al. in 1974 and it was further developed by other groups in 1977 [9], [10]. It is a technique of enhancing Raman scattering cross section by adsorption of molecules on metallic nano surfaces [11], [12]. These nano surfaces exhibit atomic scale roughness and acts as plasmonic surfaces to the molecules in their close vicinity. Normal laser Raman scattering suffers from low scattering cross section of molecules at lower concentration. For fluorescent molecules, Raman signals are sometimes masked by the fluorescence background. The fluorescence cross section of molecule is typically of the order of 10^{-17} cm² per molecule [13] and the non-resonant Raman cross section is around 10^{26} cm² per molecule. Surface enhanced Raman scattering does not suffer from this problem and has scattering cross section comparable to Fluorescence [14].

It has been seen that noble metals like gold, silver and copper show high SERS enhancement in the form of plasmonic nanostructures as compared to metals like aluminum, lithium, and sodium. The drastic increase in scattering cross section in SERS can be explained with the help of two mechanisms namely Electromagnetic and chemical enhancements [9]. The former involves enhancement of electric field while the latter is a result of enhancement in polarizability of the molecule due to chemical effects such as charge transfer excited states and the formation of resonant intermediates.

1.2.1 Electromagnetic enhancement mechanism

The Drude model describes a metal as a sea of electrons surrounding periodic static positive charges. A small displacement of electrons due to the electric field of the electromagnetic radiation leads to the formation of an oscillating dipole with the frequency similar to this excited electromagnetic radiation. An electric field is generated by the oscillation of dipole. Any molecule placed in the vicinity of the metallic surface experiences this enhanced electric field (Fig.1.2). The net electric field experienced by a molecule adsorbed on the surface of metallic nanostructure can be represented as:

$$E_i = E_o + E_S \quad (1.12)$$

where E_o is the incident electric field and E_S is the electric field produced due to surface plasmon oscillation. If r is the radius of metallic nanosphere and d is the distance of the molecule from the surface of metallic nanosphere, then from Drude model, E_S is given by relation:

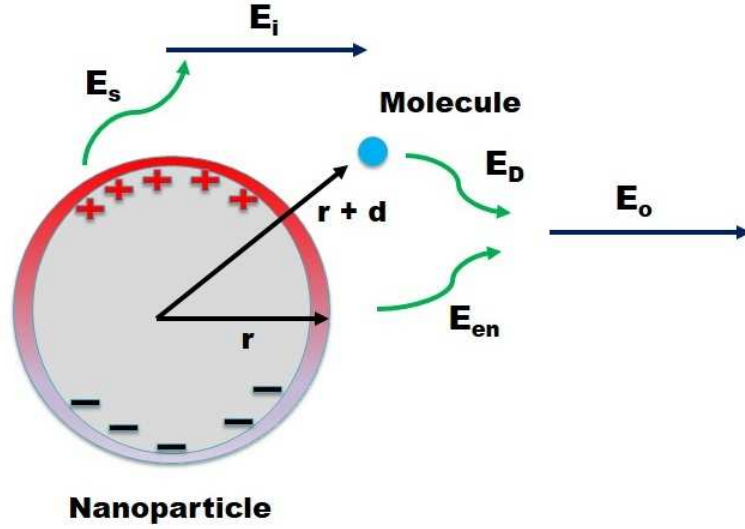


Figure 1.2: Schematic for the electromagnetic enhancement mechanism in SERS

$$E_s = \frac{\varepsilon - \varepsilon_0}{\varepsilon + 2\varepsilon_0} \left(\frac{r}{r+d} \right)^3 \quad (1.13)$$

A dipole μ_i is induced by the resultant electric field E_i in the molecule, which is directly proportional to the electric field E_i and polarizability tensor α . The electromagnetic enhancement for Stokes scattering is given as:

$$G_{SERS}(\nu_s) = |A(\nu_L)|^2 |A(\nu_S)|^2 = \left| \frac{\varepsilon(\nu_L) - \varepsilon_0}{\varepsilon(\nu_L) + 2\varepsilon_0} \right|^2 \left| \frac{\varepsilon(\nu_S) - \varepsilon_0}{\varepsilon(\nu_S) + 2\varepsilon_0} \right|^2 \left(\frac{r}{r+d} \right)^{12} \quad (1.14)$$

The SERS electromagnetic enhancement (G_{SERS}) is proportional to the fourth power of local electric field in the vicinity of the metallic nanostructure. For maxima of G_{SERS} , ie resonant excitation of surface plasmons of the metal sphere, the real part of $\varepsilon(\nu)$ should become equal to $-2\varepsilon_0$ and the imaginary part should be negligible. Metals like Ag, Au, and Cu satisfy this condition at visible wavelengths of light and, therefore, exhibit high SERS enhancements and properties in the vis-

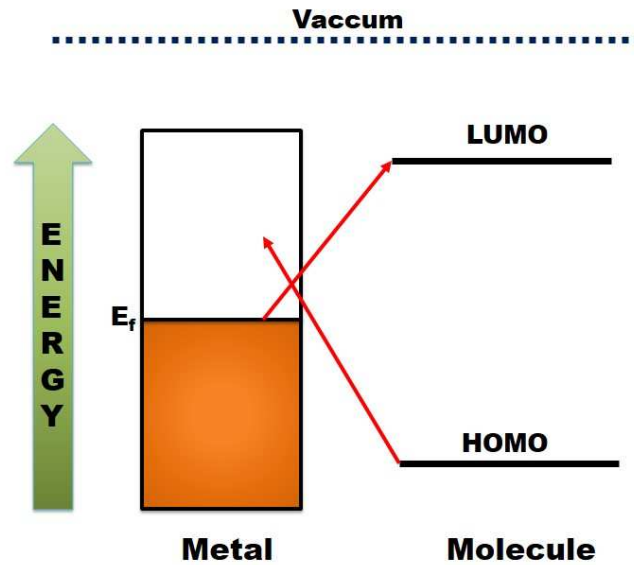


Figure 1.3: Schematic for the chemical enhancement mechanism in SERS

ible region. The electromagnetic enhancement is a distance-dependent mechanism and the enhancement decays as $\left(\frac{r}{r+d}\right)^{12}$. Hence, the molecule need not be in contact with the metal surface to exhibit enhancement. In addition, the nanostructure geometry has an effect on the enhancement factor as some geometries can create more localized areas known as *hotspots*. They are formed at sharp tips as well as in gaps between closely packed nanostructures. The electromagnetic enhancement contributes around $10^6 - 10^9$ to the total SERS enhancement.

1.2.2 Chemical enhancement mechanism

Chemical enhancement is observed when the molecule and the metal surface are in contact with each other by a bond formation. It is also known as a first layer effect and leads to the formation of an adsorbate-surface complex. Electronic

coupling occurs when a molecule is in contact with the surface of the metal. This results in the increase of Raman cross section of adsorbed molecule as compared to its free form in case of normal Raman. The charge transfer in adsorbed molecule leads to the broadening and shifting of the electronic level. This is similar to resonance Raman effect and results in enhancement of Raman scattering cross section leading to SERS enhancement [15]. The energies of the highest occupied molecular orbital (HOMO) and the lowest unoccupied orbital (LUMO) are symmetric to the Fermi level of metal (Fig.1.3). The shift in Fermi Level changes the resonance conditions. When a photon is absorbed by the metal, it results in a hot electron state. The hot electron gets transferred into the LUMO of the molecule and then back to the metal by emitting Stokes photons. The metallic surface need not be rough for observing chemical enhancement mechanism, and it contributes to an enhancement factor of 10 to 100 times.

1.2.3 Experimental calculation of SERS enhancement factor

SERS enhancement factor is a qualitative method for evaluating the increase in Raman signal intensity. SERS experiment are performed in either solution or solid phases, and the number of molecules in the probed volume at an instant of time are different for these cases. So, the enhancement factors are different in the solution and in the solid phases. The enhancement factor for a substrate cannot be defined uniquely due to non non-uniform distribution of the analyte molecule on the SERS substrate as well as high localization of the hot spots. The SERS enhancement factor is calculated in the following two ways:

1. Analytical Enhancement Factor (AEF):

$$AEF = \frac{I_{SERS}}{I_R} \times \frac{C_R}{C_{SERS}} \quad (1.15)$$

where I_R = signal intensity in a normal Raman Experiment

I_{SERS} = signal intensity in the SERS Experiment

C_R = concentration of analyte in the Raman experiment

C_{SERS} = concentration of analyte in the SERS experiment

2. SERS substrate enhancement factor (SSEF): In this method it is assumed that SERS has contribution from first few monolayers of the analyte molecule on SERS substrate.

$$SSEF = \frac{I_{SERS}}{N_{Surf}} \times \frac{N_{Vol}}{I_R} \quad (1.16)$$

where N_{Vol} is the average number of molecules in the scattering volume, V in a Raman experiment.

$$N_{Vol} = C_R \times V \quad (1.17)$$

N_{Surf} is the average number of adsorbed molecules in volume V in the SERS experiment. For higher accuracy in the enhancement factor, the surface coverage must be less than one monolayer.

1.3 Secondary structure of proteins

Cells use 20 different standard L- α -amino acids for protein construction. Amino acids contain both a basic amino group and an acidic carboxyl group. This di-functionality allows the individual amino acids to join in long chains by forming

peptide bonds: amide bonds between the $-NH_2$ of one amino acid and the $-COOH$ of another. Sequences with fewer than 50 amino acids are referred to as peptides while the terms protein or polypeptide are used for the longer sequences. A protein can be made up of one or more polypeptide molecules. There are two ends of the peptide or protein sequence, C-terminal, and N-terminal. C-Terminal end has a free carboxyl group, and the N-terminal has a free α -amino group.

Different substituents of the amino acids side chains give rise to different chemical, physical and structural properties of the protein. The amino acid sequence of a protein is encoded in DNA. Transcription is a process of using DNA strand to make a complementary messenger RNA strand (mRNA). The mRNA sequence is used as a template to guide the synthesis of the chain of amino acids which make up protein. Often, post-translational modifications, such as glycosylation or phosphorylation, occur which are necessary for the biological function of the protein. While the amino acid sequence makes up the primary structure of the protein, the chemical/biological properties of the protein are very much dependent on the three-dimensional or tertiary structure. Hydrogen bonding in amino acids leads to stretches or strands of proteins having distinct characteristic local structural conformations or secondary structure. The three types of secondary structure are the α -helix, the β -sheet and the random coils.

The α -helix is a right-handed coiled strand in which oxygen of the $iC=O$ of each peptide bond in a strand binds with the hydrogen of the N-H group of the peptide bond four amino acids below it in the helix. In the case of β -sheet, the $iC=O$ oxygens in one strand hydrogen binds with the amino hydrogens of the adjacent strand, i.e., inter strands hydrogen bonding. Depending upon the direction of N-terminal and C-terminal strands, β -sheets, are either parallel or antiparallel. The anti-parallel β -sheets are more stable due to the more well-aligned hydrogen bonds.

In the case of random coils there is a very little hydrogen bonding which gives it flexibility in structure.

The complexities of protein structure make the elucidation of a complete protein structure extremely complicated even with the most advanced analytical equipment. An amino acid analyzer can be used to determine amino acids present in a protein along with their ratios. Techniques like mass spectroscopy and peptide mapping can be used to analyze the primary sequence of the protein. It is easier to use these techniques for peptides and small proteins but very difficult for large multimeric proteins. Peptide mapping entails treatment of the protein with different protease enzymes in order to chop up the sequence into smaller peptides at specific cleavage sites. Two commonly used enzymes are trypsin and chymotrypsin. Mass spectroscopy has become an invaluable tool for the analysis of enzyme digested proteins, by means of peptide fingerprinting methods and database searching. Another method, Edman degradation involves the cleavage, separation and identification of one amino acid at a time from a short peptide, starting from the N-terminus.

Circular dichroism spectroscopy (CD) is another method which is used to characterize the secondary structure of a protein. The different types of secondary structure, the α -helix, the β -sheet and the random coil, all have characteristic circular dichroism spectra in the far-UV region of the spectrum (190-250 nm). These spectra can be used to approximate the fraction of the entire protein made up of each type of structure. X-ray crystallography or nuclear magnetic resonance (NMR) analysis provide a more complete, high-resolution analysis of the three-dimensional structure of a protein. X-ray diffraction allows measurement of the short distances between atoms and yields a three-dimensional electron density map, which can be used to build a model of the protein structure. But a large, well-ordered single crystal is required for determining the three-dimensional structure of a protein by

using X-ray diffraction. It is very difficult to crystallize the proteins and proteins sometimes lose their activity upon crystallization. Moreover, it does not provide solution phase dynamics. NMR can also be used in three-dimensional structure determination of proteins. It is more advantageous to use NMR than XRD as it can be carried out in solution phase. The two-dimensional NMR techniques used are NOESY, which measures the distances between atoms in space, and COESY, which measures distances through bonds. But it in case of bigger proteins, it becomes difficult to interpret the data.

Vibrational, absorption and emission spectroscopy are also used for providing information about specific structural aspects of protein. Raman and IR gives an estimate of the secondary structural elements of proteins. Fluorescence spectroscopy provides information about specific residues in proteins and their environment. In this thesis we use Raman spectroscopy for studying the structural changes and the detailed molecular information of the proteins, as well as their interaction with other molecules like the drug and the metal ions.

1.4 Raman spectroscopy of proteins

The vibrational Raman spectrum of the proteins has contributions from large number of the normal modes as proteins contain thousands of atoms. So analysis of Raman spectra becomes very difficult and tedious. But different regions of the Raman spectra can be interpreted separately to extract meaningful information about proteins and their structure. Using Raman spectroscopy, information about structure and environment of different side chains of amino acids can be obtained. Band positions and bandwidths can provide an insight about the backbone of proteins. Any ligand bound to protein causes a change in the structure of protein.

If the ligand is in unbound state, the Raman spectra will be an overlap of bands corresponding to ligand as well as proteins. But if the ligand binds to the protein, along with the overlap of spectra, new modes will also appear due to the interaction between the ligand and protein. So Raman Spectroscopy is a handy tool for studying proteins of various sizes and in different environments. One the major advantage of using Raman spectroscopy for the study of proteins is that the proteins can be used in both solutions as well as solid (crystallized) form.

The Raman spectra of proteins provide information about amino acid side chains vibrations, backbone vibrations, and the amide vibrations. Aromatic amino acids phenylalanine, tyrosine, tryptophan, and histidine have highly polarizable aromatic rings. The vibration modes arising from these aromatic amino acids play a vital role in study of proteins and are used as Raman markers. One such commonly used marker is the Fermi doublet of tyrosine. The doublet bands are observed around 830 and 850 cm^{-1} in Raman spectra. They arise due to the interaction between the ring breathing fundamental, and the overtone of the C-C-O deformation in para-substituted benzene rings [16]. The information about the environment and hydrogen bonding conditions of the phenol group of the tyrosine residue can be obtained from the relative intensities of the doublet bands. Tryptophan has an indole ring which give rise to as many as 18 bands in the Raman spectra. Similar to tyrosine, tryptophan also has a Fermi doublet around 1360 and 1340 cm^{-1} which gives information about the hydrophobicity around the tryptophan residue. Another band at 761 cm^{-1} can be used to study hydrophobicity around the indole ring. The ring vibration of phenylalanine corresponds to a band around 1000 cm^{-1} which is invariable to conformational changes in proteins. it can be used for normalizing Raman spectra. Side chain vibrations in cysteine correspond to S-S stretching vibrations. These bands are observed near 510 and 540

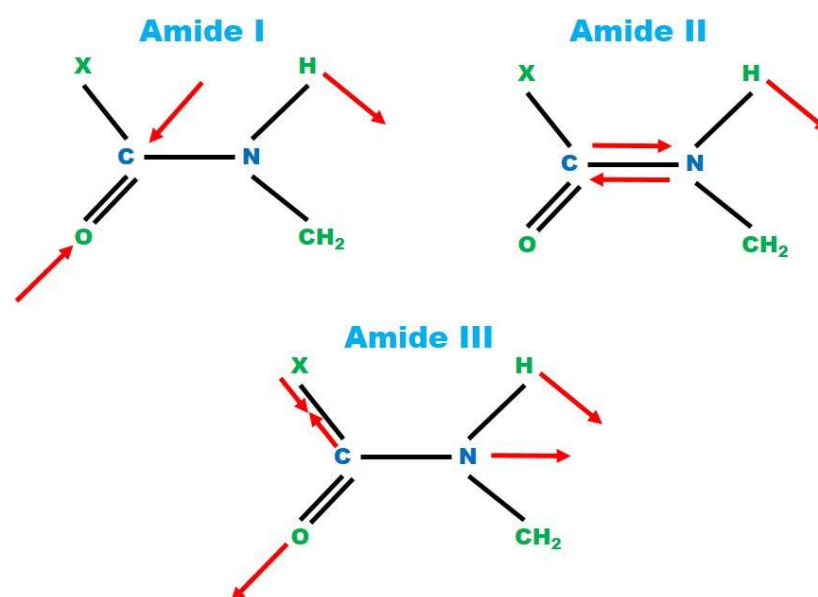


Figure 1.4: Amide vibrational modes in Proteins

cm^{-1} . The gauche and trans forms of cysteine affect the C-S stretching Raman modes. Alkyl chain vibrations are also observed around $1400-1500\text{ cm}^{-1}$.

The amide bands are also used as the Raman markers. They provide information about secondary structural components of the proteins. There are three types of amide vibrations which give rise to Amide I, II and III bands (Fig.1.4). All of them are combinations of N-H and C=O vibrations. C=O stretching vibrations corresponds to Amide I and C-N stretching in conjunction with N-H bending corresponds to Amide II. Amide II is Raman inactive. Amide I is commonly used for secondary structure analysis of protein. Amide III has contribution from alkyl side chains. For each secondary structure, α -helix, β -sheet and random coils have their characteristic Amide I band position. Their relative fractions can be obtained by their relative intensity ratios obtained after deconvolution of Amide I band. In the case of β -sheets, splitting of Amide I occurs [17]. Two modes are observed.

One strong band at 1630 cm^{-1} followed by a weak band at 1690 cm^{-1} . Amide 1 is also dependent on effects of bond coupling, dielectric constant of protein and hydrogen bonding. Secondary structures other than α -helix and β -sheet like α_{11} and turns have their vibrational modes distributed in the entire spectrum. It's hard to interpret and distinguish them [18], [17].

1.5 SERS of proteins

Surface enhanced Raman spectroscopy of proteins overcomes the problem of low scattering cross section in normal Raman. It has lower fluorescence background and requires a lesser amount of sample for an experiment. Recently, studies have shown that the SERS can be used as a tool for studying biomolecules. It can be used for studying structural changes at the molecular level, unlike normal Raman. Even very minute changes causing local changes in binding pockets and active domains on proteins can be picked up using SERS. SERS spectra of proteins give accurate information about the structure as it selectively enhances the vibrational modes. SERS spectra of protein look very different from normal Raman spectra, which is a convolution of all the vibrational modes. SERS surface selection rules changes and determine the enhancement of particular vibrational mode. Noble metal nanoparticles are used to enhance the electric field in the vicinity, and the part of molecules lying in the vicinity of the surface experiences greater enhancement instead of a complete molecule. The electric field is distance dependence and decays rapidly away from the surface of the nanoparticle. SERS provides surface information about bigger molecules like proteins. Raman scattering intensity is proportional to the product of change of polarizability and electric field. The change in polarizability can be represented as:

$$\widehat{R} = \left(\frac{\partial \alpha}{\partial q} \right)_o = \begin{bmatrix} \alpha'_{xx} & \alpha'_{xy} & \alpha'_{xz} \\ \alpha'_{yx} & \alpha'_{yy} & \alpha'_{yz} \\ \alpha'_{zx} & \alpha'_{zy} & \alpha'_{zz} \end{bmatrix} \quad (1.18)$$

If α'_{xx} element in the Raman tensor is non-zero, the Raman mode has a xy component. The orientation of the molecule with respect to the polarization of the incident light determines appearance or disappearance of mode. Raman intensity is dependent on the polarization of the incident ($\widehat{\epsilon}_s$) and scattered light ($\widehat{\epsilon}_o$). When incident and scattered lights are polarised in same direction ($\widehat{\epsilon}_s = \widehat{\epsilon}_o$), it leads to maximum enhancement. Polarization Components xx , yy and zz belong to A_1 symmetry and xy , xz and yz belong to A_2 , B_1 and B_2 . Each symmetry species has a particular group of polarization components. The modes which have A_1 symmetry are independent of the polarization of the incident light.

The knowledge of Raman tensors of different intensity modes and also the local field polarization experienced by the molecule helps in determining the SERS intensities. Both Density functional theory (DFT) and symmetry analysis can be used for finding Raman tensors. For maximum SERS enhancement (E^4), the incident light and the scattered light should be polarized in the same direction as the electric field in the vicinity of the nanoparticles.

Surface selection rules for SERS was given by Moskovitz [18]. For experimental purposes, it is assumed that the local field polarization is perpendicular to the surface of metal nanoparticle. The vibrational modes parallel to the surface are not enhanced, and those lying normal to the surface are enhanced the most. The modes which are neither parallel nor perpendicular to the surface are also enhanced due to their perpendicular components. Hence, SERS provides information about molecular orientation with respect to the nanoparticle surface.

SERS spectra of proteins are quite different from their normal Raman spectra due modification of surface selection rules. SERS spectra of proteins are dominated by modes from aromatic amino acids. Amino acids aromatic groups have large π electrons which gets strongly polarised giving strong enhancements. Amide bands are also seen. Amide II, which was Raman inactive, becomes visible in SERS. Amide I region is much narrow and can be interpreted in details to determine the secondary structure changes in the protein. We do not need to deconvolute the Amide I region in case of SERS. Information about aliphatic chains, disulfide bonds and carboxylate groups can also be obtained from the SERS spectra of proteins.

In this thesis we begin by developing the SERS sensors by etching Si. These SERS sensors have high enhancement factors with trace detection ability. Multi-analyte like biomolecules, fluorescence markers can be probed with it. The thesis also describes the use of SERS in secondary structure determination of proteins in details. Metal ion effect on protein, as well as ligand binding effect on proteins, have also been studied using SERS. These works demonstrate technique development and utility of SERS as a tool, in study biomolecules. The thesis finally ends with plasmonic applications of SERS in the field of solar energy.

CHAPTER 2

EXPERIMENTAL TECHNIQUES

2.1 Instrumentation

A custom made Raman setup, consisting of an excitation source (laser), an epifluorescent microscope converted to a Raman microscope, collection optics, a spectrograph, a CCD detector and a computer interfacing was used for all the Raman and surface-enhanced Raman spectroscopy experiments [19].

A He-Ne gas laser (632 nm) or a frequency-doubled Nd-YAG solid state laser (532 nm) was used as the Raman excitation source. Nanoparticles of noble metals are used for enhancing Raman signals in SERS experiments, which absorb in different regions to generate surface plasmons. The incident light from the laser comes in resonance with the surface plasmons of the nanoparticles resulting in enhanced SERS. Hence, depending upon the region of the absorption of the nanoparticles, one of the two lasers was chosen.

The laser was passed through plasma line filters (PF) and neutral density filters (NDF). PF removes the plasma lines generated in a gas laser while NDF were used to reduce the power of transmitted beam from the laser. This is important while working with organic samples or biological samples in order to prevent laser induced chemical change or degradation of the sample. The laser beam is reflected onto the sample by a dichroic mirror at 45°. A high numerical aperture objective focuses the incident light on to the sample and also collects the 180° backscattered light from

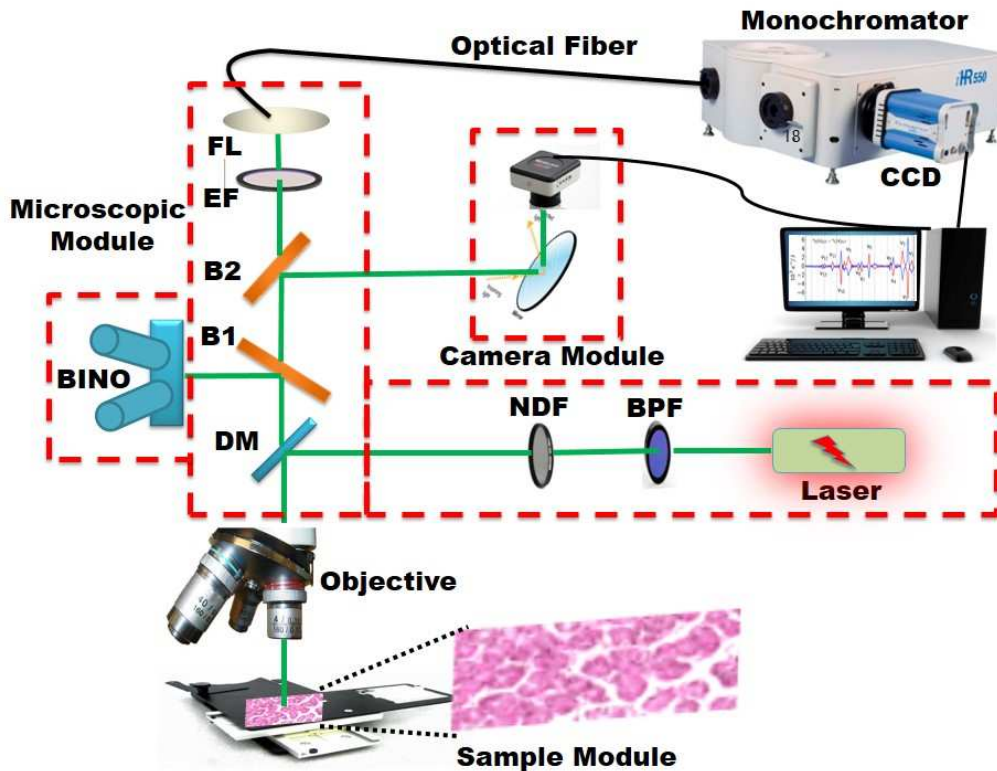


Figure 2.1: Schematic Raman Setup. The collection optics consists of the following components: NDF neutral density filter, BPF band pass filter, DM dichroic mirror, B1 and B2 beam splitters, BINO binocular, EF Edge filter, FL focussing lens

the sample. This backscattered light from the objective, passes again through the dichroic mirror before passing through an edge filter to finally enter the output port of the epi-fluorescent microscope. The light is then directed towards the Raman spectrograph through an optical fiber. The fiber is f-number matched to both the microscope and the spectrograph. Fig.2.1 shows the complete schematic of the Raman setup used in all the experiments.

The Raman spectrograph used for these experiments had Czerny-Turner type monochromator (iHR320, Horiba Jobin Yvon). The captured light was converted to electrical signals through a peltier cooled charge coupled device (Andor, DU401A-BR-DD). The monochromator consists of a computer-controlled adjustable en-

trance slit and a triple grating turret. The turret has the following gratings: holographic 1800 grooves per mm for providing the highest resolution, 1200 grooves per mm and 600 grooves per mm. Peltier cooled CCD comprised of a two-dimensional array (1024 X 127 pixels) having a pixel size of 26 x 26 micrometers is employed to collect the signal. A digital camera port is present on the top of the microscope to optical imaging of the sample and align the fiber to this laser spot on the sample.

2.2 Spectral Measurements

Surface enhanced Raman spectroscopy can be performed both in liquid or dry state. Since, proteins denature when dry, it is necessary to perform SERS of proteins for their structural determination in the liquid state. This gives the information about the structure of protein as it present in the biological environment. The SERS spectra of protein can help determine even a subtle variation at the molecular level due to the structural change. For liquid samples, typically 1-2 μl of the sample is mixed with 10 μl of nanoparticles and then dropped on a clean glass slide. Grooved glass slides can be used to prevent the spreading of the drop. In the case of regular glass slides, the liquid solution keeps spreading slowly with time. This defocuses the sample while using the air objective lens. A water immersion objective can be used for samples which are weak scatterer, especially for proteins. The water immersion objective has high numerical aperture (N.A.) for increasing the spatial resolution as well as collection of scattered light. This is ideal for acquiring spectrum where the object lies in contact with the objective. The liquid sample forms an elongated capsule enclosed between the water immersion lens and the glass slide. This geometry of the liquid sample helps in light trapping by multiple reflections, thereby increasing the net flux of backscattered light from the

sample into the lens. Both, the nanoparticles and proteins, are sticky moieties. They stick and contaminate the water immersion objective lens. Therefore, it becomes necessary to clean the surface of the objective lens thoroughly before use. This can be done by putting a drop of Proteinase K solution on the objective lens and then incubating it at 37°C for around 30 minutes. After this, the lens is thoroughly washed with water and ethanol. The proteinase K solution helps to digest proteins which tightly binds to the glass surface.

The resolution of the spectrum is usually defined by the width of the entrance slit of the monochromator. The resolution of the spectrum can be increased or decreased by adjusting this slit width. In all our experiments, the entrance slit to the monochromator was typically set at 200 μm . In the case of weakly scattering samples, the slit width can be increased for an increase in the intensity, but this decreases resolution. A high resolution of 0.7 cm^{-1} was achieved in all the Raman and SERS experiments by using the 1800 grooves per mm grating. At such a high resolution, the CCD chip covers around 600 cm^{-1} in a single window. The entire spectrum is divided into 7 windows for scanning a region from 100 to 4000 cm^{-1} . There was an overlap of around 30 cm^{-1} between each windows.

The intensity of the laser was kept at 8 mW at the sample to avoid damage to the sample. When sample degradation sets in, the spectrum is dominated by the D and G peaks, coming from amorphous carbon formed due to the charring of the substrate. These peaks are found at around 1350 and 1600 cm^{-1} respectively. The laser intensity was adjusted in such ways to prevent the sample from degrading as well as to get the highest signal-to-noise ratio. The average accumulation time for acquiring SERS spectrum varied from 30 s to 120 s. It must be noted that the more is the accumulation time, the more is the exposure of the sample to laser. This might cause the sample to undergo degradation. To get a better spectrum,

multiple spectra are averaged by increasing the accumulation number.

2.3 Calibration of Raman spectra

Raman spectral calibration is a crucial process. Each Raman spectra should be calibrated before analysis for accurate interpretation. Factors like the movement of the grating can cause minor shifts in the Raman spectra. This will lead to misinterpretation of data especially in the case of proteins where the Raman spectra contain large number of convoluted vibrational modes. Therefore, to avoid such errors, calibration of the spectrum is a must. The standard way for calibration is to collect a spectrum of a compound which has sharp Raman peaks and compare them with their usual positions reported in the literature. Instead of a compound, mostly the neon glow lamp is used as an emission source as it has many characteristic sharp lines in the complete region of interest. Each window is calibrated at the beginning of the day and at the end of the day by recording this Ne spectrum.

2.4 Analysis of Raman spectra

The Raman and SERS spectra of proteins, biochemicals, dyes, polymers and other chemicals have majority of their bands in the region between 500 to 1750 cm^{-1} , corresponding to various amino acids, protein backbones, amide bands, stretching and vibration frequencies. The region from 700 to 1200 cm^{-1} is known as the fingerprint region and plays a very crucial role in band assignments. In the last 50 years, all the important modes have been assigned by both experimental and theoretical methods. There exists a vast literature which can be used to assign the modes in most of the compounds. But in case of proteins there is an enormous

overlap of different modes owing to the complex structure of protein. This makes it difficult to assign some of the modes. So to be sure about band assignments of these modes, some specific experiments are performed. For example, amide I mode in protein is observed between 1600 and 1700 cm^{-1} . It is an important mode of structural determination. But it has some overlap from the stretching frequencies of some of the amino acids. So deuteration experiments are performed for a confident band assignment. This will be discussed in details later.

Spectrum of nanoparticles and protein buffer should be recorded as a part of control experiments to see their contribution to the final protein spectrum. Certain buffer components give enormous Raman scattering which can completely dominate the protein spectrum. Therefore, these components should be removed from the protein solution through dialysis before acquiring the protein spectrum. It should be ascertained that protein functionality is not lost by removing these components.

2.5 Acquiring SERS spectra from Proteins

Attachment of Protein to Silver Nanoparticles

Plasmonic silver nanoparticles were synthesized by Lee-Meisel method [20]. Milli-Q water with a resistance of 18.2 $M\Omega cm$ at 25°C was used for all the experiments. 18 mg of silver nitrate was added to 100 ml of water and boiled under reflux conditions to maintain water at a constant level. 2 ml of 1% sodium citrate solution was added to this solution under vigorous stirring. The boiling and stirring was continued for 1 h. The solution was then brought back to room temperature while stirring. The nanoparticles were then characterized by UV-Vis spectroscopy, zeta-potential measurements and transmission electron microscopy (TEM) (Fig.2.2).

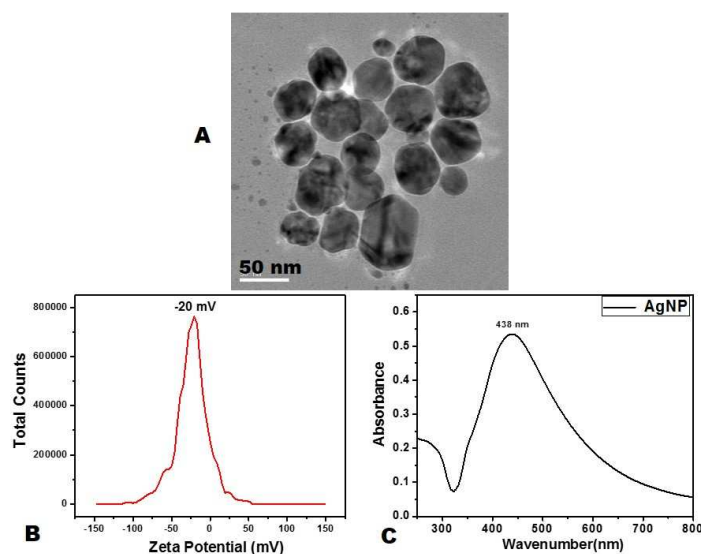


Figure 2.2: Attachment of protein to nanoparticles: (A) TEM of Ag nanoparticles (scale bar = 50 nm). (B) Zeta potential measurement of Ag nanoparticles showing overall negative charge. (C) The UV-Vis spectrum of Ag nanoparticles showing maxima at 438 nm.

Protein molecules are weak Raman scatterers. For obtaining enhancement, the molecule should be adsorbed to the silver nanoparticle. There are several strategies used to link protein molecules to the surface of nanoparticles. The most common are electrostatic absorption, attachment to ligand on nanoparticle surface, using the cofactor-ligand chemistry and direct conjugation to the nanoparticle surface [21].

Sodium Citrate used in the synthesis of colloidal nanoparticles acts as a weak capping agent. It prevents nanoparticles from agglomerating and also allows the analyte molecules to be electrostatically attracted to the silver nanoparticles. The analyte molecule replaces the citrate molecules to come in direct contact with the metal nanoparticle. DLS data shows a net charge of -20 mV on the surface of the nanoparticles. The pH of as-prepared nanoparticles was found to be around 8. Therefore, any protein of pI above 8 can be electrostatically attached to the

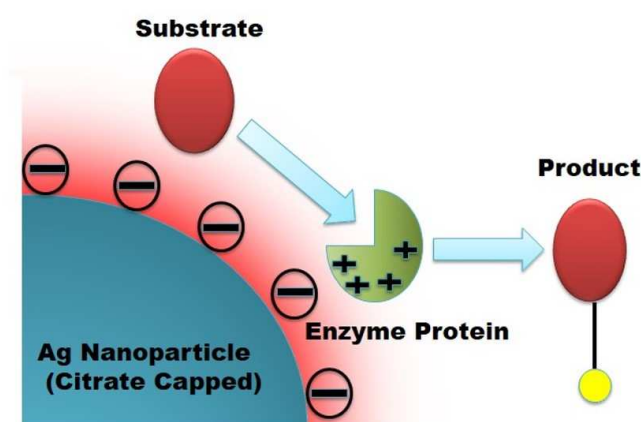


Figure 2.3: Schematic showing the biochemical assay performed to check the activity of protein in the presence of Ag nanoparticles

surface of these citrate capped nanoparticles.

For the attachment of proteins to the nanoparticles, the size of nanoparticles plays a vital role especially if the size of the nanoparticle and that of the protein are comparable. The proteins are 2-10 nm in size and the silver nanoparticles prepared by the Lee Meisel method have diameters of 40 to 60 nm. This size distribution is necessary for generating surface plasmons in the visible range for SERS applications. Also, the nanoparticle is much bigger as compared to protein, so the mode of attachment is not affected by such sizes. Surface Charges (hydrophilicity) on the protein surface can help determine the attachment site of protein on the nanoparticle.

Activity of the protein-nanoparticle conjugate

The attachment of molecules like proteins to the nanoparticles creates an interface between organic and inorganic materials. This leads to enhanced surface effects which may cause structural deformation. In the case of proteins, their func-

tions are determined by their structures. So any change in structure of protein on attachment with nanoparticle will yield spectra of the deformed structure. So before starting any SERS experiments of proteins, biochemical activity assays are done to check the activity and functionality of protein in the presence of nanoparticles (Fig.2.3). Another indirect method to monitor the activity of proteins involves use of UV-Vis spectroscopy of Protein-Ag Nanoparticle conjugate. The loss of activity in protein will induce structural changes which will cause agglomeration of the nanoparticles. This will show a shift in plasmon peak of the nanoparticle.

Amide mode verification by deuteration studies

Stability and flexibility of proteins can be explored by exchanging labile hydrogen atoms of the amide with deuterium. This hydrogen-deuterium exchange method helps in Raman band assignments. Raman bands of Amides are very sensitive to such exchanges as they change their position and shift to a lower wavenumber. The amide I vibrations helps in the prediction of secondary structural elements present in proteins as a helix and b sheets. Amide I is generally influenced by changes in the secondary structure of the protein backbone and are independent of the nature of the side chains. Secondary structure of protein can be elucidated from the positions of Amide I band. Each secondary structural element has a fixed position of Amide I in Raman spectrum. It can be deconvoluted further to find their relative contribution.

Consider the bond vibrations as the vibrations of a spring attached to two masses(m_1 and m_2) corresponding to two atoms. Now, the vibrational oscillation of the spring can be written as:

$$\nu_{osc} = \frac{1}{2\pi} \sqrt{\frac{k}{\mu}} \quad (2.1)$$

where μ is the reduced mass and is given by $m_1m_2/(m_1 + m_2)$. On changing any one of the two atoms with a new atom, the vibrational oscillation changes due to change in mass. On replacing the lighter Hydrogen with heavier Deuterium, the vibrational oscillation decreases. A combination of vibrations of N-H and C=O gives rise to various Amide bands in Raman spectra. The vibrations containing NH modes are prone to changes upon deuteration. In the case of Amide I, in plane NH bending vibration changes its frequency on the deuteration. Hydrogen attached to the nitrogen is replaced with a heavier Deuterium. This results in shifting of Amide, I band to lower wavenumbers on the deuteration. In the case of Amide II, the in-plane NH bending along with C-N stretching gets converted to the ND bending vibration upon deuteration. This vibration has a lower frequency than the NH bending vibration, and it no longer couples to the C-N stretching vibration. Therefore, a new mode of Amide II is observed around 900 cm^{-1} . The ND separates out and gets redistributed among other modes for Amide III vibration mode. Deuteration is a very handy technique for confirming band assignments of Amide bands. For any band to be Amide band, it has to have a change in intensity or position on the deuteration.

Amide I verification by denaturation studies

The secondary structure of proteins gets thermally disrupted on thermal denaturation. This causes changes in the Amide I band as it is dependent on the secondary structure of protein. Thermal denaturation takes place through a molten globule state. At melting temperature, an initial downshift of amide I is observed. This gets upshifted to higher wavenumbers at higher temperatures [22]. In case of SERS it is observed that increased side chain interactions with the nanoparticle surface obscures the amide I band [23]. The thermal denaturation leads to protein unfolding. This increases the interaction of the side chains with the surface



Figure 2.4: Linkam THMS 600 heating-cooling stage

of the nanoparticle. As a result, the intensity of Amide I decreases and that of side chains increases on thermal denaturation. This is another technique to verify Amide I mode of proteins.

2.6 Temperature dependent measurements

All the temperature-dependent Raman measurements were done using a Linkam THMS 600 heating-cooling stage (Fig.2.4). The stage is equipped with a temperature controller and a liquid nitrogen pump (TMS94). Any temperature in the range -196°C to 600°C can be set and achieved with an accuracy of 0.1°C . Different heating and cooling rates can be used to go from one temperature to another. In our experiments, we used a heating rate of 10°C per minute and while cooling the sample was allowed to cool to room temperature by Newtons Law of cooling.

CHAPTER 3

PLASMONIC NANOCERMETS AS A VERSATILE SERS SENSORS

3.1 Introduction

A nanoscale composite of a ceramic ('cer') material present in the matrix phase and a metal ('met'), present in the form of nanoparticles (NPs) is known as a Nanocermet. Noble metal NPs (Au, Ag, Cu) absorb strongly in the UV-Vis-NIR spectral ranges on interacting with the electromagnetic radiation. Plasmonic nanocermet exhibits the phenomenon of localized surface plasmon resonance (LSPR) due to the presence of noble metal NPs [24],[25]. The size and shape of the nanoparticles as well as their distribution (inter-particle spacing) and the dielectric properties of the ceramic material, all have an effect on the resonance behavior of plasmonic nanocermet. Recently, plasmonic nanocermet thin films have been employed in photothermal conversion, optical waveguiding, photochromic and photoelectrochemical applications, etc. [26],[27].

One of the major application of the LSPR phenomenon from the plasmonic nanocermet, is used in surface-enhanced Raman spectroscopy (SERS), for providing very high electric field intensities in the vicinity of NPs (high near-field intensities) for the detection of various analytes [28],[29]. Both, solid sensors, fabricated by depositing nanoparticles on a plane or micro-/nano-engineered surfaces as well as

liquid sensors using colloidal suspensions of nanoparticles of noble metals, are used for enhancing Raman signals in surface enhanced Raman spectroscopy [30],[31].

For a strong plasmonic coupling as in the case of solid sensors, metal nanoparticles should be present in a highly ordered arrangement. This can be achieved by using advanced fabrication techniques like e-beam lithography, focused ion beam, etc. But they require a high level of sophistication, as well as they, have low time-and-cost effectiveness and limited spatial resolution due to the electron/ion-beam size [32],[33]. The colloidal suspensions of NPs in liquid SERS sensors give non-reproducible enhancements as they sometimes uniformly agglomerate in the presence of salts and some analytes [34],[31]. Capping agents stabilize the nanoparticles by preventing their agglomeration in the colloidal suspension. But adding capping agents to the colloidal suspensions affects the SERS performance of the nanoparticles [35],[36],[37]. These capping agents are ionically charged and hence repel similarly charged analyte molecules. They act as an impediment for the analyte molecule to directly interact with the NP thus, limiting their range of use [35]. The liquid SERS sensors are difficult to regenerate and non-reusable because the capping agents are non-replaceable in nature [35]. Most of the present SERS sensors, both solid and liquid are unstable at high temperatures and in harsh chemical environments, owing to oxidation of the nanoparticles at high temperatures and degradation in harsh chemical environments.

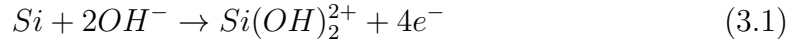
In the present work, we have combined optical properties of micro-engineered Si surface, like light trapping, with those of nanocermetes to design a highly stable and robust SERS sensor for multi-analyte detection [24],[25],[38]. Silver nanoparticles were dispersed uniformly in an amorphous silicon nitride ($a\text{-Si}_3\text{N}_4$) matrix. This matrix of silicon nitride protects the silver nanoparticles from degradation [39]. Micro-pyramidal structure were obtained from silicon (100) by anisotropically etch-

ing it [38],[40]. These micro pyramids contribute to the enhanced nucleation and growth of AgNPs in addition to the light trapping effect [41]. NCES-SERS sensor (nanocermet-on-etched-Si-based-SERS sensor) has highly uniform distribution of AgNPs on the micro pyramids. This results in high enhancement factors ($10^6 - 10^7$) and low detection limit of analytes at very low concentration. The sensor exhibited multifunctional characteristics such as reusability, high-temperature stability, and chemical stability. Hot-spots were distributed homogeneously over the sensor as compared to a roughened Ag substrate [42] which have non-reproducible SERS signals with low enhancement factor(10^3) [43]. The presence of micro-pyramidal structures helps in multiple reflections of light which helps in SERS enhancement. This NCES-SERS sensor can be employed in the fields of biomedicine, pharmacology, microbiology, forensic, chemistry, environmental sciences, etc. Given the fact that both the etching of Si, as well as the sputter deposition of nanocermets, are well-established techniques in the semiconductor industry, the proof-of-concept of the present work can be easily upscaled. The sensor also provides a cost effective and viable alternative to techniques that use non-labelled methods (such as SERS) to avoid the use of radio labeling or fluorescence tagging.

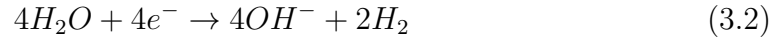
3.2 Experimental methods

Anisotropic Etching of (100) Silicon Substrate: Highly ordered array of micro pyramids were chemically etched on (100) silicon substrate. The micro pyramids that were formed had an angle of 54.74° to the base. These pyramids were square in shape and were formed by the intersection of the 111 planes of silicon [40]. Fig.3.3a Shows the morphology of an anisotropically etched silicon wafer and Fig.3.1 shows the experimental setup which was used to perform the anisotropic

etching of Si (100) wafer. A heated solution mixture containing potassium hydroxide, KOH (10 wt.%) and ethylene glycol, HO-CH₂-CH₂-OH (20 vol.%) was used for wet chemical Etching of silicon. This solution was maintained at 85 °C. This process of wet chemical etching of silicon by KOH is a well-known process. KOH is anisotropic etchant and is known to etch Si along the (111) plane. The complete process of chemical etching can be written in the form of chemical equations as: Si is first oxidized by the hydroxyl ions to form a silicate:



Water is simultaneously reduced to give off the hydrogen gas:



The silicate that was thus formed reacts further with more hydroxyl ions to produce a water soluble complex:



The entire redox reaction can thus be summarized as:



Isopropyl alcohol (IPA) increases the anisotropy in etching, controls the adherence of the H₂ bubbles to the Si surface. So a solution containing a mixture of both isopropyl alcohol as well as KOH solution is used. This solution mixture has increased wettability property. Ethylene glycol has a higher boiling point as

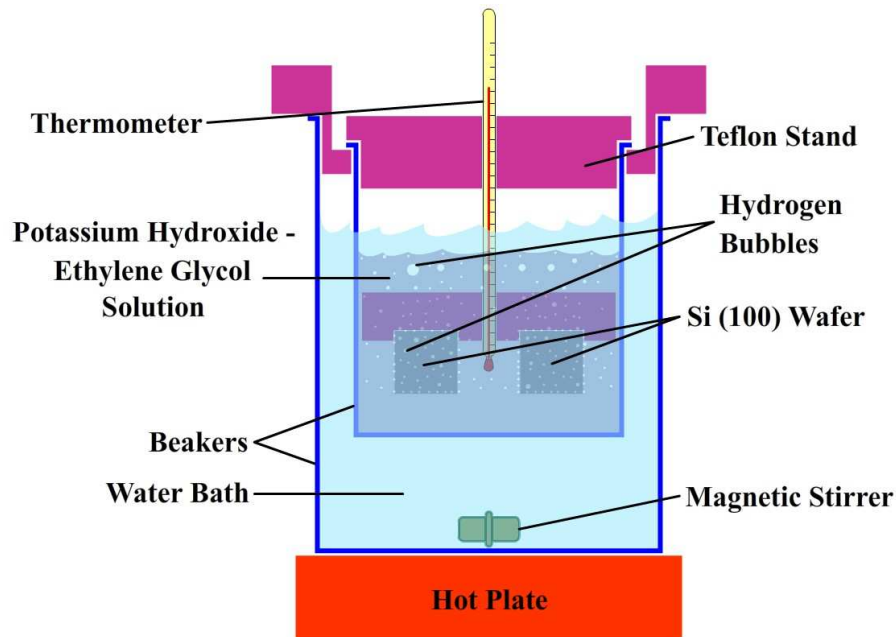


Figure 3.1: Experimental setup for anisotropic etching of Si (100) wafer. Adapted with permission from [44]

compared to that of isopropyl alcohol. So, for high-temperature etching, ethylene glycol is preferred over isopropyl alcohol. The size and distribution of the Si micro pyramids are dependent upon the size and distribution of hydrogen gas bubbles in the solution. It can be varied by varying the temperature and concentration of the etching solution.

The etched Si samples with micro-pyramids have more surface area as compared to bare Si. This contributes to the fact that the sensor can be used for enhancing Raman signals as the increase in surface area will contribute to exposing larger area to a laser beam. It also leads to enhancement of nucleation of the silver nanoparticles in the silicon nitride matrix. When the light is incident on the micro-pyramids formed by etching, it gets reflected multiple times between different surfaces of pyramids. So there is an overall increase in the antireflection properties of the etched Si. This was confirmed by recording the Raman spectra of plane and etched

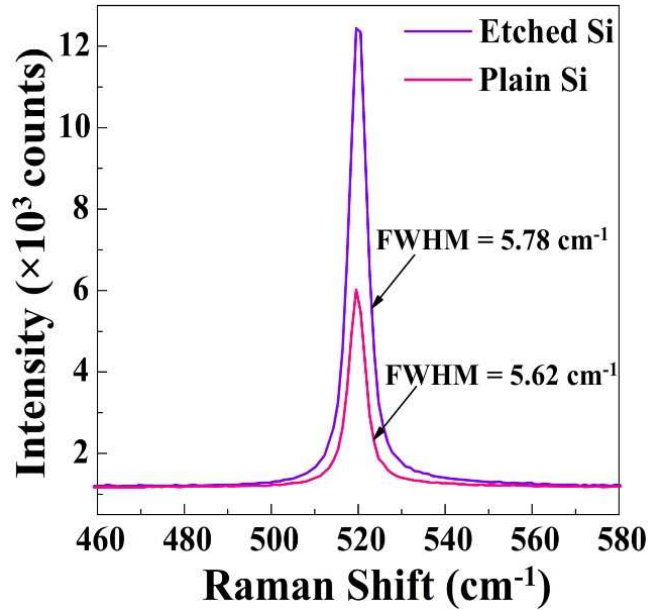


Figure 3.2: Raman spectra of plain and etched Si (100) wafer. Adapted with permission from [44].

silicon samples. For a given acquisition time and laser power, the Raman intensity of the peak at 521 cm^{-1} for plane Si, increase from 6000 counts to approximately 12000 counts (Fig.3.2) for the etched Si ($R_{RMS} = 0.3 - 3 \mu\text{m}$). This enhancement in the Raman signal was observed universally for all the etched Si samples. These results also corroborate that the probability of interaction of laser light with silver nanoparticles increases when Ag: $a\text{-Si}_3\text{N}_4$ nanocermet is deposited on etched Si surface, thus increasing the overall intensity of the SERS signal.

Growth of Ag: $a\text{-Si}_3\text{N}_4$ Nanocermet Thin Film on Anisotropically Etched Si:

A reactive, direct current unbalanced magnetron sputtering system was used for depositing Ag: $a\text{-Si}_3\text{N}_4$ nanocermet thin films from high purity targets of Ag and Si_3N_4 with diameter 0.075 m. A constant substrate temperature of $150 \text{ }^\circ\text{C}$ and a constant pressure of 3.4 Pa were maintained during the deposition of nanocermet on the anisotropically etched silicon. The Ar gas flow rate was 30 SCCM. Initially,

a 10 nm thick layer of silver was deposited by using sputtering power (P_{Ag}) of 20 W. This was followed by a co-sputtering process of deposition of both Ag and Si_3N_4 targets. In the whole process, the sputtering power for Si_3N_4 target was kept constant at 325 W, whereas the sputtering power of silver target (P_{Ag}) was varied from 12 to 18 W. This was done to obtain different composition of silver in the nanocermet thin films. The sample holder was rotated uniformly throughout the process of deposition to achieve highly uniform thin films. The samples were finally annealed in air for 1 h at 500 °C by allowing them to cool down under ambient conditions.

Characterization of NCES-SERS Sensor:

The surface morphology and microstructure were analyzed using field emission scanning electron microscopy (FESEM, Supra 40VP, Carl Zeiss) and 3D surface profilometer (Nanomap). The structural and chemical characterization of the sensor was carried out using X-ray diffraction (XRD, Bruker D8) in thin film mode and x-ray photoelectron spectroscopy (XPS, SPECS). The plasmonic behavior of the sensor was studied using a UV-Vis spectrophotometer (PerkinElmer, Lambda 750).

SERS Measurements:

180° backscattering geometry was used to record Raman and SERS spectra. The excitation source was 532 nm from a diode-pumped frequency-doubled Nd:YAG solid state laser (Photop Suwtech Inc., GDLM-5015 L). The numerical aperture of the lens was 0.45 with a working distance of 17 mm. A custom built Raman spectrometer equipped with an SPEX TRIAX 550 monochromator and a liquid nitrogen cooled CCD were used to record the spectra. Laser power at the sensor was 8 mW without filters and appropriate neutral density filters were used to control the laser power at the sensor. Typical acquisition time was 10-30 s. For obtain-

ing SERS spectra, 10 μl of the analyte solution was dropped on the sensor and allowed to dry. SERS spectra were then collected from three different locations and averaged. In order to study the thermal stability of the sensor, after acquiring the SERS spectra of a given analyte, it was removed by heating the sensor at 450 $^{\circ}\text{C}$ for 15 min (with a heating rate of 10 $^{\circ}\text{C}/\text{min}$). This procedure was repeated 5 times to demonstrate the reusability of the substrate. Similarly, for chemical stability, the sensor was dipped in concentrated HCl solution for 5 min and then washed thoroughly with ethanol. Analyte solution was then added to obtain the SERS spectra of the next cycle.

Finite difference time domain (FDTD) simulations of NCES-SERS sensor:

All the FDTD simulations were performed using Lumerical FDTD Solutions (Trial License). All the data generated from the simulation were plotted in MATLAB. The micro-pyramids were represented by triangles with base length P , and NPs as circles with diameter d , and edge-to-edge NP spacing S . The thickness of dielectric material was $0.7d$, wherein the NPs were embedded to a depth of $0.2d$. A 10 nm interlayer of Ag was also used in the model. The left, and right boundaries of the simulation region were assigned periodic boundary conditions (PBC) (periodicity = P) while the top and bottom boundaries were modeled with perfectly matched layers (PML). Mesh size for the simulation was taken as 2 nm (in both X- and Y- directions) due to computational limitations. A p-polarized light source was introduced at the top with $\lambda = 532$ nm.

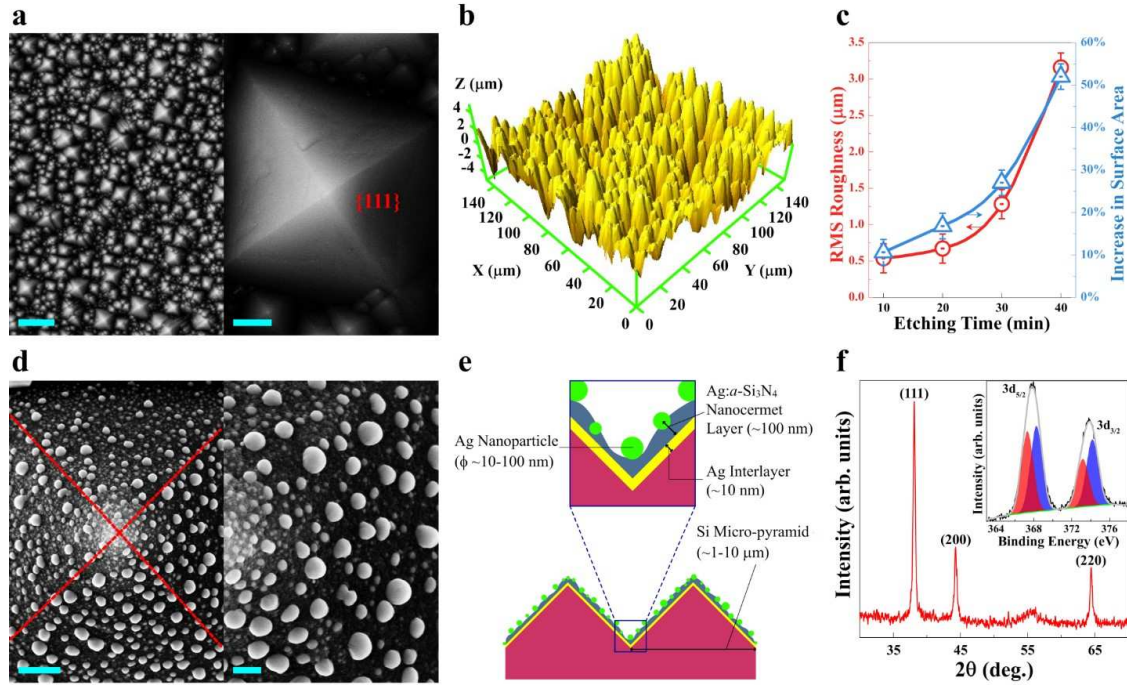


Figure 3.3: NCES-SERS sensor. (a) Low (left) and high (right) magnification FESEM micrographs for the anisotropically etched Si (100) wafer. (scale bar $10 \mu\text{m}$ for the left and $1 \mu\text{m}$ for right) (b) 3D surface roughness profile of an etched Si substrate. (c) Plot of etching time with RMS roughness (left) and the increase in surface area (right). (d) Low (left) and high (right) magnification FESEM micrographs for the NCES-SERS sensor. (scale bar $0.5 \mu\text{m}$ for the left and $0.15 \mu\text{m}$ for right) (e) Schematic representation of the NCES-SERS sensor. (f) XRD pattern of the nanocermet thin film with the crystal planes of Ag marked. The inset shows the XPS spectrum of Ag $3d_{5/2}$ and $3d_{3/2}$ transitions. Adapted with permission from [44].

3.3 Results and Discussions

Micro-pyramids were formed by anisotropic etching of Si (100) wafer. These micro-pyramids had a base width in the range of $1\text{-}10 \mu\text{m}$ [38] and were responsible for micro-scale roughness. The nucleation and growth, and distribution of the silver nanoparticles in the nanocemets was affected by the micro-scale roughness imparted by the micro-pyramids [41]. The pyramidal microstructure results in the formation of valleys that lead to several interesting microstructural and optical properties.

Fig.3.3b is a 3D surface profile for the etched Si surface. The average height of the micro-pyramids was uniformly distributed throughout the surface. The root-mean-square roughness (R_{RMS}) for these samples was in the range of 0.54 -3.15 μm and was controlled by changing the duration of etching. Fig.3.3c shows a plot of (R_{RMS} and the duration of the anisotropic etching along with the corresponding increase in the surface area. Fig.3.3d shows the FESEM micrograph of NCES-SERS sensor at high magnification. The edges of the Si micro-pyramid beneath the nanocermet thin film are depicted by dashed lines. The nanocermet film comprises of the silver nanoparticles dispersed in a-Si₃N₄ matrix. The average NP size was found to change with the power that was applied to the Ag target (P_{Ag}) during deposition, as well as (R_{RMS} of Si substrate. The NP sizes were in the range of 10-100 nm.

A 10 nm thick interlayer of Ag was deposited on the etched Si surface. It reduced absorption of light in the underlying Si substrate and caused multiple reflections of light. Thin film XRD (Fig.3.3f) shows the characteristic crystal planes of the polycrystalline Ag and confirms the presence of silver nanoparticles in the nanocermet thin film. Si₃N₄ was amorphous in nature and hence its peaks were not detected in the XRD. Silver nanoparticles were surface oxidized due to heating at 500°C for 1 h. This was confirmed by XPS [45],[46]. The peaks of the core level spectra were deconvoluted to confirm the presence of AgO (367.3 and 373.2 eV, red) and Ag (368.3 and 374.2 eV, blue) (Fig.3.3f). Majority of Ag was in the metallic state as no oxide peaks were observed in the XRD data.

Fig.3.4 shows the variations in the AgNP size distribution with P_{Ag} (a-c) and R_{RMS} of the etched Si (d-f), respectively. The corresponding UV-Vis spectra are provided as inserts. UV-Vis spectra have correlation with the distribution of sizes of nanoparticle. The different NP sizes give rise to different dipole plasmon modes.

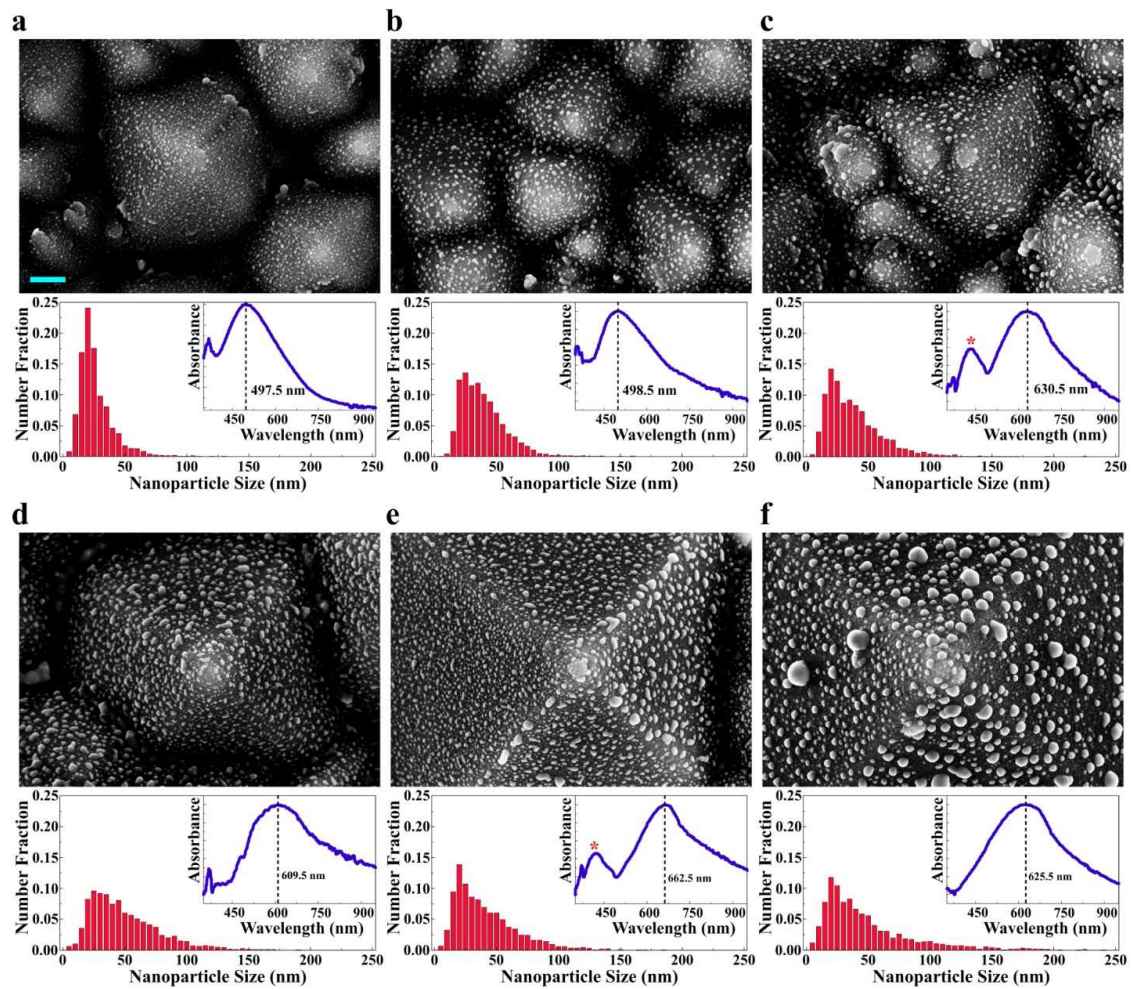


Figure 3.4: Dependence of surface plasmon resonance on the NP size and distribution. FESEM micrographs (scale bar = $0.5 \mu\text{m}$), NP size distribution histograms and the UVvis absorbance plots (inset) for the NCES-SERS sensors at RMS surface roughness, $R_{RMS} = 0.63 \mu\text{m}$ but different Ag target power levels: $P_{Ag} =$ (a) 12, (b) 14, and (c) 16 W. Fig. d-f are at constant Ag target power, $P_{Ag} = 18$ W but different RMS surface roughness: $R_{RMS} =$ (a) 0.54, (b) 1.28, and (c) 3.15 μm . Adapted with permission from [44].

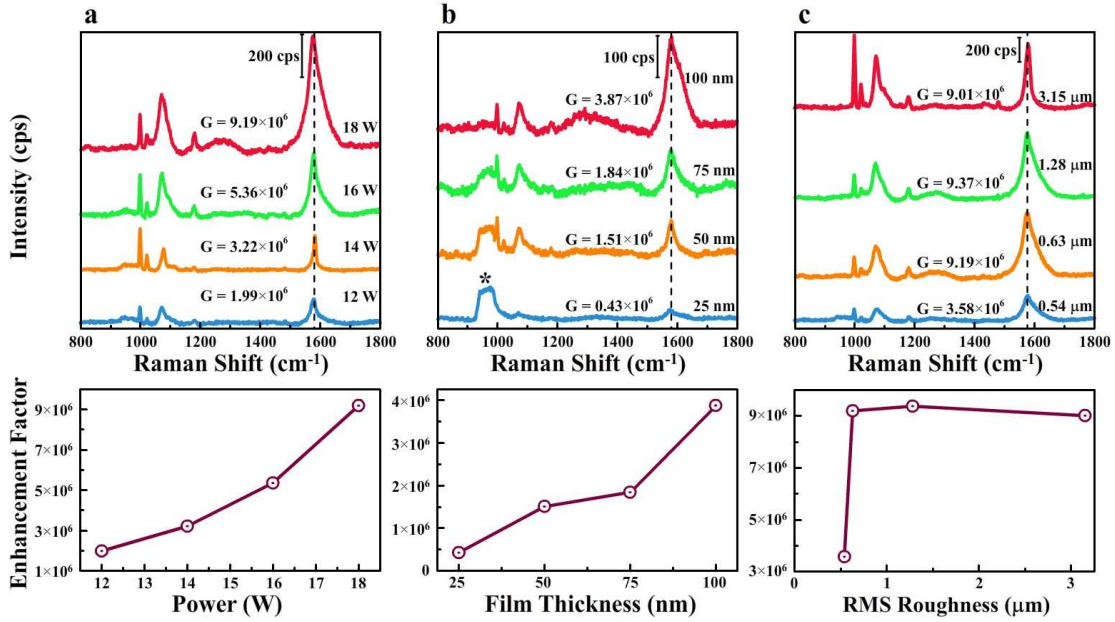


Figure 3.5: SERS spectra for the NCES-SERS sensors prepared by varying different experimental parameters: (a) Ag target power, (b) film thickness, and (c) RMS surface roughness. PhSH is used as a model analyte. (d) The variation in the SERS enhancement factors (written as En. Factor) for NCES-SERS sensors calculated from the SERS plots in parts ac. Adapted with permission from [44].

With increase in the average size of nanoparticle (increase in P_{Ag}), the dipole plasmon gets red-shifted [29],[47]. There is no major shift in the dipole plasmon peak, this shows that the size of nanoparticles is independent of the pyramid size. Due to shadowing the effect during the sputtering process, the distribution of silver nanoparticles varied with different etched planes [48]. An additional dipole plasmon mode was observed at lower wavelengths in the UV-Vis spectra. This quadrupole plasmon mode (*) led to two major size distributions of silver nanoparticle. Bigger sized NPs often give rise to plasmon bands that are red shifted due to electromagnetic retardation effect [49],[50].

Thiophenol (C_6H_6S or PhSH), was used as a model analyte for calculating SERS enhancement factor (G) [51]. Different process parameters like Ag target

power, film thickness, and surface roughness were used to fabricate NCES-SERS sensor. These parameters were varied, and their effects on SERS was studied by plotting enhancement factors. Inhomogeneous broadening of Raman peaks (or the differences in their relative scaling) was observed due to the "many molecule" SERS effects [52]. The enhancement of a particular mode depends on the orientation of the polarizability component with respect to the NP surface (maximum when perpendicular) [53]. The surface of NCES-SERS sensor was fairly homogeneous, in terms of its AgNP distribution, and displayed similar SERS spectra at randomly selected locations (Fig.3.6)

The enhancement factor was calculated by the following relation:

$$G = \frac{I_{SERS}}{I_{RS}} \times \frac{N_{VOL}}{N_{SURF}} \quad (3.5)$$

where I_{SERS} and I_{RS} are the intensities from SERS and Raman spectroscopy (RS) of the analyte for a specific peak (e.g. 1580 cm^{-1} in the present work). N_{VOL} and N_{SURF} are the number of molecules in the scattering volume and the surface of the NPs, respectively. N_{SURF} is given by CA , where C and A are the surface coverage density of PhSH molecules (6.8×10^{14} molecules per cm^2) and the laser spot area ($4 \mu\text{m}^2$), respectively. N_{BULK} is given by $Ah\rho m$, where h , ρ and m denote the penetration depth ($100 \mu\text{m}$), the density (1.079 g/cm^3) and the molecular weight (110.18 g/mol^1) of the PhSH, respectively.

Highly aggregated silver based nanostructures with non-uniform hot spots can show enhancement $G > 10^8$ [34],[31]. NCES-SERS has fairly uniform distribution of AgNPs anchored in $\alpha\text{-Si}_3\text{N}_4$ matrix. It has enhancement factor in the range of $10^6 - 10^7$ for PhSH. The nanoparticles in the nanocermet, do not aggregate and are thermally and chemically stable. The variations in the size and distribution of Ag-

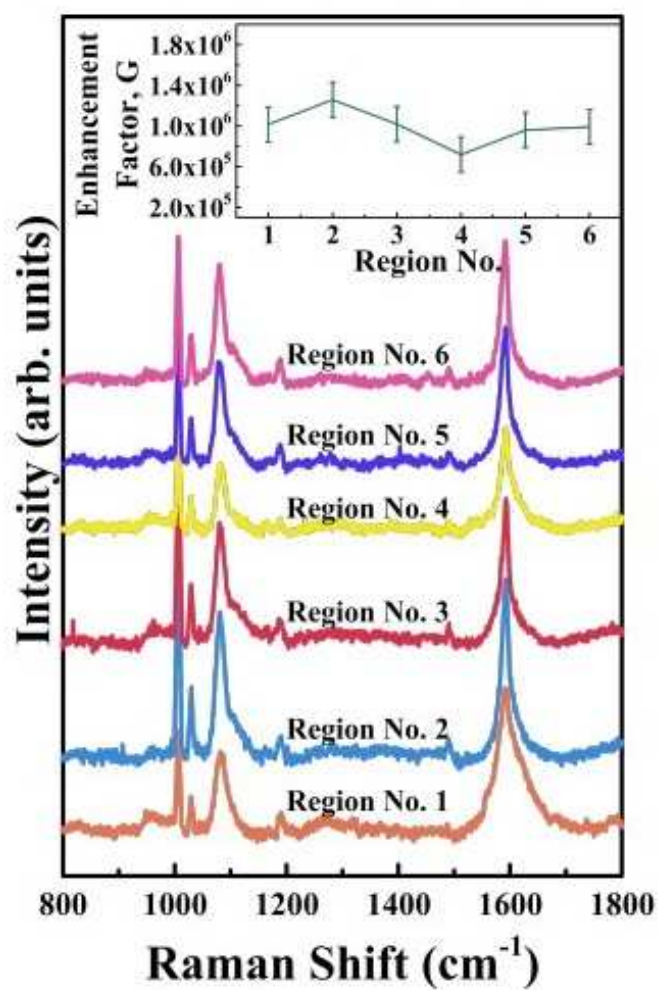


Figure 3.6: Homogeneity of AgNP distribution. SERS spectra of thiophenol at six randomly selected regions of the NCES-SERS sensor, displaying low variation in peak intensities. Adapted with permission from [44].

Table 3.1: Assignment of SERS for PhSH (Thiophenol)

Raman shift(cm^{-1})	Band assignment
1001	In plane ring deformation + C-C stretching mode(ν_{CC})
1027	In plane ring deformation + ν_{CC} + C-H deformation(δ_{CH})
1077	In plane ring deformation + ν_{CC} + δ_{CH}
1576	C-C stretching

Table 3.2: Assignment of SERS for R6G (Rhodamine 6G)

Raman shift(cm^{-1})	Band assignment
886	$C_X - C_X - H$ bending
925	$C_X - C_X - C_X$ bending
1149	$C_E - H$ bending
1196	$C_X - C_X$ stretching
1316	$C_X - H$ bending
1364	$C_X - C_X$ stretching
1520	$C_X - C_X$ stretching
1588	$C_X - C_X$ stretching
1664	$C_X - C_X$ stretching

NPs, lead to changes in SERS enhancement factors. As the size of AgNPs increases with P_{Ag} and the film thickness (t_{film}), an increase in G is observed as depicted in Fig.3.5. As size and distribution of nanoparticles are independent of pyramid size (in other words, R_{RMS}), the enhancement factor (G), was also independent of R_{RMS} . On increasing t_{film} , second-order Raman peak of Si, decreases in intensity (Fig. 3.5b). The optimum conditions for maximum SERS signal enhancement were found to be $P_{Ag} = 18$ W, $R_{RMS} = 1.33 \mu\text{m}$ and $t_{film} = 100$ nm. The variation in the SERS enhancement factors has also been plotted separately in Fig.3.5d to illuminate its dependence on the process parameters.

Nanocermets can be used for high-temperature SERS studies as they are stable at high temperature and have high melting point [53]. Using thiophenol as a model analyte, high-temperature SERS were done up to 450°C. Thiophenol disintegrates completely and evaporates in the air at such high temperatures. There were no

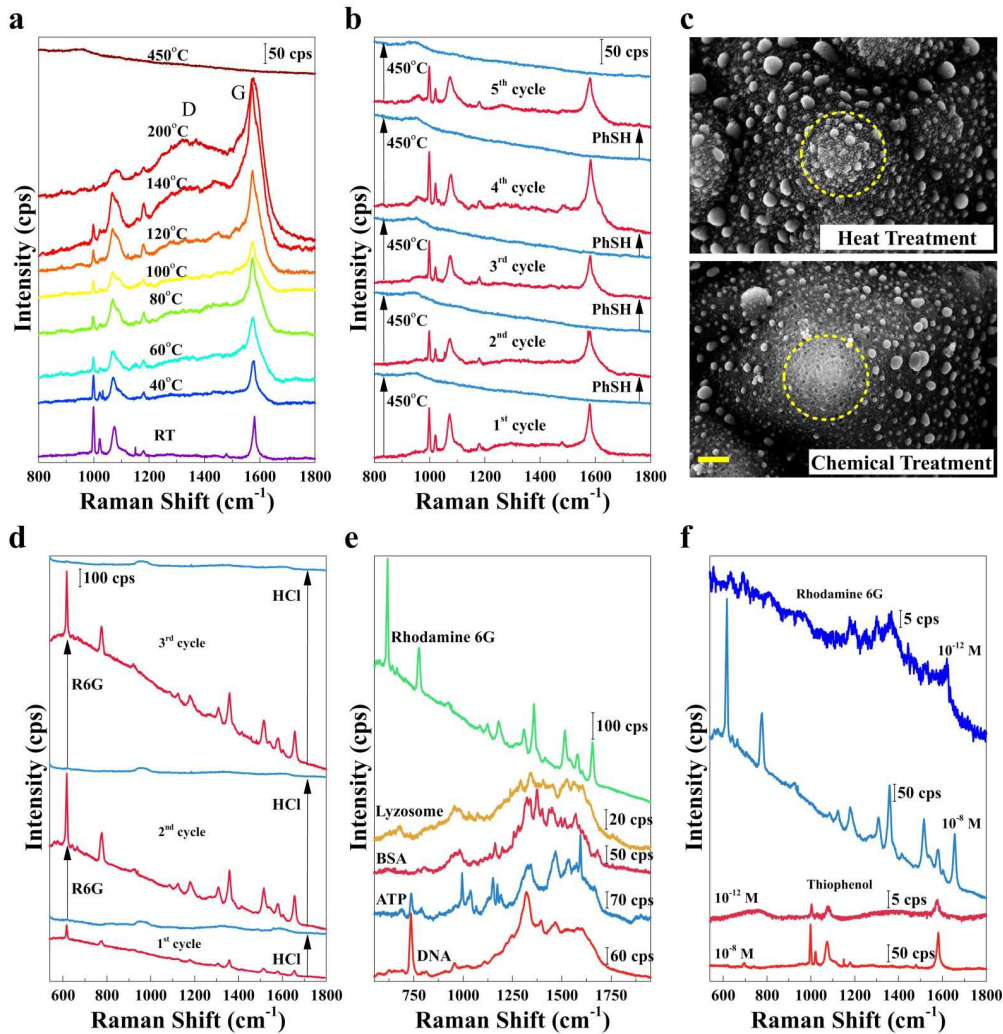


Figure 3.7: (a) Temperature dependent SERS spectra of thiophenol from room temperature (30°C) to 450°C for the NCES-SERS sensor. (b) Reusability of the sensor through heat treatment for 5 cycles, where red and blue represent SERS spectra after drop coating and heating up to 450°C in air, respectively. (c) FESEM micrograph of heat treated (5 cycles) and chemically treated sample depicting their effect on the distribution of AgNPs (secondary growth). (d) Reusability of the sensor through chemical treatment for 3 cycles, where red and blue represent SERS spectra after drop coating and HCl wash for 5 min, respectively. FESEM micrograph of chemically treated (3 cycles) sensor with leaching of AgNPs. (e) SERS spectra of different biomolecules. (f) Demonstration of high sensitivity by low (10^{-8} M) and ultra-low (10^{-12} M) concentration of PhSH and R6G. Adapted with permission from [44].

Table 3.3: Assignment of SERS for ATP (adenine triphosphate)

Raman shift(cm^{-1})	Band assignment
686	NH_2 out of plane wagging mode
734	Adenine ring breathing mode
1041	Ribose vibrational mode
1334	Adenine

Table 3.4: Assignment of SERS for DNA (Deoxyribonucleic Acid)

Raman shift(cm^{-1})	Band assignment
773	Adenine
959	Sugar phosphate chain, Deoxyribose
1328	Adenine
1400	Adenine, Thiamine, Guanine
1457	Deoxyribose, CH_2
1576	A(ring stretching), NH_2 deformation

Table 3.5: Assignment of SERS for lysozyme

Raman shift(cm^{-1})	Band assignment
671	$\nu(C - S)$
960	Tyrosine
1030	Phenylalanine
1076	$\nu(C - N)$
1296	Amide III
1348	Tryptophan
1413	δCH_2
1519	Amide II
1561	Tryptophan, Histidine
1600	Phenylalanine, Tyrosine

Table 3.6: Assignment of SERS for BSA (Bovine Serum Albumin)

Raman shift(cm^{-1})	Band assignment
1167	Tyrosine
1205	Tyrosine, Phenylalanine
1266	Amide III
1282	Amide III
1327	Tryptophan
1375	Tryptophan
1459	δCH_2
1512	δCH_2
1569	Tryptophan
1611	Tyrosine, Tryptophan
1679	C=O stretch, Amide I

observable peaks in the SERS spectra of thiophenol at 450°C (Fig.3.7a). Due to the stability of nanocermets at high temperature, the NCES-SERS sensor was also stable at 450°C. This was proved by repeating SERS of thiophenol at room temperature. The SERS spectra of thiophenol were similar to the one obtained prior to heating. The sensor was heated again till 450°C and SERS measurements were done. This cycle was of experiments of heating and cooling the NCES-SERS sensor and then recording the SERS spectra of thiophenol was repeated 5 times. The SERS intensity for thiophenol remains almost constant in each cycle. These results prove the stability of the sensor at high temperature and its reusability. The NCES-SERS sensor subjected up to 5 cycles of annealing was further examined under FESEM, and the corresponding micrograph is shown in Fig.3.7c, highlighting the anchoring effect of $\alpha-Si_3N_4$ matrix.

The reusability of the NCES-SERS sensor through chemical treatment (HCl immersion and wash) was also investigated (Fig.3.7d). In this case, Rhodamine 6G (R6G) dye molecule was used as a model analyte instead of thiophenol. Unlike thiophenol, Rhodamine 6G does not form a direct covalent bond with Ag and hence it can be removed easily by chemical wash. The sensor was dipped in HCl for 5

minutes. This led to the removal of native oxide layer on the surface of silver nanoparticles which increased the intensity of SERS signals from R6G analyte molecule [46],[45]. The NCES-SERS sensor was again examined under FESEM after three such cycles of acid wash. The FESEM micrograph (Fig.3.7c, bottom) taken indicates slight leaching and displacement of the silver nanoparticles. This is expected to deteriorate after subsequent cycles, thus limiting its reusability through chemical route. Contrary to this, the reusability through heat treatment does not lead to any significant changes in the size and distribution of silver nanoparticles. Therefore, the reusability through heat treatment is better than commonly used chemical treatment.

SERS measurements for different analytes of biological significance were done to demonstrate the versatility of NCES-SERS sensor (Fig.3.7e). The detailed SERS peak assignments are provided in the tables 1,2,3 and 4. Two important classes of biomolecules were investigated, namely proteins [lysozyme (table 5) and bovine serum albumin, BSA (table6)] and nucleic acids (deoxyribonucleic acid, DNA)(table 4). The SERS spectrum of adenosine triphosphate (ATP) was also studied (table 3), which is of common interest because of its central role in biological energy transfer reactions [54]. The NCES-SERS sensor was also used to sense low concentration (10^{-8} M) of genomic DNA as well as molecular ATP and have obtained unique fingerprints of these molecules which might be used for multiplex detection [55],[56],[57]. NCES-SERS sensor can be used to detect two differently charged protein molecules, lysozyme (pI = 11.35) and BSA (pI = 4.9). The conventional colloidal based SERS nanoparticles have charged capping agents [35],[36],[58],[37], and it becomes very difficult for the proteins molecules to displace these charged capping agents before getting attached to the nanoparticles. If the capping agent and protein have similar surface charges, then it is not possible

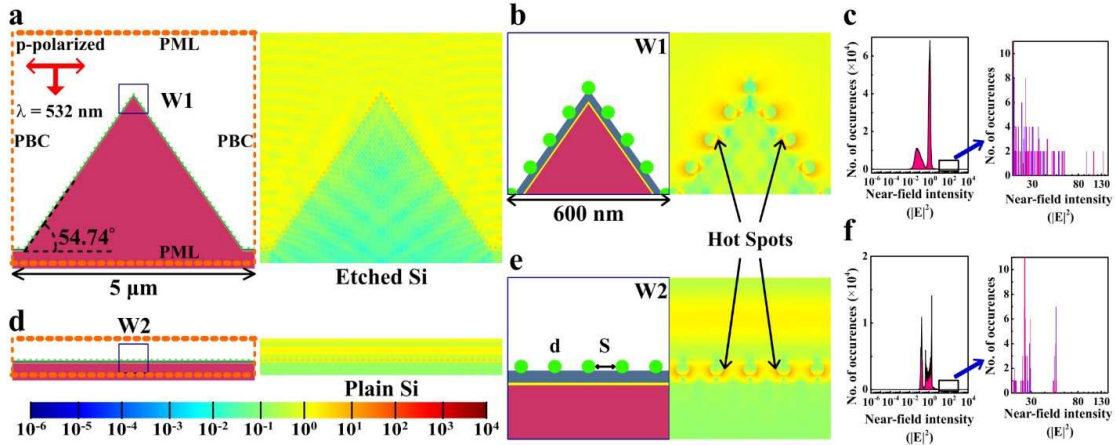


Figure 3.8: (a) Schematic representation of the 2D FDTD simulation model used to simulate the conditions for the etched Si sensor and the corresponding FDTD field intensity plot. (b) Magnified view of the simulation model (shown as W1 in part a) and the corresponding view of the FDTD field intensity for the etched Si sensor model. (c) Near-field intensity distribution for the etched Si sensor model and a magnified view for the higher intensities (hot spots). For a comparison, parts d-f give the corresponding results for plain Si sensors as parts a-c, respectively. The color bar at the bottom gives the near-field intensity values. Adapted with permission from [44].

to displace these capping agents. Hence, it is not possible to detect differently charged protein molecules using same colloidal nanoparticles. The bare nanoparticles surface of the sensor does not form complexes with biomolecules (as delicate as proteins) due to its chemical stability, which is an important criterion for their detection. NCES-SERS sensor exposes more molecular surface area for SERS enhancement by accommodating large sized biomolecules like proteins and DNA in the gaps between AgNPs. The possibility of detecting fluorescence molecules like R6G, which are used for tagging biological molecules (fluorometric detection), was also demonstrated by our NCES-SERS sensor. SERS spectra of PhSH and R6G were acquired for ultra-low concentrations, to test the SERS detection limit of the NCES-SERS sensor. Both the analytes with all their characteristic peaks were detected up to 10^{-12} M concentrations (Fig.3.7d).

To understand the plasmonic behavior of the NCES-SERS sensor, 2D finite difference time domain (FDTD) simulations were performed. The unique microstructure of etched Si and the AgNP distribution of our NCES-SERS sensor provides interesting prospects for observation of distinctive plasmonic behavior due to the light trapping phenomenon [59],[60],[38]. The near field intensity ($|E|^2$) obtained from the FDTD simulations can be directly correlated to $G (\propto |E|^4)$ [30]. In NCES-SERS sensor, there was a variation in the size and shape of the silver nanoparticles and size of the micro pyramid as well as spacing between the two nanoparticles. It is a very challenging task to realistic model these effects, so these parameters were theoretically modeled, individually, to study their effects on the near field intensities [61]. The simulation parameters for the nanocermets on etched and the plain Si SERS sensors designed under identical conditions are shown in Fig.3.8. The FDTD near field intensity color plots in Fig.3.8a, b, d, and e correspond to the parameters: NP size, $d = 50$ nm, pyramid size, $P = 5 \mu\text{m}$, and spacing $S = 75$ nm, based upon the average values from the FESEM data of the NCES-SERS sensor. Fig.3.8 band c shows the distribution of the hot spot in the magnified regions W1 and W2. The distribution of $|E|^2$ was calculated based upon the number of occurrences of hot spots in the simulation area for etched and plain sensors (Fig.3.8c and f). Due to larger simulation area for the etched Si, the total number of occurrences was significantly more as compared to the plain Si. Therefore, the near field intensity distribution for higher values was magnified, and the data is shown adjacent to the corresponding distributions. The occurrence of higher field intensities is more prominent for the etched sensor, which leads to more enhancement in the SERS signal than the plain sensor. The simulation parameters were also varied individually to study their influence on the near field intensities. From these results, it can be inferred that the optimum NP size should be in the

range of 50100 nm, which is also consistent with the experimentally determined NP size. Furthermore, the simulation predicts that smaller pyramids ($P = 15 \mu\text{m}$) lead to more number of hot spots due to multiple reflections of the electromagnetic radiation. The near field intensities are very strong when the nanoparticles were very closely spaced. This leads to stronger plasmonic coupling [62]. At 532 nm, Si_3N_4 and Al_2O_3 yielded relatively higher near-field intensities than SiO_2 . This may be because of their higher refractive indices at 532 nm. Therefore, from the simulation results the distribution of the near-field intensities and the locations of the hot spots, can be linked to the characteristics of the real NCES-SERS sensor in understanding its plasmonic behavior.

3.4 Conclusions

The unmatched capability of the NCES-SERS sensor was successfully demonstrated. It has a very high degree of robustness and reusability due to its unique micro-/nanostructure. It provides high enhancement in the SERS signal of various analytes. There was a fairly uniform distribution of the AgNPs on Si micro pyramids which responsible for imparting many optical properties and plasmonic behavior to the sensor. Thiophenol was used as a model analyte for calculating enhancement factors of the sensor. Very high enhancement factors (10^6 to 10^7) were achieved by optimizing the fabrication parameters. This was substantiated by the 2D FDTD simulations. The NCES-SERS sensor is stable at high temperature and can work up to 500°C in air. It has a very low detection limit, analytes like R6G and thiophenol were detected at low concentration of 10^{-12}M . The charged analyte molecules (e.g., lysozyme and BSA) do not face any repulsion and are directly accessible to the NP surface. This is due to the bare and neutral nature of the

AgNPs (no capping agents). This helps in the detection of complex biomolecules such as DNA and proteins. The FDTD simulation results predict that the process parameters for the fabrication of NCES-SERS sensor can be further fine-tuned to obtain very high sensitivity capable of detecting $\leq 10^{15}$ M concentration levels.

CHAPTER 4

SURFACE ENHANCED RAMAN

SPECTROSCOPIC INSIGHTS INTO AN

INTERACTION OF SERUM ALBUMINS WITH

DIHYDROPYRIDINE BASED HYPERTENSIVE

DRUGS

4.1 Introduction

Emergence of Raman spectroscopy to study biological systems has enabled it to be used as an effective tool for studying biomolecular interactions [63]. The ease of instrumentation and the versatility of its use have made this technique more and more attractive to biophysicists. It is slowly emerging as one of the most common characterization tools in conjunction with other popular techniques like fluorescence, circular dichroism, and infrared spectroscopy [64]. The strength of Raman spectroscopy lies in the fact that both secondary structural information and bond vibrational information can be obtained in a single spectroscopic analysis, whereas in the case of fluorescence and circular dichroism, such detailed bond specific information cannot be elucidated [65]. Although X-ray crystallography and

NMR has been used to study protein-ligand binding, they too suffer from difficulties like good diffracting single crystal of the protein or the protein size. Therefore, there was a need to develop a simple and easy information-rich technique like Raman spectroscopy which can be used to study protein-ligand binding. But one of the major drawbacks of normal Raman spectroscopy is the low scattering cross sections which are an impediment in studying of the biomolecular systems. This is where the advent of the surface enhanced Raman spectroscopy (SERS) becomes important [66]. The Raman scattering cross section is greatly enhanced when a molecule is placed in the vicinity of a plasmonic nanostructure made of gold, silver or copper [67]. The enhancement from the SERS can be further enhanced by coupling of the nanostructures due to their proximity to each other creating the hotspots which are areas of intense electromagnetic field between the nanostructures which are below 10 nm in separation. Since SERS can be performed with a very low concentration of analytes and also in physiological conditions it is increasingly being used in the field of biology for developing some new diagnostic techniques and also for monitor biochemical processes [68]. The sensitivity of this technique can reach single molecule level detection, and complex molecules like proteins can also be studied [63]. In the past SERS studies have been conducted by our group to study protein-small molecule interactions involving biologically relevant proteins like p300 [69], CARM1 [70], and Aurora Kinases [71].

Serum albumins are the most abundant proteins found in mammals. Human serum albumin (HSA) is a globular protein which consists of three homologous domains, namely I, II and III. Each one of these domains can be divided into A and B subdomains. In the case of HSA, it has been shown that the ligand binding hydrophobic cavities are located in subdomains IIA and IIIA [72]. A single Trp-214 residue belonging to subdomain IIA is also responsible for ligand binding [73].

This protein is the carrier of drugs in the bloodstream and amplifies the transport of endogenous and exogenous substances. The analogues of HSA found in other animals also perform similar functions. This class of protein forms a model to study protein-molecule binding and provides useful information on possible modes of interactions of the molecule to biological systems and also the transportation behavior of drugs.

Amlodipine and nimodipine are a class of calcium channel blockers with vasodilating activity. These molecules are used in the treatment of hypertension, cerebrovascular diseases and angina pectoris [74]. Here the two similarly structured proteins and drug molecules are chosen to study the minute differences in binding which can be picked by the highly sensitive SERS technique. We have used citrate capped silver nanoparticles which have the capability for providing highest enhancement for biomolecular systems. The proteins and the nanoparticles were attached using electrostatic attraction by modulating the charges through introduction of ions. This type of interaction helps retain the activity of protein which has been demonstrated earlier in our studies [71]. The ability to differentiate between the binding modes is significant as it can lead to the development of a fast SERS based screening tool.

4.2 Experimental methods

Materials: Human serum albumin (HSA), amlodipine, nimodipine, silver nitrate, and sodium citrate were obtained from Sigma-Aldrich and used as obtained. HSA was dissolved in 10mM phosphate buffer of pH 7.4. MilliQ water was used for all preparations. Nimodipine and amlodipine were dissolved in dimethyl sulphoxide (obtained from SD Fine, India).

Preparation of silver nanoparticles: Citrate capped silver nanoparticles were prepared by Lee-Meisel method. Initially, 18 mg of silver nitrate was dissolved in 100 ml of water and brought to boiling point. 2 ml of 1% aqueous sodium citrate was added to it and stirred vigorously. After 1 hour, the heat was turned off, and the solution was brought to room temperature while stirring. The colloid was characterized by transmission electron microscopy (TEM) (JEOL JEM 3010) and UV-vis absorbance spectroscopy (as described in Chapter 2).

SERS measurements: SERS spectra were obtained by using a custom made Raman setup in an 180° backscattering geometry. A 532 nm Nd-YAG solid state laser was used as an excitation source. A custom built Raman spectrometer equipped with an SPEX TRIAX 550 monochromator and a liquid nitrogen cooled CCD were used to record the spectra. A 3 cm^{-1} resolution was achieved by using a holographic 1800 grooves mm^{-1} along with a $200\ \mu\text{m}$ spectrograph entrance slit settings. For SERS measurements of the aqueous protein solution, a 20x air objective lens was used. The laser power achieved at the sample was typically 5 mW. The accumulation time for each spectrum was typically 30s.

Molecular docking simulations: The crystal structures of BSA and HSA used for simulations were obtained from protein data bank (PDB) with IDs 1MQ4 and 4AF3 respectively. The structure of the drug molecules, amlodipine, and nimodipine were obtained from ZINC. Docking analysis was performed by using Autodock 4.2 software. Lamarckian genetic algorithm was used for the simulations with a grid spacing of $0.375\ \text{A}^\circ$. Ligands used were rendered flexible, and 100 GA runs with a population size of 300, 25 X 105 evaluations and a maximum of 27000 generations were utilized in each simulation to generate favorably bound configurations of the ligand. The analysis of the conformations was done using MGL Autodock tools ver 1.5.4 and the protein figures were generated using the

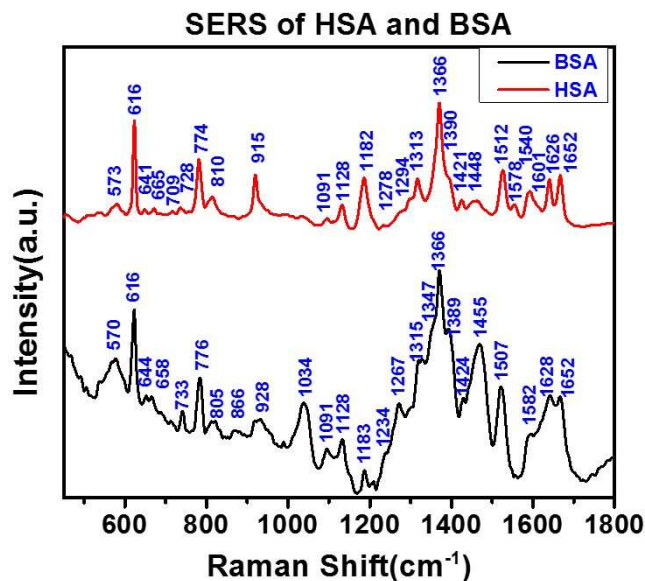


Figure 4.1: SERS spectra of HSA and BSA

PyMOL molecular graphics system.

4.3 Results and Discussions

SERS of HSA and BSA: The band assignment has been done in accordance with the available literature on the SERS spectra of amino acids and proteins (Fig.4.1). Table 1 and Table 2 give the detailed tentative SERS band assignments for both the proteins HSA and BSA and also their deuterated forms [75–78].

Aromatic amino acids: Aromatic amino acids like Tyrosine, Phenylalanine, Tryptophan and Histidine give strong SERS due to the high polarizability of the π electrons. The modes at 1182 and 1578 and 1601 cm^{-1} in the SERS spectra of HSA can be assigned to combination of in-plane CH bending (ν_{9a}) with ring stretching and phenyl C stretching (ν_{8a}) of the Phenylalanine amino acid. The corresponding modes in BSA are observed at 1034, 1183 and 1582 cm^{-1} . The mode at 1034 cm^{-1}

Table 4.1: The tentative Raman band assignments of SERS for the human serum albumin (HSA) protein

HSA	Deuterated HSA	Tentative Band assignment
573	578	Trp
616	616	COO^- wagging
641	641	Tyr/C-C twisting
728		Trp/ $\delta(COO^-)$
774	774	Trp(H19) or His
810		Tyr and/or $\nu_{as}(C - S - C)$
915	916	$\nu(COO^-)$ / C-C stretch of Pro Ring
1091	1091	$\nu(C\alpha - N)$
1128	1128	$\nu_{as}(C\alpha CN)$
1182	1184	Tyr and/or Phe(ν_{9a})
1278	1278	Amide III / $C - C\alpha - H$ deformation
1294		Amide III
1313	1312	CH_2 wagging/ $\delta(C - H)$
1366	1366	Trp
1448	1448	(CH_2) / $\delta(C - H)$
1512	1511	Amide II
1540	1540	Trp w3
1578	1578	$\nu_{as}(COO^-)$, His, Trp, Phe
1601	1602	Phe
1626		Amide I
1652	1653	Amide I

Table 4.2: The tentative band assignments of SERS for the Bovine Serum Albumin (BSA) protein

BSA	Deuterated BSA	Tentative Band assignment
570	578	Trp
616	616	COO^- wagging
644	643	Tyr/C-C twisting
733	734	Trp/ $\delta(COO^-)$
776		Trp(H19) or His
805	806	Tyr and/or $\nu_{as}(C - S - C)$
928	928	$\nu(COO^-)$ / $\alpha - helix$ stretch (C-C)
1034	1034	Phe (ν_{18a})/ C-N stretch
1091	1090	$\nu(C\alpha - N)$
1128	1132	$\nu_{as}(C\alpha CN)$
1183		Tyr and/or Phe(ν_{9a})
1205		Tyr /Phe
1234		Amide III
1267	1272	Amide III / $C - C\alpha - H$ deformation
1294		Amide III
1315	1312	CH_2 wagging/ $\delta(C - H)$
1347	1342	Trp/ $C\alpha - H$ bend and $C - C\alpha$ stretch
1366	1370	Trp
1424	1425	(CH_2) / $\delta(C - H)$
1448	1448	(CH_2) / $\delta(C - H)$
1507	1505	Amide II
1540	1540	Trp w3
1582	1584	$\nu_{as}(COO^-)$, His, Trp, Phe
1601	1602	Phe
1621	1628	Amide I
1652	1653	Amide I

is from the in-plane CH bending (ν_{18a}) [78; 79]. The phenylalanine usually shows a strong peak around 1000 cm^{-1} , arising from the symmetric ring breathing of benzene ring. This is absent in both the proteins. In SERS, intense ring-breathing and CH stretching vibrations are observed when the benzene ring of the aromatic amino acids are oriented at a tilt angle of 90° (normal) to the nanoparticle surface. So it can be inferred that the benzene ring is oriented parallel (or close to parallel) to the nanoparticle surface for both HSA and BSA. Tyrosine shows a doublet due to the Fermi resonance. In SERS, these are around 829 and 847 cm^{-1} . But in proteins, this doublet is not very pronounced, and the lower-frequency mode is very weak. In the case of BSA, the higher frequency mode of the doublet was observed at 866 cm^{-1} for BSA, while in the case of HSA, we were unable to see the higher frequency mode, but a strong peak at 810 cm^{-1} is observed, which can be assigned to the lower frequency mode of the doublet of the tyrosine. It is the B_{1g} mode of tyrosine and is observed when the face of the ring is tilted to the nanoparticle surface. Peaks corresponding to tryptophan were seen at the modes 573 , 728 , 774 (H_{19}) and 1366 cm^{-1} for HSA and 570 , 733 , 776 (H_{19}) and 1366 cm^{-1} for BSA. The modes observed at 774 and 776 cm^{-1} in HSA and BSA, respectively would also have contributions from the histidine as well.

Aliphatic side chain vibrations In vibrational spectroscopy, below 1500 cm^{-1} is called the fingerprint region and is mostly crowded and has a lot of overlapping frequencies. This is also the region for the aliphatic side chain vibrations. Glutamic acid and aspartic acid show a stretching vibration of C-COO as a doublet in the SERS spectra. Surprisingly, for both HSA and BSA we do not observe the doublet. Instead in HSA, we observe only the lower frequency mode at 915 cm^{-1} , while, in BSA we observe on the higher frequency mode at 928 cm^{-1} . It is common to see an overlap of ν_{as} (COO^-) of aliphatic side chains stretching vibration with bands

from histidine, tryptophan and phenylalanine at 1578 and 1582 cm^{-1} for HSA and BSA respectively. In the case of SERS, CH_2 deformation vibration appears at 1448 and 1455 cm^{-1} for HSA and BSA, respectively. The 1312 and 1315 cm^{-1} bands seen in HSA and BSA, respectively are assigned to CH_2 wagging vibration. C-N stretching mode is observed around 1034 cm^{-1} in the case of BSA and has an overlap with phenylalanine ring mode. At the same time, we do not see any band in this region related to C-N stretching mode in the case of HSA. Here it should be emphasized again that the absence of a expected peak in SERS is driven due to the different selection rules governing SERS compared to Raman. The $\nu(C\alpha - CN)$ band from $C - NH_2$ vibrations, appears at 1091 cm^{-1} and the $\nu_{as}(C\alpha CN)$ band appears at 1128 cm^{-1} for both HSA and BSA. The mode of $C\alpha - H$ bending and $C - C\alpha$ stretching were observed at 1347 cm^{-1} for BSA, but it difficult to see in HSA as it is masked by the 1366 cm^{-1} peak.

Amide vibrations Amide bands are related to the vibrations associated with peptide bonds and hence are highly sensitive to the secondary structure of the proteins. CO stretching vibrations along with some contribution from in-plane N-H bending predominantly represent Amide I band, but it also has some contributions from out of phase CN stretching vibration and C-CN deformation and is seen both in Raman and SERS of proteins. Similarly, the combination of NH in-plane bending and the CN stretching vibrations form the Amide II vibration with small contributions from CO in-plane bend and the CC and NC stretching vibrations. Amide II is Raman inactive but is active in SERS spectra of proteins. On the other hand, the amide III vibration is the combination of the in-plane bending of NH bending and CCN stretching vibration with small contributions from CO in-plane bending. This vibration in proteins is weak in both Raman and SERS but present in both the cases for protein samples. The Amide vibrations have contributions from

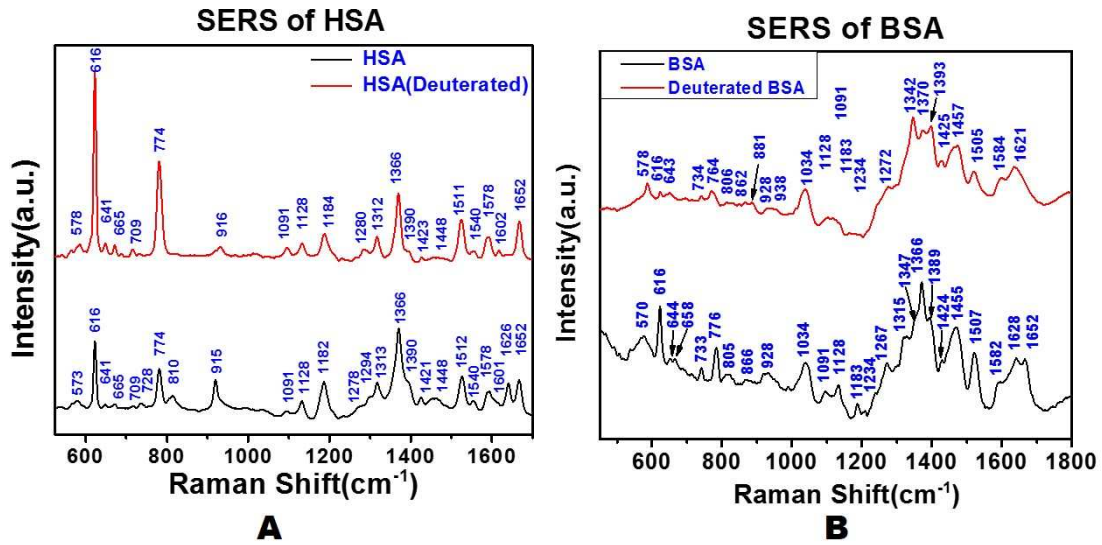


Figure 4.2: A: SERS spectra of HSA and Deuterated HSA; B: SERS spectra of BSA and Deuterated BSA

α -helix, β -sheets (both parallel and antiparallel), and random coils hence need de-convolution of the spectra to assign. In Raman there is contributions from all of them are present, and their intensities are depending on their percentage presence in the protein structure, but since SERS is a distance-dependent phenomenon, the contributions from those groups of secondary structures which are closest to the nanoparticle surface have larger intensity. Sometimes there may be no contribution from the secondary structures even though they are present due to them being very far from the nanoparticle surface (> 1 nm). For HSA and BSA, amide I bands are seen at 1626 and 1652 cm^{-1} in both the proteins. The sharp and intense band at 1626 cm^{-1} could be assigned to anti-parallel β -sheet whose band position is near 1620 cm^{-1} in Raman and IR spectra. Amide II band appears at 1512 and 1507 cm^{-1} in HSA and BSA, respectively. The peaks at 1234, 1267, 1278 and 1294 cm^{-1} can be assigned to Amide III for both HSA and BSA, respectively.

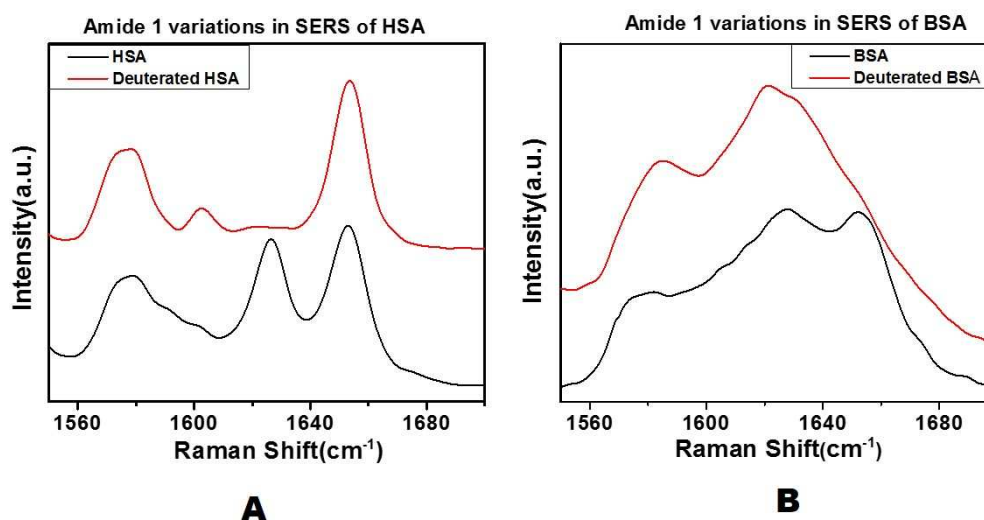


Figure 4.3: A: Effect of Deuteration on Amide 1 band of HSA; B: Effect of Deuteration on Amide 1 band of BSA

Deuteration studies of the serum proteins: Deuteration studies of the proteins were performed to ascertain the amide mode assignment, predominantly Amide I (Fig.4.2). When a labile hydrogen of the peptide is replaced by a heavier deuterium, there is an expected decrease in the Amide band frequency without any changes in the peak position of most other modes as well as its intensity.

However, we see an entirely different behavior in SERS spectra in the case of BSA vis-a-vis HSA. Although the proteins are structurally similar, the deuteration effects on SERS spectra were different (Fig.4.3). In the case of HSA, there is a slight increase in intensity of the 1653 cm^{-1} band corresponding to the α - *helix* domain, while the mode related to antiparallel β - *sheet* at around 1620 cm^{-1} decreases to around 1600 cm^{-1} . This shows that the antiparallel β - *sheet* domain of HSA gets preferentially deuterated in comparison to the α - *helix* domain. In comparison, in the case of BSA, the α - *helical* domain as well the β - *sheet* domain

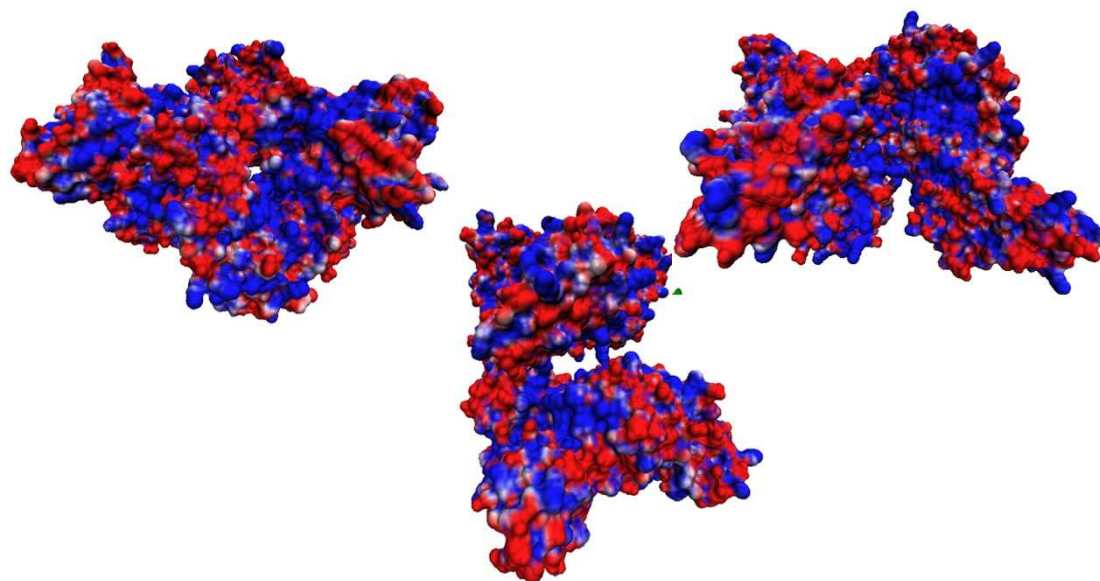


Figure 4.4: Surface Charges on HSA. Red: Negative Charges and Blue: Positive Charges

gets deuterated as both of these modes gets shifted by $8-10\text{ cm}^{-1}$. Other major changes occur in the carboxylate modes including bending and wagging vibrations since they are involved in hydrogen bonding. These modes change in intensities which indicate that there is a subtle change in the way the carboxylate groups of the proteins are oriented with respect to the surface of the silver nanoparticles. Since deuteration causes structural alterations in the protein, it also reflected in the SERS spectrum where there is a change in orientation of the rings of the aromatic amino acids with respect to the nanoparticle surface. Therefore, modes like B_1 and B_{2g} would change on the deuteration as their intensities are sensitive to their orientation with respect to the nanoparticle surface.

Structural similarities between HSA and BSA probed by SERS: HSA and BSA are structurally similar proteins with sequence conservation as high as 76% (Fig.4.7). The sequence similarity in terms of Q-factor and secondary structure

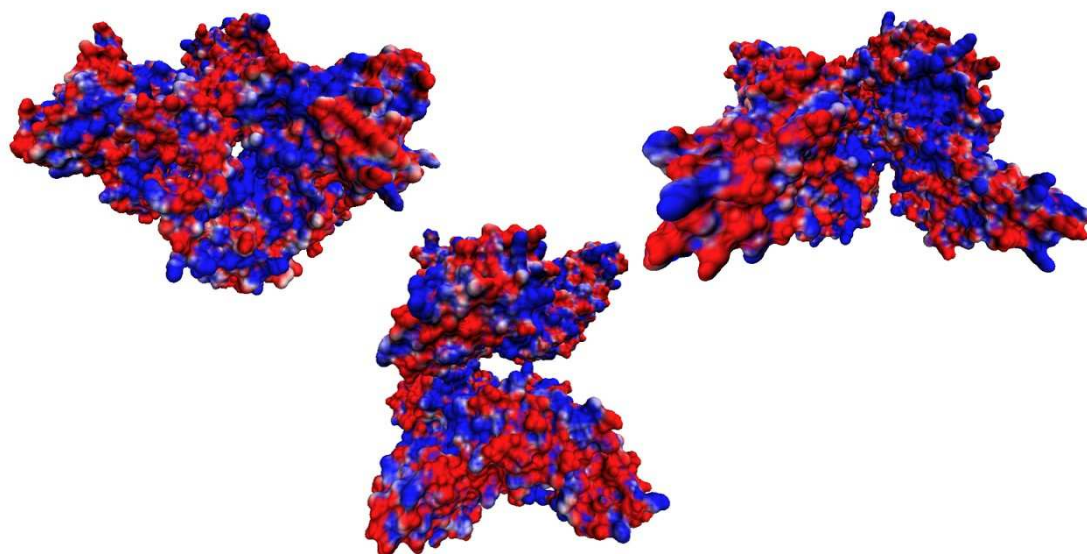


Figure 4.5: Surface Charges on BSA. Red: Negative Charges and Blue: Positive Charges

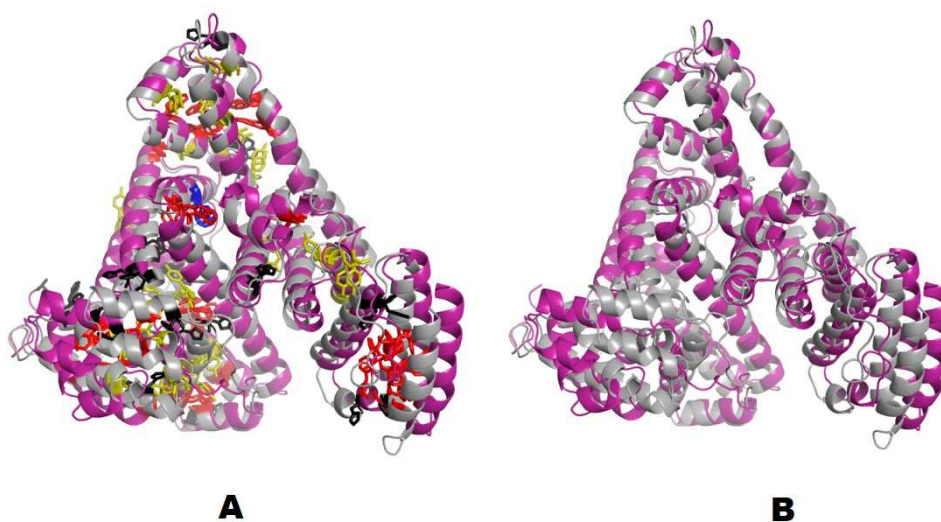


Figure 4.6: A: All aromatic amino acids in HSA and BSA; B: Structural alignment of HSA and BSA

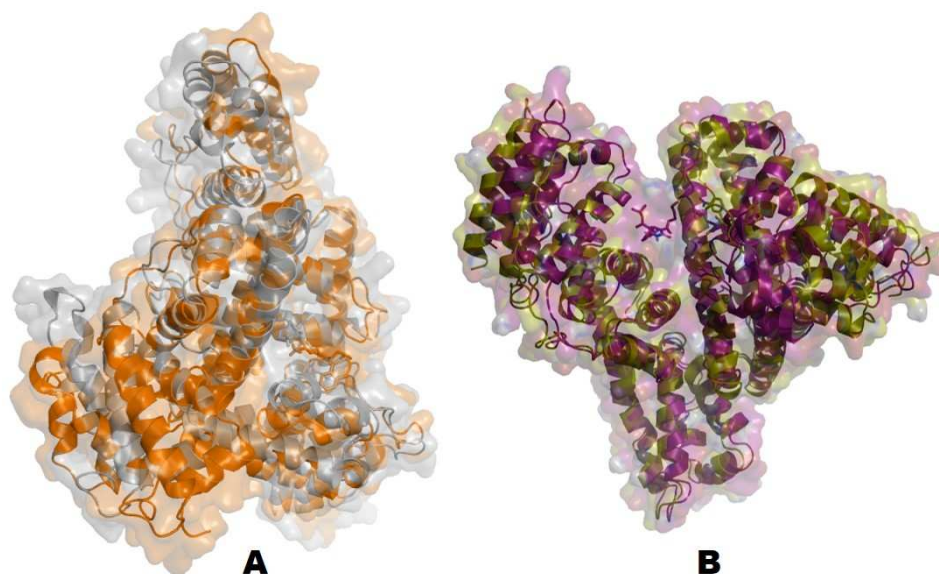


Figure 4.8: A: Amlodipine docked on HSA and BSA; B: Nimodipine docked on HSA and BSA

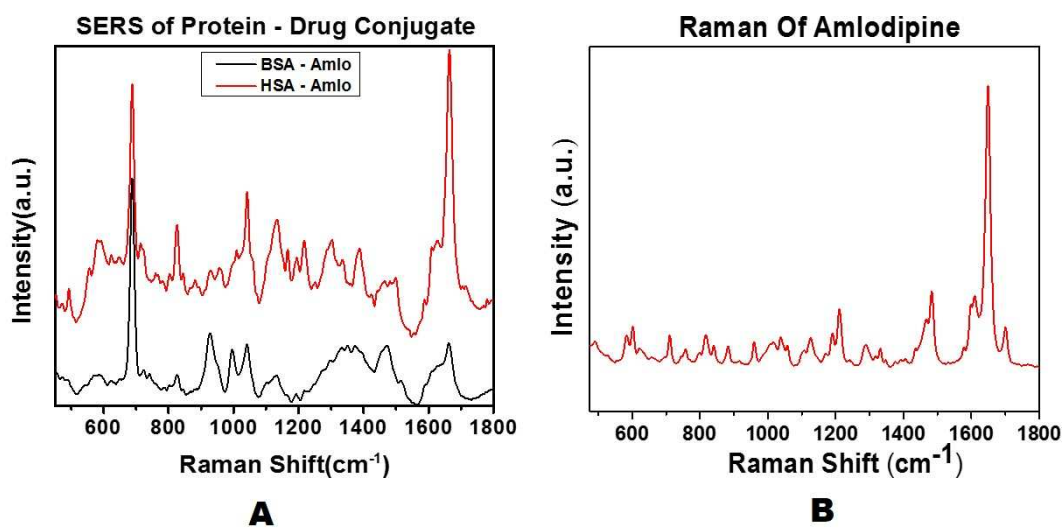


Figure 4.9: A: SERS spectra of HSA-Amlodipine conjugate and BSA-Amlodipine conjugate; B: Raman spectra of Amlodipine

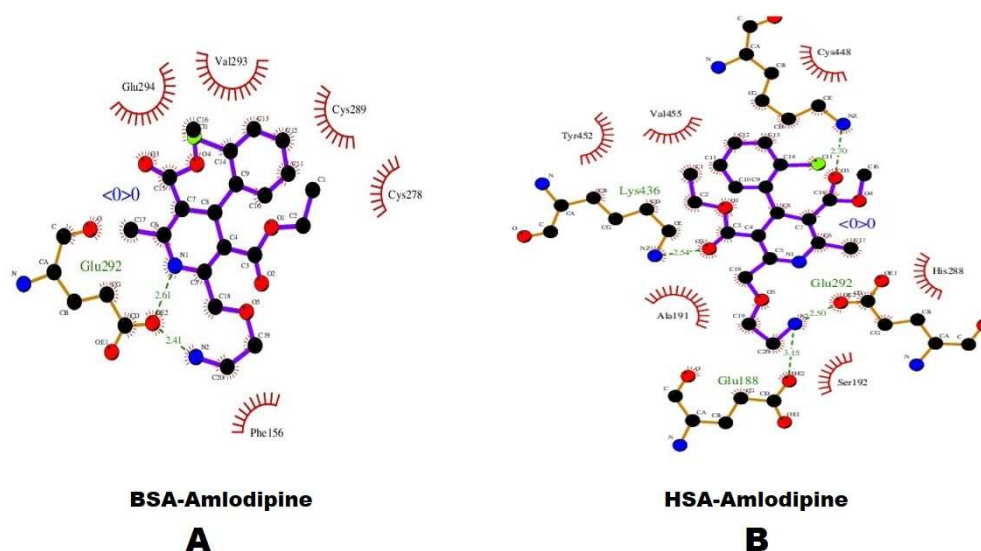


Figure 4.10: Ligplus plots showing Residues adjacent to Amlodipine binding pockets for; A: BSA and B: HSA

Interaction of amlodipine with HSA and BSA: The SERS spectra of protein-amlodipine conjugates are dominated by modes from amlodipine itself convoluted with those of the protein. Fig.4.9A shows the SERS of amlodipine conjugated with BSA and HSA. The Raman spectrum of Amlodipine is shown as a reference (Fig.4.9B). There is a strong overlap in the entire spectral region of the protein with the modes of amlodipine. This makes it difficult to analyze specific changes along individual modes of the protein and interpret it with the structural aspects. But the SERS spectra of HSA and BSA conjugated with amlodipine shown major differences. This gives sufficient confidence to say that the binding of the amlodipine produces different surface charge distributions, as well as hydrophilicities on these proteins leading to the difference in the adsorption on the surface of the nanoparticles. As an example let's look at the amide I band: in the case of HSA this peak is completely obscured by the peaks from amlodipine, whereas, in the case of BSA,

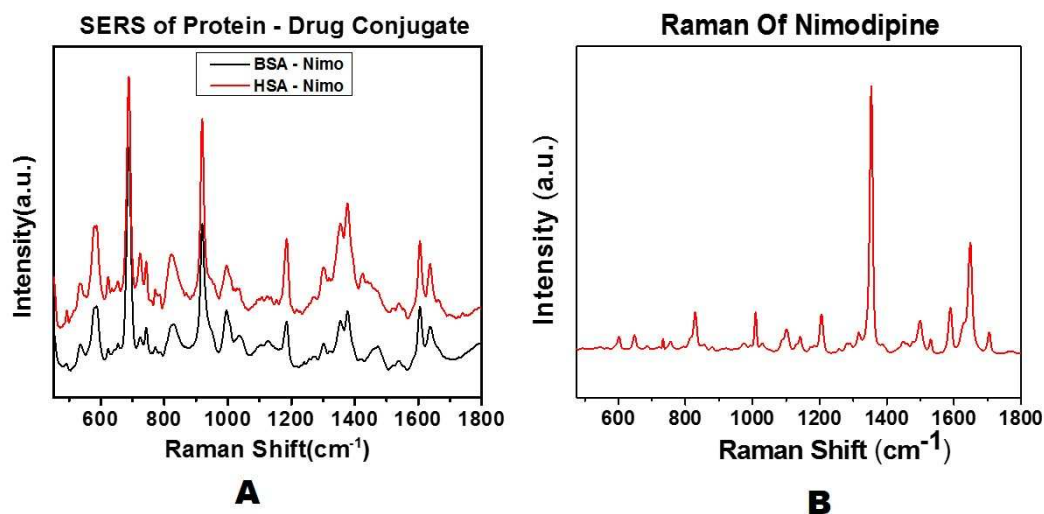


Figure 4.11: A: SERS spectra of HSA-Nimodipine conjugate and BSA-Nimodipine conjugate; B:Raman spectra of Nimodipine

there is a far lesser overlap of the two bands. This supports our assumption that the binding of the drug on the protein leads to the difference in the way they are adsorped on the surface of the nanoparticle in the otherwise structurally similar BSA and HSA proteins. To validate our results we have carried molecular docking studies to demonstrate the possible binding sites of amlodipine (Fig.4.8A). The amlodipine forms a hydrogen bonding with Glu-292 with both BSA and HSA, and the binding pocket is similar. But as seen from the surface representation, in case of HSA, the bound amlodipine lies more towards the solvent accessible surface. Therefore, the enhancement in the modes of amlodipine is more in case of the HSA than BSA.

Interaction of nimodipine with HSA and BSA: The SERS spectra of BSA and HSA conjugated with nimodipine (Fig.4.11A) shows a very different behavior compared to that observed in the case of amlodipine. There is a negligible overlap of

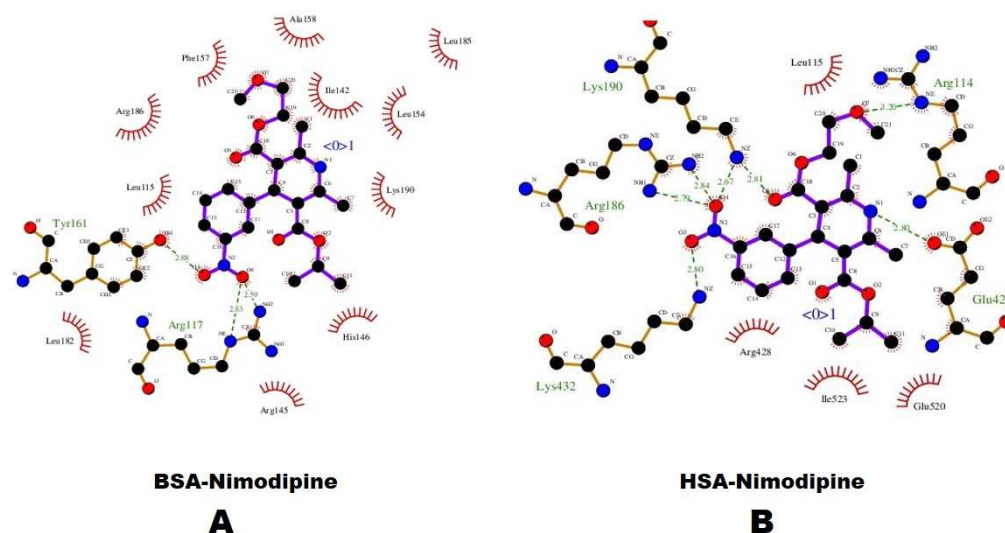


Figure 4.12: Ligplus plots showing Residues adjacent to Nimodipine binding pockets for; A: BSA and B: HSA

modes of the protein with those of nimodipine thus making the spectra easier to interpret. The retention of the amide I bands in case of the protein-nimodipine conjugate in both the cases indicates that nimodipine doesn't bind in the same place as the amlodipine. We observe the bands at around 670 cm^{-1} corresponding to the DMSO solvent used to dissolve nimodipine in the conjugated spectra. The similarity of the two spectra shows that the binding mode of nimodipine to the two proteins is similar, and the ligand binding does not affect charge or hydrophilicity of the protein at the point of interaction with the surface of the nanoparticles. We have shown in the Fig.4.11B, the Raman spectra of Nimodipine for comparison. The binding of nimodipine with the proteins was validated using molecular docking simulations (Fig.4.8B). The molecule binds to the same binding pocket in both HSA and BSA. It is noteworthy that the binding position of nimodipine lies a bit far from the solvent accessible surface used by the amlodipine. Therefore,

it validates our conclusion that the reason for the minimal overlap of molecular signatures of nimodipine in the SERS spectrum of the protein-ligand complexes.

4.4 Conclusions

We used the highly sensitive technique of surface enhanced Raman spectroscopy to study the binding of anti-hypertensive drugs amlodipine and nimodipine to the serum proteins human and bovine serum albumins. We could elucidate the minute differences in binding of these drug molecules through the SERS spectra and could verify the same by using molecular docking studies. This clearly says that even as a quick and dirty way the SERS could provide us a first approximation whether the binding site of the molecules were same or different for molecules derived from the same drug. This type of specific information can pave the way for using the SERS as a molecular screening technique. With greater control over the SERS interpretation, one could develop it into a very good molecular probe for binding studies, but this would require a lot of focused studies before it can see the light of the day. The ease with which SERS can provide information along with molecular dynamic simulations, it has a great potential for being a drug screening tool.

CHAPTER 5

SURFACE ENHANCED RAMAN

SPECTROSCOPY OF RESTRICTION ENZYME

R-KPN1

5.1 Introduction

Restriction endonucleases (REases) are excellent model systems for understanding DNA recognition and phosphodiester bond hydrolysis. The hydrolysis of the phosphodiester bond at specific sequences yield 3-hydroxyl and 5-phosphoryl termini. REases exhibit high sequence specificity in substrate binding and use versatile DNA cleavage mechanisms [80–83]. R.KpnI, also belongs to HNH nucleases family. Many properties of Kpn1, isolated from *Klebsiella pneumoniae*, have been studied, and they have been found to differ from HNH nucleases. For example, Kpn1 is activated by metal ions belonging to both the alkaline earth and transition groups. This feature is not common to the other members of the superfamily [84]. Further, among the metal ions that conduct DNA cleavage, some of them induce promiscuous cleavage (Mg^{2+} , Mn^{2+} , and Co^{2+}) while others (Ca^{2+} , Cd^{2+} , Ni^{2+} , and Zn^{2+}) support high-fidelity cleavage. The promiscuous activity of Kpn1 was attributed to second Mg ion which binds to ExDxD motif. Whereas the suppression of the promiscuous activity along with an induction of high-fidelity cleavage in case

of Ca^{2+} could be attributed to the presence of an additional Ca^{2+} binding site in the enzyme [85]. Ca^{2+} has ionic radius larger than Mg^{2+} , (Ca^{2+} ionic radius = 1.14 Å, Mg^{2+} ionic radius = 0.86 Å). Due to increase in the ionic radius, the enzyme becomes specific even at high concentrations of the enzyme or the metal ion. Kpn1 exhibits promiscuous activity even at low enzyme concentrations for lower ionic radii. Promiscuous activity has been proposed to offer an adaptive fitness to the host bacteria and a gateway to the evolution of new enzyme activities [86]. This suggests that altering the active site interactions with the metal ion could affect the enzymes specificity.

In this chapter, we have used surface-enhanced Raman scattering (SERS) to study the dramatic effect of metal ion cofactor on the KpnI activity. SERS can be used to pick up structural changes induced by metal ion cofactors. Ca^{2+} has a coordination number of 6, and it has two binding sites on Kpn1. For proteins, any change in structure brings about a change in activity of protein and vice versa. So we expect differences in secondary structure of Kpn1 in the two cases, namely, when one Mg ion binds to Kpn1 and the other when Ca ion binds to Kpn1 [87]. The subtle changes at the molecular level in the binding sites brings about changes in the global secondary structure of Kpn1. These effects can be studied with the help of SERS. Other techniques like fluorescence, XRD provide global structural information rather than providing a molecular picture to the desired phenomenon.

5.2 Experimental methods

R.KpnI and its mutants were purified using the method described previously [88]. A buffer containing 20 mM Tris-HCl (pH 7.4), 25 mM NaCl, and 5 mM 2-mercaptoethanol was used for diluting the enzymes. Bovine serum albumin was used as a standard

in Bradford method for estimating the concentration of the proteins. The purity of the proteins was assessed by sodium dodecyl sulfate polyacrylamide gel electrophoresis (PAGE). Oligonucleotides (Microsynth and Sigma) purified on a 15 % urea polyacrylamide gel were labeled at the 5' end using T4 polynucleotide kinase (New England Biolabs) and [γ - ^{32}P] ATP (6000 Ci/mmol, Perkin-Elmer Life Sciences) and purified using G-50 spin column chromatography. The Hi-Trap heparin column (GE Healthcare), ampicillin, chloramphenicol, bovine serum albumin, polyethyleneimine, Coomassie Brilliant Blue, IPTG (Sigma), and phosphocellulose P11 (Whatman) were used. Megaprimer inverse polymerase chain reaction (PCR) method was used to generate Site-directed mutants of R.KpnI. Glycerol is required for structural stability of proteins. But for SERS studies glycerol was removed by repetitive dialysis as it gives strong signals and masks the protein spectra. Small molecules like beta-mercaptoethanol were also removed from the protein solution after purification.

Citrate capped silver nanoparticles were prepared by Lee-Meisel method. Initially, 18 mg of silver nitrate was dissolved in 100 ml of water and brought to boiling point. 2 ml of 1 % aqueous sodium citrate was added to it and stirred vigorously. After 1 hour, the heat was turned off, and the solution was brought to room temperature while stirring. The colloid was characterized by transmission electron microscopy (TEM)(JEOL JEM 3010) and UV-vis absorbance spectroscopy (for further details see the Chapter 2).

SERS spectra were obtained by using a custom made Raman setup in an 180° backscattering geometry. A 532 nm Nd-YAG solid state laser was used as an excitation source. A custom built Raman spectrometer equipped with an SPEX TRIAX 550 monochromator and a liquid nitrogen cooled CCD were used to record the spectra. A 3 cm^{-1} resolution was achieved by using a holographic 1800 grooves

mm^{-1} along with a 200 μm spectrograph entrance slit settings. For SERS measurements of the aqueous protein solution, a 50X air objective lens was used. The laser power achieved at the sample was typically 5 mW. The accumulation time for each spectrum was typically 120s.

5.3 Results and Discussions

Attachment of Silver with Protein (Kpn1):

Silver nanoparticles of spherical shape having diameter in the range 30-50 nm were used for surface-enhanced Raman scattering studies. These nanoparticles were capped with citrate to prevent them from agglomerating. Citrate capped nanoparticles does not have any observable SERS modes, and hence they dont show any spectra of their own. Hence, the protein spectra are not interfered by any signals from nanoparticles. Since, the citrate is a weak capping agent, it can be easily displaced by the protein to get adsorbed on the nanoparticles. This attachment of protein with silver nanoparticle is electrostatic in nature. Silver nanoparticles are negatively charged whereas Kpn1 has an overall positive surface charge.

The electrostatic attachment sites on the surface of protein with respect to the nanoparticles is dependent on the surface hydrophilicity, the surface charges and the nanoparticle size. The Fig.5.1 shows the hydrophobic and the hydrophilic region on the surface on the Kpn1 dimer in the active site region and Fig.5.2 shows the surface charges on the Kpn1. The sites which are both hydrophilic and positively charged are more favorable for the nanoparticle attachment. Crystal structure of the Kpn1 is still unknown, so from the homology modelling, the molecular structure for residues 97 to 190 is depicted in Fig.5.3. All the major aromatic amino acids

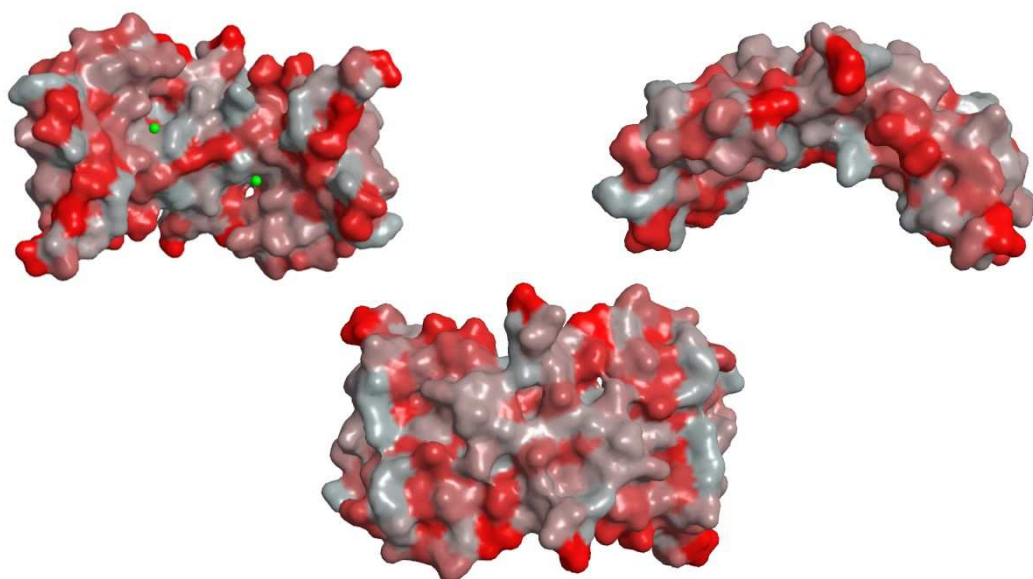


Figure 5.1: Hydrophobic(Red) and hydrophilic(Grey) region on the surface of kpn1

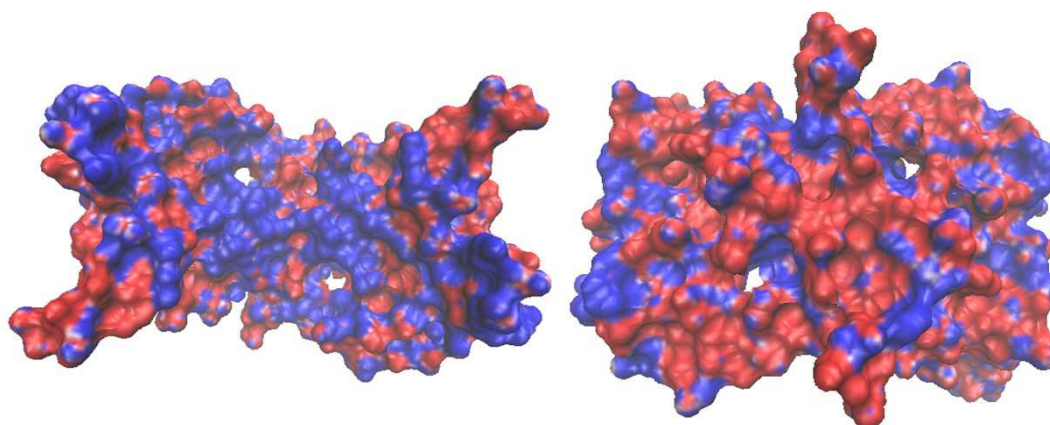


Figure 5.2: Surface Charges on Kpn1. Red: Negative Charges and Blue: Positive Charges

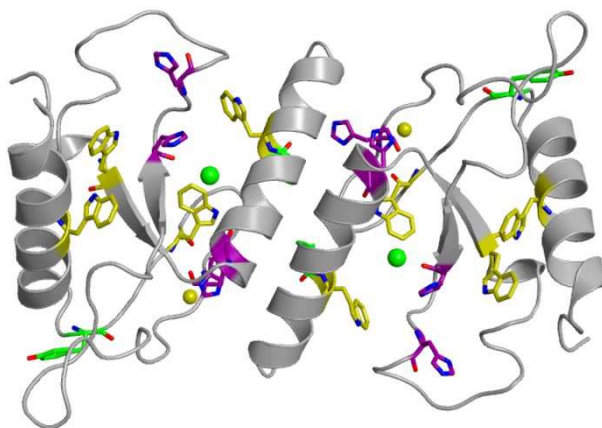


Figure 5.3: Molecular Structure of Kpn1 for residues 97 - 190. All aromatic amino acids have been shown. Histidine: Purple, Tryptophan: Yellow and Tyrosine: Green

present in this domain are shown in the structure. Surprisingly, no Phenylalanine was present in this domain. In SERS, we have a major contribution from the aromatic amino acids, and they play a vital role in structural analysis using SERS. Fig.5.4 shows the probable attachment site and orientation of the Kpn1 on the silver nanoparticles.

The size of nanoparticle is another major factor, as it determines the total surface area available to the protein for the attachment and the distribution in size of the nanoparticles (30 - 50 nm), generates the surface plasmons in the visible range. Effect of salt addition on colloidal silver nanoparticles was also studied using UV-Visible spectroscopy. Addition of both calcium and magnesium salts led to agglomeration of the silver nanoparticles. Colloidal Ag nanoparticles had an absorbance maxima at 438 nm, which decreased to 397 nm and 408 nm after adding calcium and magnesium salts respectively (Fig.5.5). The surface plasmon

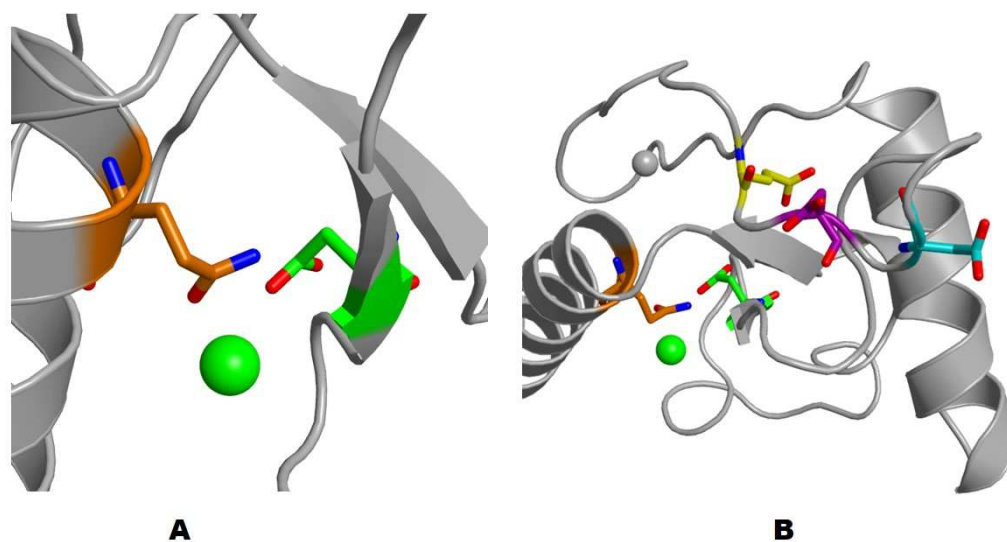


Figure 5.4: Cationic binding pockets. A: Mg binds at D148 and Q175. B: Ca binds at D148, D163, Q175, E132, D134 and D136

peak broadened, and the new plasmon peak at a higher wavelength was observed confirming the aggregation of colloidal Ag nanoparticles.

Activity of Protein Nanoparticle Conjugates:

Biochemical assays were performed to study the activity of protein in the presence of nanoparticles. DNA binding and cleaving activity of both the Kpn1 and the Kpn1 adsorbed on silver nanoparticle were compared. From the results, it was evident that protein did not lose its activity in the presence of nanoparticles, and it was only found to be moderately reduced (Fig.5.7).

Colloidal nanoparticles are slightly basic in nature (pH around 8); this leads to a slight structural deformation of protein which causes a reduction in enzymatic activity. But since the enzymatic activity was retained even after adsorption on nanoparticles, so in this case there were not much of structural deformation, and it is suitable to study the structural property of the protein using SERS. This was

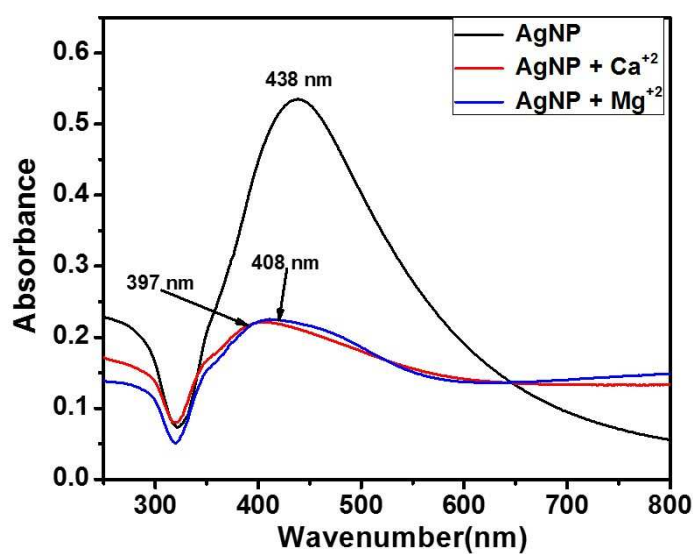


Figure 5.5: UV-Vis spectra: Effect of Salt Addition on Ag nanoparticles

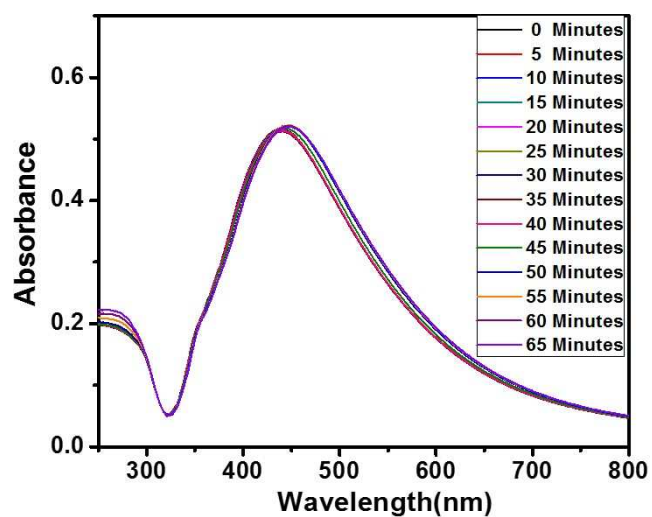


Figure 5.6: UV-Vis spectra: Time-dependent activity of Kpn1 in presence of Ag nanoparticles.

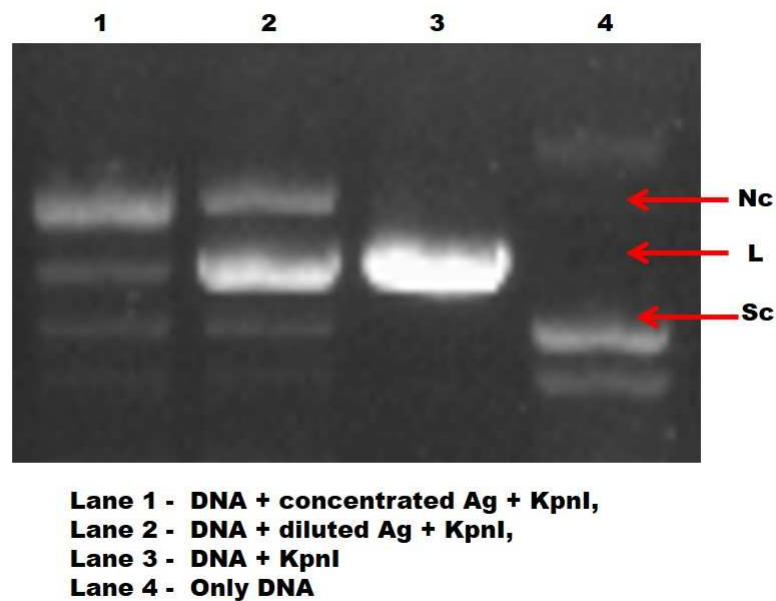


Figure 5.7: DNA cleavage properties of R.KpnI. KpnI was incubated with and without nano particles (1:1 ratio) on ice for 5 min. Plasmid DNA (pUC18 DNA) was added to the mixture in the presence of 2 mM Mg^{2+} at 37°C for 1 h . The cleavage products were analyzed on a 1% agarose gel. N_c , L, and S_c indicate the positions of nicked circular (N_c), linear (L), and supercoiled (S_c) forms of the plasmid, respectively

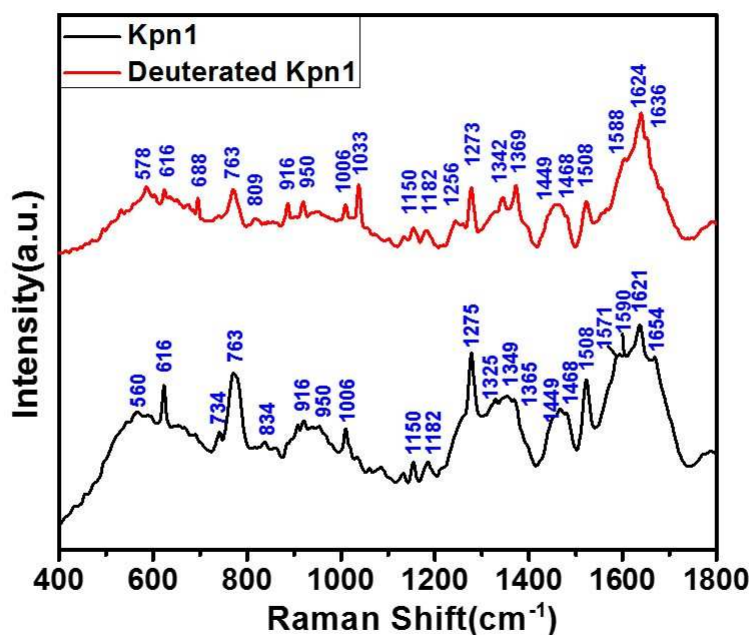


Figure 5.8: SERS spectrum Kpn1 and Deuterated Kpn1

also proved by doing UV-Visible spectroscopy of protein nanoparticle conjugate. Absorbance maxima of the conjugate did not change with time. The spectra were recorded every 5 minutes for a total time of 60 minutes. There was no change in the absorbance maxima. The loss of enzymatic activity in the presence of colloidal silver nanoparticles would have led to agglomeration of nanoparticles causing a decrease in intensity, as well as wavenumber of the absorbance maxima with time.

SERS of Kpn1:

As described earlier, the Kpn1 is a 50 kDa protein. In a normal Raman experiment, there will be contributions from all the amino acids. But in SERS we see only select a few modes being enhanced. SERS can be used to probe protein conformations and spatial structures as it gives surface sensitive information about proteins [89]. The enhancement of a particular vibrational mode of amino acid, in

a SERS experiment, is dependent upon its proximity to nanoparticle as well as its vibrational orientation with respect to the surface[90]. Surface selection rules in the case of SERS are very different than conventional Raman [91]. The modes which have vibrations parallel to the surface are not enhanced in comparison to the modes having vibrations perpendicular to the surface of the nanoparticle. In addition π electron rich systems have a stronger presence in SERS spectrum. This is one advantage of the SERS since a very subtle variations at the molecular level due to the changes in orientation of moieties with respect to the nanoparticle, which is due to the conformational changes in proteins can be detected very easily. The amino acids residues present in the close vicinity of nanoparticles, i.e., on the surface of proteins, give strong SERS spectra, as the enhancement is a distance-dependent phenomenon. If r is the distance between the molecule and the nanoparticle, then the enhancement factor decays as $1/r^{12}$ [92]. The Table 1 gives the band assignment of SERS spectra of Kpn1 and was done in accordance with the available literature for the SERS of the amino acids and the proteins [75–77].

Aromatic amino acids:

All aromatic amino acids show strong SERS modes. The SERS spectra of Kpn1 was dominated by peaks from aromatic amino acids like tryptophan, tyrosine and histidine. Each monomer of Kpn1 has three phenylalanine residues, but they are present at C and N terminals. So the modes corresponding to phenylalanine will be mostly suppressed by other modes of Kpn1. Tyrosine shows doublet in the Raman spectra due to Fermi resonance at around 828 and 845 cm^{-1} . This shifts to 829 and 847 cm^{-1} in the SERS spectra. This doublet arises due to Fermi resonance between the ring breathing mode and the overtone of an out of plane ring bending vibration of the para-substituted benzene ring in the tyrosine. For Kpn1, the mode at 834 cm^{-1} can be assigned to the lower mode of the tyrosine Fermi doublet. Higher

Table 5.1: Tentative Band Assignments of SERS for Kpn1

Kpn1 (cm^{-1})	Deuterated Kpn1 (cm^{-1})	Tentative Band assignment
560	578	Trp
616	616	COO^- wagging
734		Trp/ $\delta(COO^-)$
763	763	Trp(H19) or His
834		Tyr and/or $\nu_{as}(C - S - C)$
916	916	$\nu(COO^-)$ / C-C stretch of Pro Ring
1006	1006	Indole asymmetric ring breath
	1033	C-N stretch
1150	1150	NH^{3+} deformation
1182	1184	Tyr and/or Phe(ν_{9a})
	1256	Amide III
1275	1273	Amide III / $C - C\alpha - H$ deformation
1325		CH_2 wagging/ $\delta(C - H)$
1349	1342	$C\alpha - H$ bend/ $C - C\alpha$ stretch
1365	1369	COO^- symmetric stretch
1449	1449	(CH_2) / $\delta(C - H)$
1468	1468	CH_2 scissoring
1508	1508	Amide II
1540	1540	Trp w3
1590	1588	Asp , Glu C=O stretch, Trp, His
1601	1602	Phe
1621	1624	Amide I
1654	1636	Amide I

frequency mode of the doublet was not observed. This low-frequency mode is a B_{1g} mode of the tyrosine. It gets enhanced only when the face of the ring is tilted to the metal surface. Its intensity changes with changes in orientation of ring with respect to the metal surface. These modes also depend upon the conformation of the amino acid backbone. Tryptophan modes were observed at 560, 763 and 1325 cm^{-1} . The mode at 763 cm^{-1} can be assigned to the histidine present in the protein.

Aliphatic side chain vibrations:

Glutamic acid and aspartate are the two amino acids having aliphatic side chains. The mode at 916 cm^{-1} can be assigned to the stretching vibration of C-COO^- . But the asymmetric stretching mode $\nu_{as}(\text{COO}^-)$ from glutamic acid and aspartate has an overlap with modes from aromatic amino acids. This mode was observed at 1590 cm^{-1} . The CH_2 deformation vibrations shows distinct doublet at 1449 and 1468 cm^{-1} for the Kpn1. There might be some overlap from histidine and tryptophan in the 1468 cm^{-1} mode. Modes from CH_2 wagging were also observed at 1325 cm^{-1} . C-N stretching mode was observed at 1033 cm^{-1} . There is a possibility of a weak contribution from phenylalanine to this mode. The bands from $\nu(\text{C}\alpha - \text{N})$ and $\nu_{as}(\text{C}\alpha\text{CN})$ are generally observed around 1065–1100 cm^{-1} and 1125 cm^{-1} . But they were not so strong in the SERS of Kpn1. $\nu_{as}(\text{C}\alpha\text{CN})$ bending and $\text{C} - \text{C}\alpha$ stretching bands were observed at 1349 cm^{-1} .

Amide vibrations:

SERS of proteins have modes corresponding to Amide I, Amide II and Amide III. Even though the Amide II is not observed in Raman spectra as it is Raman inactive, but due to modification in the surface selection rules in the SERS, it becomes active and is observed in most of the protein spectra. In earlier Chapter, we have described these modes vibrations in detail (Chapter 4). Amide I band

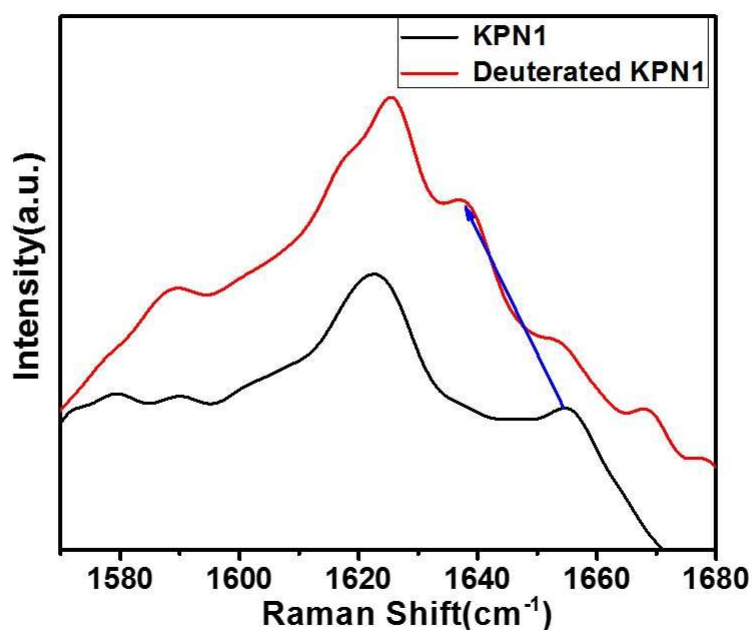


Figure 5.9: Effect of Deuteration on Amide I band of Kpn1

can contain information about the secondary structural elements, since it is one of the strongest peak in the SERS spectra among the Amide modes. Nanoparticles have tendency to bind preferentially to certain secondary structures like α – *Helix*, β – *Sheets* and random coils due to the overall, charge and hydrophobicity. Each secondary structure has a particular frequency of the Amide I band in the SERS spectra. Amide I band also helps in determining the mode of attachment of protein with the nanoparticle. It is sharp in SERS in comparison to the normal Raman spectra, where it is much broader. The presence of all amide bands due to various secondary structural elements can be confirmed by deconvolution of peaks in this region. In SERS of Kpn1 Amide I band was observed at 1621 and 1654 cm^{-1} . The mode at 1621 cm^{-1} is due to the antiparallel β – *sheets* whereas the mode at 1654 cm^{-1} is due to α – *helix*. There could be some contribution from the

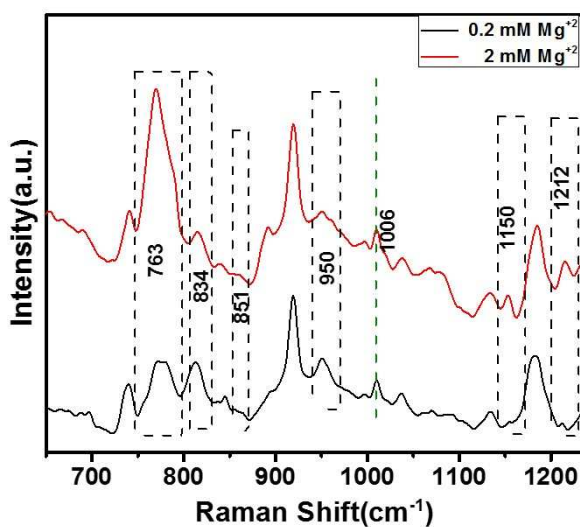


Figure 5.10: A: SERS spectra of Kpn1 on addition of Magnesium

asymmetric C=O stretch of glutamic acid in the band at 1621 cm^{-1} . From the modeled structure, it is evident that Kpn1 contains both antiparallel β – sheet as well as α – Helix. The amide I band was generally confirmed by deuteration studies. After deuteration, the band at 1654 cm^{-1} shifts to 1636 cm^{-1} [93]. This decrease in frequency is due to increase in mass. Amide III band is observed in the region $1200\text{--}1400\text{ cm}^{-1}$ and has contributions from other bands as well. For Kpn1, it was observed at 1275 cm^{-1} and after deuteration, it shifted to 1256 cm^{-1} . There was a decrease in intensity of the band at 1275 cm^{-1} and a new band was observed at 1256 cm^{-1} after deuteration. The Amide II band lies around $1510\text{--}1530\text{ cm}^{-1}$ in the SERS spectra of proteins, so the band at 1508 cm^{-1} is assigned to the Amide II mode. The intensity of this band decreases upon deuteration. Due to the presence of other peaks around the Amide II, it was difficult to ascertain the shifted peak due to the deuteration.

Effect of Metal Ions on Kpn1:

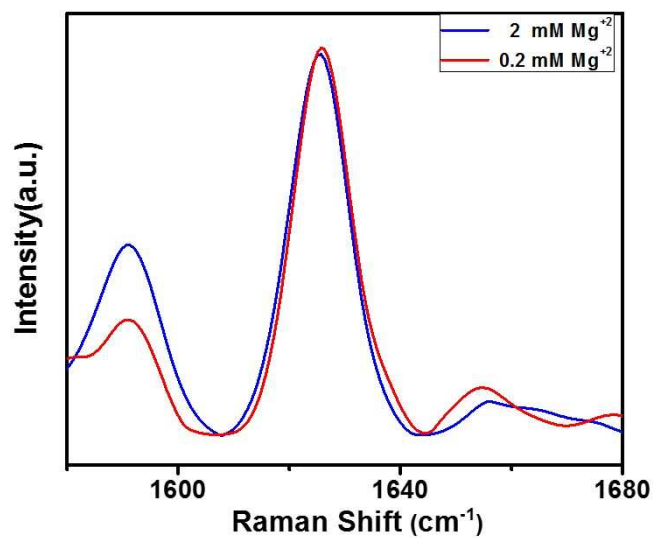


Figure 5.11: A: Effect Of Addition of Magnesium on Amide I of Kpn1

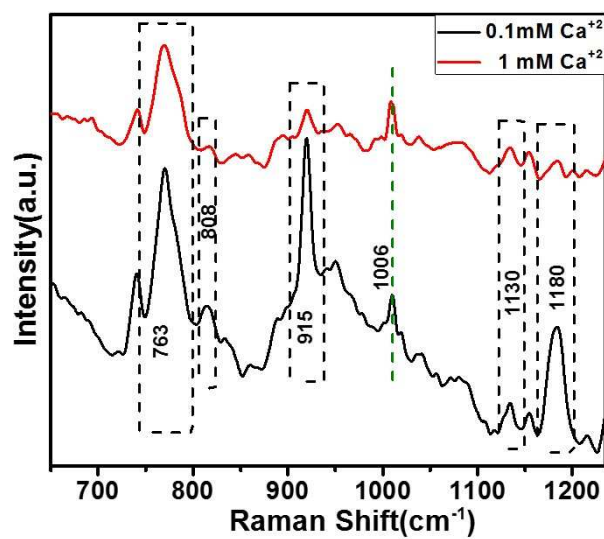


Figure 5.12: A: SERS spectra of Kpn1 on addition of Calcium

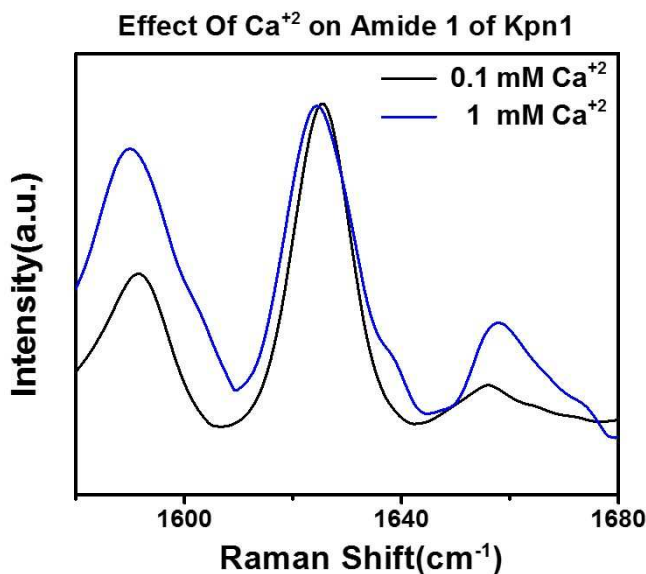


Figure 5.13: A: Effect Of Addition of Calcium on Amide I of Kpn1

It has been seen earlier that Mg^{2+} binds in HNH active site of Kpn1, at lower concentrations (0.2 mM), one magnesium atom binds per monomer of Kpn1. At higher concentrations (2 mM), two magnesium atoms binds per monomer of Kpn1. The magnesium ions binds at both HNH active site as well as $E_{132}_xD_{134}_xD_{136}$ motifs. While in case of Ca^{2+} irrespective of the concentration (0.1 mM or 1 mM), it binds at both HNH and E_xD_xD motifs. Residues D148, D163 and Q175 constitute HNH motifs whereas residues E132; D134 and D136 constitute ExDxD motifs. These motifs are present on two different domains on the Kpn1. SERS spectra of Kpn1 on addition of Mg^{2+} should show changes in intensity of peaks corresponding to aromatic amino acids ($700 - 1200\text{ cm}^{-1}$) if it induces re-orientation with respect to the nanoparticle surface due to certain conformational changes. We do not observe any change in peak position for any of the aromatic amino acids at both low and high concentration of magnesium (Fig.5.10). This was confirmed by normalizing and plotting Amide 1 region for low, and high concentration of Mg

Fig.5.11. There was no shift in the peak position of Amide I band as well. The band at 1006 cm^{-1} was assigned to symmetric ring breathing mode of indole in the SERS spectra of Kpn1 [79]. This mode is independent of orientation of ring on the metal surface. So, it was normalized in both the spectra (low and high conc. Of Mg), for comparing the changes in intensity. The modes at 763, 834, 851, 950, 1150 and 1212 cm^{-1} showed changes in intensity with addition of Mg^{2+} to Kpn1. The change in the intensity of these modes shows change in the orientation of benzene rings of aromatic amino acids on the metal nanoparticle surface, suggesting secondary structural changes [78]. On addition of Ca^{2+} to Kpn1, we observe similar changes as shown in Fig.5.12 There was no shift in the peak positions of any of the bands or appearance/disappearance of any band. Like the case of Mg, there were no changes in Amide I as well, as shown in Fig.5.13, upon addition of Ca. But Ca has a coordination number of 6, and it binds at to both the HNH and E_xD_xD motifs, which are away from each other. From the modelled structure of the active site region, (Fig.5.3) it can be seen that Kpn1 has random coil. On the addition of Ca, Kpn1 folds along this random coil so as to bring both the motifs closer to surround Ca. This makes binding of Ca easier. Ca has bigger ionic radii as compared to Mg. At present, the preliminary studies do not give clear indication of the conversion of random coils to higher secondary structures. Further experiments are in progress to study this through mutation of the calcium and magnesium binding sites.

5.4 Conclusions

Surface enhanced Raman spectroscopy to study the secondary structure of Restriction enzyme Kpn1. Kpn1 is a small protein, so it is fully in the vicinity of silver nanoparticles. This results in enhancements of most of the vibrational

modes of Kpn1. Addition of cations like magnesium and calcium to Kpn1 leads to its structural changes. SERS is a surface sensitive technique which can detect minute structural variations at the molecular level which are capable of bringing global changes in the structure of proteins. It was observed that modes due to aromatic amino acids undergo intensity changes on addition of Mg^{2+} and Ca^{2+} to Kpn1. There was no shift in the position of peaks. So it can be concluded that the orientation of the aromatic rings of amino acids changed on addition of metal cations. It has been showing using biological experiments that the effect of the addition of Mg^{2+} is different to that of Ca^{2+} . Similar results were obtained from SERS spectra. The vibrational modes undergoing intensity changes need to be further analysed. Molecular Dynamics simulations will have to be done for confirming the orientation of Kpn1 on silver nanoparticles. This will provide better insight to the orientation of aromatic rings in the binding pockets of Kpn1, on the surface of metal nanoparticle.

CHAPTER 6

PLASMONIC FEATURES OF LOW TEMPERATURE MELTING ALLOYS IN ORGANIC SOLAR CELLS

6.1 Introduction

Solar energy has become one of the most promising renewable resources to meet the increasing energy demands. Organic solar cells are easy to fabricate, lightweight and low-cost alternative to traditional silicon (Si) for harnessing solar power. Organic solar cells are intensely being studied as a potential photovoltaic PV device due to the solution processing methods and the relative ease of fabrication. The combination of unique semiconducting electronic property and mechanical aspects similar to conventional plastics is an attractive feature in spite of the lower efficiencies prevailing in these systems. Power conversion efficiency for organic solar cells has reached well above 9% in lab [94],[95], but the module efficiencies remain quite low [96]. Low efficiency of modules has been related to effects like increase resistive losses , a lesser contribution from the region around the electrode [97] and reduced collection efficiency [98], [99]. It has been demonstrated that the performance parameters vary inversely with scaling up of electrode area [97], [100]. The essential active ingredients for the polymer solar cells (PSC) are widely used

donor and acceptor kind of polymers intermixed to form bulk heterojunction (BHJ) facilitating charge transfer and transport processes. In BHJ solar cells, active layer bulk-morphology plays an important role in transport processes and is controlled by the factors such as solvent properties, drying and annealing conditions,[95] and appropriate distribution of the two components. A crucial factor to realize the maximum impact of the different strategies finally depends on better fill factor FF of the devices which is more sensitive to the polymer-metal interface morphology unlike other parameters such as the open-circuit voltage V_{OC} and short circuit current density J_{SC} . By using low-temperature meltable alloy and pixelating the cathode, it was demonstrated by Das et al.[101] that efficiencies can be retained over larger module area. Their strategy avoids the efficiency loss occurring in large area devices due to electrically resistive losses and lesser contribution from the vicinity of the electrode. Retention of single pixel efficiency over a module dimensions is achieved by reducing the area of single contact.

Recently, plasmonic nanostructures like silver and gold nanoparticle [102],[103],[104] have been used for trapping light to increase efficiency of organic solar cells. This additional photon energy is coupled back into the active matrix for increasing absorption in solar cells. Features like shape and size of metal nanostructures can be controlled for tuning surface plasmon properties. This can increase the electromagnetic (EM) field enhancement of the plasmonic nanostructure. Plasmonic properties of metallic nanostructures like silver and gold nano particles, nanorods, nano prisms have been used to increase the optical density and photogeneration of carriers in BHJ solar cells [105]-[106]. While the small area pixelated electrodes over module length can minimize the loss mechanism underlying the large area electrodes, the presence of plasmonic system can further enhance the overall efficiency.

Low-temperature meltable alloys which have been reported earlier [101] have been explored further by studying properties like surface plasmons and micro and nano texturing. Additional advantages like low-temperature processability, easy to pattern, surface texturing at nano and micron scale and surface plasmons over conventional vacuum evaporated electrode can help in retaining the efficiency over large area. The constituent metals show moderate plasmonic activity which can be further enhanced in the presence of surface nanostructures at the BHJ-alloy interface. Light trapping strategies can be benefited by utilizing regular patterns of submicron to micron scale to create local field enhancements. Enhancements greater than 10% have been achieved by using regular periodic structures like optical grating. In general, such patterning requires a very controlled manipulation of metal films or nanostructures to achieve the desired effects. To benefit from the regular pattern mediated light harvesting, there is a considerable need for low-cost structuring. In this regard, we propose micropatterning in the low-temperature alloy as an alternative low-cost patterning technique. The cooling process gives rise to a conformal patterning at the alloy/BHJ interface guided by the surface instabilities. These patterns are regularly distributed with the inter structure distance ranging from 15-30 microns.

Metal nanoparticle-based on silver and gold have been widely utilized as host for plasmonic enhancement in organic solar cells. These systems are introduced as an additional element in buffer layers or otherwise as an additional layer in and around the BHJ. Here we demonstrate the plasmonic activity in alloy electrodes which also serves as the low-temperature alternative for vacuum free back electrode. The presence of alloy interface shows a significant increase in Raman mode for P3HT as compared to aluminum (Al) interface. The alloys demonstrated in previous work constituted lead (Pb) as one of the components. A Pb-free system is always

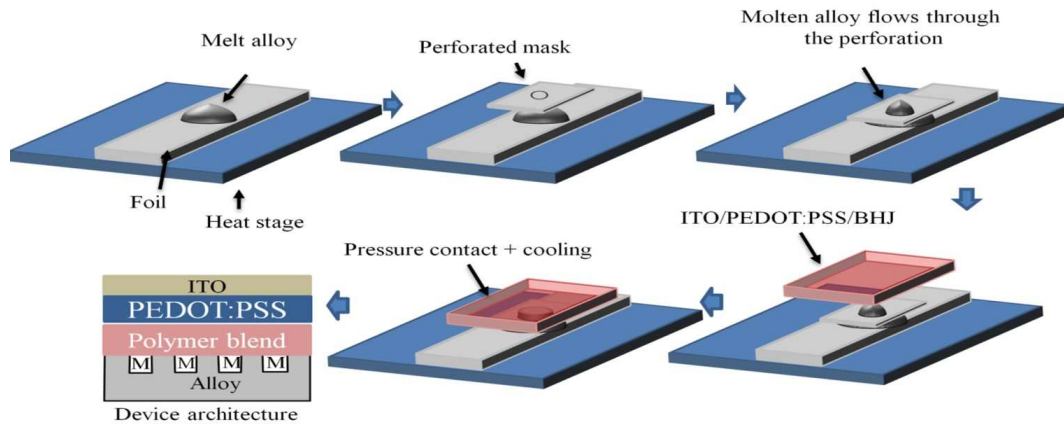


Figure 6.1: Schematic for alloy electrode fabrication over P3HT:PCBM60 BHJ film via vacuum free melt phase processing

desirable for viable widespread use of these meltable electrodes. We present a Pb-free alternative electrode which demonstrates comparable plasmonic features. Short circuit current densities measured for model BHJ system are comparable for both sets of alloy electrode systems. While the open circuit voltage and fill factor remains low and, further improvements are required.

6.2 Experimental Methods

Device Fabrication

P3HT was procured from luminescence Technology Corp. (lumtec), Taiwan and PC60BM were purchased from nano-c. P3HT-PC60BM was blended in 1:1 (wt/wt) ratio in *o*-dichlorobenzene (*o*-DCB). ITO-coated glass substrates were cleaned by Sonication in IPA and acetone followed by RCA treatment. For Raman measurements a thin layer $\sim 25 - 30$ nm was coated from very dilute solution on ITO-coated glass substrates. For solar cell fabrication, a thin layer (30 - 40 nm)

of *PEDOT : PSS* (Clevios 1000) was spin coated at 4000 RPM and annealed at 150 °C for 20 min. The PEDOT coated substrates were transferred to nitrogen-filled glove box ($O_2 \sim 3$ ppm, $H_2O \sim 2$ ppm), *P3HT – PC60BM* active layer of film thickness ~ 100 nm was coated from 16 mg/ml solution in o-DCB at 1000 rpm. All films were annealed at 120°C for 15 min inside a glove box. Aluminum back electrodes were evaporated at the rate of 5 Å/s inside a thermal evaporator at 10^{-6} mbar pressure. Alloy electrodes were coated in ambient on a hot plate. Alloys were heated above melting point on a hot plate; molten alloy surface was cleaned by scooping the oxidized top surface (a thin oxide layer few nanometer thick is always present which cannot be removed). A mask made of PET sheet was placed on the molten alloy to define the area of the back electrode. The substrates (glass/ITO/PEDOT: PSS/BHJ) substrates were slowly lowered, BHJ facing downward, using a precision z stage and brought in contact with molten alloy. After the electrode is formed, the system is allowed to cool to room temperature before removing from hotplate; this technique provides reproducible alloy electrodes.

Raman spectra calibration

Raman shifts in wavenumber (cm^{-1}) were calibrated using paracetamol as the calibration reference. Since all the spectra were acquired in real time from 1300-1600 cm^{-1} , Paracetamol spectra were also acquired in real time in the same region. Fig.6.2 shows Raman shift measured for paracetamol on our Raman system, this was compared with the literature value available from RRUFF database. Peak positions were calculated from the Gaussian fit for each major peak (1325.4 cm^{-1} , 1371.3 cm^{-1} , 1562.3 cm^{-1}). Other peaks were not considered because of the variation in spectral feature between measured and the literature value. An average shift of 15.5 cm^{-1} towards higher wavenumber was observed in measured Raman

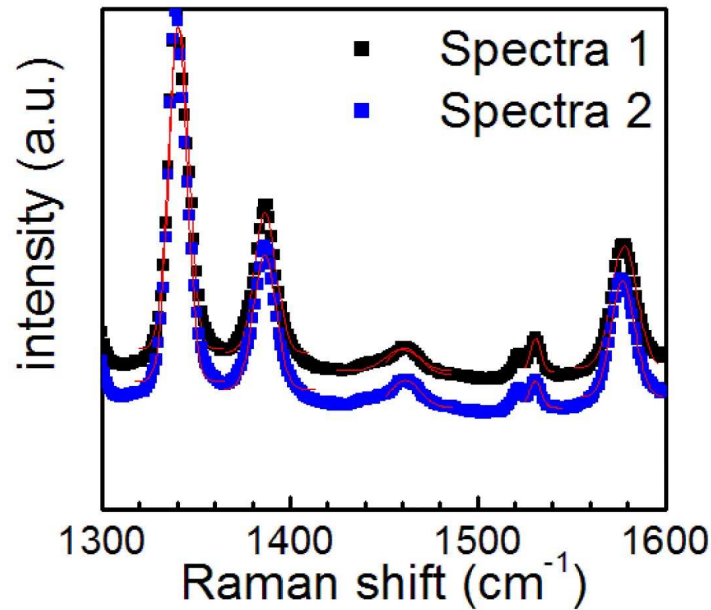


Figure 6.2: Raman Spectral Calibration: Measured Raman shift for paracetamol peaks. This number was used for correcting the Raman shift of alloy 1 and alloy 2.

Scale calibration for optical image

Optical Image was calibrated using AFM calibration grid from Nanonics Imaging. The grid consists of periodic patterns of $10\ \mu\text{m} \times 10\ \mu\text{m}$, visible as black squares [Fig6.3]. An objective with 50X magnification was used for both the images. Laser spot has been shown for comparison purpose. The concentric circles have been included as a guide to eye for comparing the structures against the scale.

6.3 Results and Discussions

Charge extraction properties of low temperature melting alloys were studied with the help of binary mixture of Poly(3 - hexyl thiophene) (*P3HT*) and Phenyl-C61-butyric acid methyl ester (*PC60BM*), as the model system. *P3HT* :

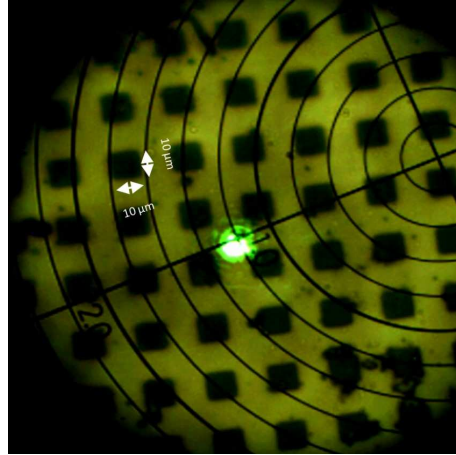


Figure 6.3: Optical image for AFM calibration grid with $10\ \mu\text{m} \times 10\ \mu\text{m}$ periodic structures

PC60BM shows plasmonic behavior in the range 300 nm - 450 nm. It has lower *PCE* than *PBDTTT - CT : PC70BM*. Microstructures formed during the alloy melting stage were thermally stable. General schematic for fabricating alloy electrode is shown in [Fig.6.1]. Two alloys systems, *ROTO136F* (Elec1) and *ROTO281F* (Elec2) were used for this study. *ROTO136F* melts at 56 °C and it is a eutectic mixture of four basic metals Indium (In), Lead (Pb), Bismuth (Bi) and Tin (Sn). It has been reported that 6% efficient cells can be achieved using *ROTO136F* (Elec1) alloy on *PBDTTT - CT : PC70BM* systems. *ROTO281F* is a Pb-free alloy. It melts at 135 °C and is composed of two basic metals Bi and Sn. *ROTO281F* can be a viable In and Pb-free alternative for low temperature back electrode. There was homogeneous distribution of work function, and plasmonic component of the alloy throughout the active area as the individual metals in the alloy do not phase separate after cooling. No additional component were required for connecting different cells in series as the alloy layers themselves served as interconnect between two pixels of the active area. The melting temperature and the cooling rate appear to be critical factors in deciding the interface microstructure.

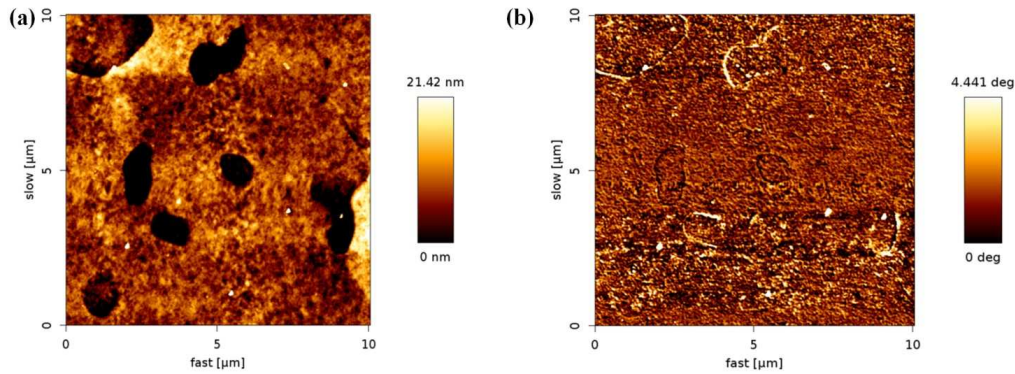


Figure 6.4: a) Surface topography map for ROTO136F, b) Surface phase variation for ROTO136F

Thin film samples of the alloy structures were peeled off from the ITO-glass substrate and their morphological studies were done. Fig.6.4 shows the surface topography and the phase images respectively. A maximum surface roughness of the order of 20 nm was observed. No polymer residue was present on the films, and they had homogeneous phase ($0-4^\circ$) over the scanned area. Liquid alloy instabilities during cooling and nucleates on the polymer surface impart surface roughness of the alloy surface and thus are the sources of enhanced roughness in the surface. This leads to interesting optical effects at the micron scale. Also, the electromagnetic radiation starts interacting with these surface having a roughness in few nanometers to give enhanced local electrical field (localized surface plasmons). The term quality factor (Q_{LSP}) is used to quantify plasmonic behavior of metals. Silver is the best plasmonic metal, having highest quality factor of 97, followed by gold, which has 33. For Aluminum, this value is 11, and it lies around 3-4 for indium and tin. Hence, indium and tin are considered as weakly plasmonic in nature. These metals are suitable for plasmonic enhancement in solar cells due to their low reflection invisible region. This is due to the fact that their resonance frequency lies in UV region.

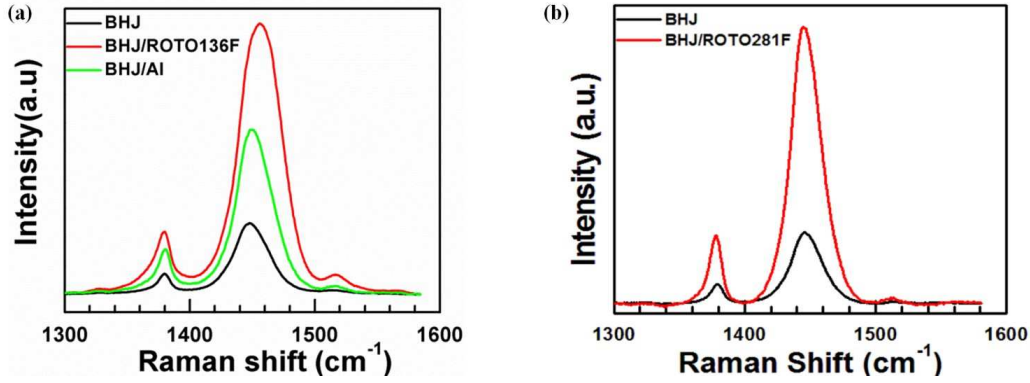


Figure 6.5: a) SERS spectra of P3HT-PCBM only, P3HT-PCBM/Al and P3HT-PCBM/ROTO136F. b) Raman spectra of P3HT-PCBM pristine and P3HT-PCBM with ROTO281F.

BHJ/alloy interface has transparent front electrode in the solar cell configuration. Raman measurements were performed at this interface. Paracetamol was used as standard reference for calibrating all the Raman spectra. Raman spectra of P3HT on only ITO coated glass with and without alloy electrodes were recorded. There was an enhancement in the intensity of the peaks at 1447 cm^{-1} , 1379 cm^{-1} and 1511 cm^{-1} in presence of alloy electrode as compared to that of P3HT on ITO glass without the electrodes. The 1447 cm^{-1} and 1511 cm^{-1} modes are associated with the in phase stretching of C=C conjugated bond in thiophene ring. In surface enhanced Raman scattering the incident laser intensity is enhanced as a function of $|E_{incident}|^2$ and the scattered intensity is enhanced as $|E_{scattered}|^2$ where $|E|$ is the field strength of electromagnetic radiation. Thus, there is a 4 fold increase in the Raman scattering intensity in SERS. Using electromagnetic theory, SERS enhancement factor can be calculated theoretically as:

$$En_{SERS} \approx \left| \frac{E(\omega_{incident})}{E_o(\omega_{incident})} \right|^2 \left| \frac{E(\omega_{scattered})}{E_o(\omega_{scattered})} \right|^2 \quad (6.1)$$

Where $E_o(\omega)$ is the incident electric field and $E(\omega)$ is the field in the presence of

plasmonic medium, $\omega_{incident}$ and $\omega_{scattered}$ are the frequency of excitation and emission respectively. SERS enhancement depends on the distance of the scattering medium from the plasmon source, relative orientation and polarization of electromagnetic radiation. Experimentally, it is calculated using the following relation [107],[108]:

$$EnhancementFactor = \frac{I_{SERS}}{N_{Surf}} \times \frac{N_{bulk}}{I_{norm}} \quad (6.2)$$

Where I_{SERS} and I_{norm} are the intensity of any specific band in SERS and Raman spectra of the analyte molecule. N_{bulk} and N_{surf} gives the number of probe molecules which are illuminated the laser in bulk and SERS experiments respectively.

$$N_{surf} = C \times A \quad (6.3)$$

C is Surface Density A is area of the laser spot

$$N_{bulk} = \frac{Ah\rho}{M} \quad (6.4)$$

h is the penetration depth ρ is density of the sample M is molecular weight of the sample. In our experiment, it was difficult to calculate the number of probe molecules in both Raman and SERS measurements, so the SERS enhancement factors were calculated by taking the ratio of the intensity at a particular band. Intensity at a particular band was calculated by taking area under the Raman band with and without back electrode, i.e., P3HT on only ITO coated glass. Maximum enhancement factor calculated was ~ 4.7 , the actual SERS enhancement will be much higher if the analyte molecule concentration was taken into account. This

enhancement was certainly more than any reflective increase from the electrode but was low as compared to enhancements obtained for P3HT with silver nanoparticles (2-20). The low enhancement can be due to various factors such as inhomogeneous distribution of nanostructures. It has been observed that for getting maximum enhancement with small analyte molecules, the optimum size of nanostructures should be in a range of 40 to 60 nm, whereas in our case it was below 20 nm. Also, silver has highest plasmonic character of all the metals, but the constituent metals in the alloy were indium and tin, and they have very low plasmonic character in comparison to silver. Since the plasmons are localized at the BHJ/alloy interlayer the level of enhancement observed is also proportional to the number of scattering molecules present in the close vicinity of alloy.

In case of Elec1 the 1447 cm^{-1} band and 1511 cm^{-1} band shows a shift towards higher wavenumber by $\sim 12\text{ cm}^{-1}$. Shift in C=C band stretching mode is attributed to increasing in the double bond character; such shift was not observed in the case of Elec2. Since both the bands have contribution from C=C symmetric stretching which suggests the presence of interaction between Elec1 and P3HT core. Exact nature of such interaction has not been clearly understood. Elec1 showed more enhancement in the intensity of Raman bands of P3HT as compared to Elec2. This is possible because Elec1 contains a significant proportion of In. This leads greater plasmonic activity in Elec1 as In is relatively more plasmonic in nature than Sn. The Raman bands at frequencies 1447 cm^{-1} and 1511 cm^{-1} show higher enhancement compared to 1379 cm^{-1} band. So it can be inferred that the effective enhancement in electric field is much localized and is only restricted to a few layers close to the electrode at the surface of BHJ/alloy because the bands at 1447 cm^{-1} and 1511 cm^{-1} arise due to C=C symmetric stretching mode. So there is stronger coupling and higher field enhancement for this mode. As Aluminum

shows higher plasmonic activity so, surface enhanced Raman spectra of P3HT on thermally evaporated Al electrode were done as control experiments. Due to the absence of nanostructures, the SERS enhancement for Aluminum was lower than both the alloys. SERS measurements gave a clear evidence for energy transfer between plasmonic particles and polymer layers. This energy transfer resulted in enhancements in efficiency of polymer solar cells.

A clear evidence of alloy induced SERS enhancement of the C=C stretching is evident in the case of films where a macro instability pattern co-exists forming a periodic structure [Fig.6]. These films highlight the optical features arising from the alloy/BHJ contact regions. Fig.6 indicates the reflection contrast of alloy films arising from the periodic contacts with the active layer. A spatial scan of the SERS measurements indicated the larger enhancement region from the contact regions compared to the noncontact-regions.

It has been shown earlier that the alloys with the BHJ, under optimum conditions, solidify to give ohmic contacts [98]. So, Current - Voltage (I - V) characteristics of the two alloys were studied, and their performances were compared to that of Al. For the case of Elec1, I-V characteristics were comparable to as observed in thermally evaporated Al. Photo current response, under illumination for Elec1 was also comparable to thermally evaporated Al, but for Elec2, there was an increase in J_{SC} while the fill factor and V_{OC} were lower than thermally evaporated Al.

Quantum efficiency measurements (IPCE) were done to determine the plasmonic contribution in the organic solar cell (O_{SC}) device structures. These measurements proved that the enhancement in case of alloy was due to plasmonic contributions from alloy. This was in agreement with the Raman measurements. The details about the same are discussed elsewhere.

Surface textures of micron and submicron scale were observed at the alloy/BHJ

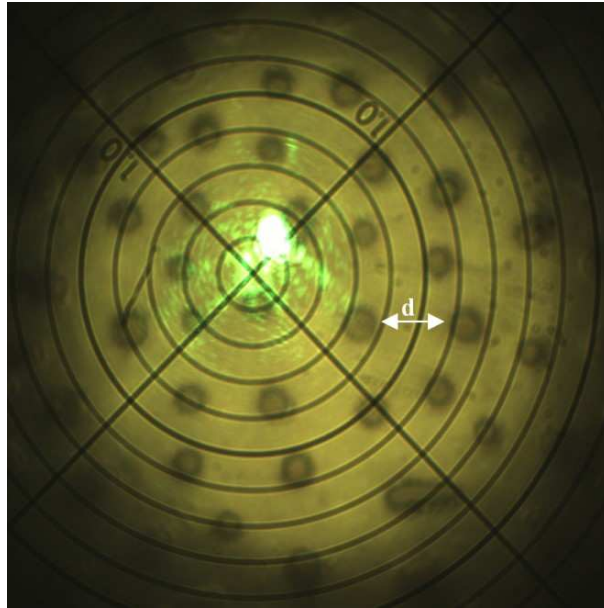


Figure 6.6: Instability mediated patterning at the micron scale on alloy surface

interface in optical and AFM images (Fig.6.4 and Fig.6.6). These texture helps in trapping light, and reducing losses due to reflection. Thus, the low melting alloys provides a low cost texturing technique for metal contacts.

Fig.6.6 shows microstructures which are mostly in a circular shape, the microstructures are distributed in a close to periodic fashion over an area of $250 \mu\text{m}$ by $250 \mu\text{m}$. The diameter of the structure varies from 8-20 microns with the inter structure distance ranging from 15-30 microns with the inter structure distance ranging from 15-30 microns. The lines in concentric circles serve as a scale bar, when viewed through a 50X objective the distance between the two consecutive circles is of the order of 10 microns.

6.4 Conclusions

Facile meltable alloys are potential alternatives to conventional vacuum-deposited thin-film electrodes. These alloy-electrodes are equivalent to Al cathodes in terms of the charge extraction properties. There is an increased optical efficiency in the optical process within the active BHJ layer upon cooling the liquid. These alloys show enhancement in plasmonic features which were confirmed by SERS studies. Surface enhanced Raman studies confirms that origin of plasmonic behavior can be associated with the presence of plasmonic metals (In, Sn, Pb) in the alloys. These metals get amplified due to the presence of surface nanostructure 20 nm at the alloy/BHJ interface. Light trapping effect was also observed at the polymer/alloy interface. This was responsible for efficient performance of Elec1 as a back electrode. There was an effective increase in absorption for both the alloys system due to diffusive scattering of light by the microstructures. These properties of low meltable alloys can be used in manufacturing of solution processed photovoltaic devices.

CHAPTER 7

OUTLOOK

In the recent past, many optical spectroscopic techniques like SERS, SPR, and FRET, have emerged. These techniques have reached single molecular level detection. Molecules can be probed with high resolutions and sensitivity even at extremely low concentrations. Other optical techniques like AFM, can be coupled with these techniques for an increased versatility. Tip enhanced Raman spectroscopy (TERS) is one such example which helps in extracting both topological, as well as chemical information from molecular systems.

Surface-enhanced Raman scattering (SERS) is a very versatile technique with a potential to carry out ultra low detection. It can provide vibrational as well as chemical information about molecular systems. SERS is used for environmental analysis to find toxicity in ground water and concentration of pollutants in the air. It has an edge over many other traditional techniques like fluorescence and chemiluminescence. The advantages like high sensitivity, multiplex detection, robustness and capability of probing molecules in aqueous environments have made SERS a significant tool in protein-molecule binding studies. Techniques like SPR, fluorescence, NMR and X-ray crystallography have some limitations. SERS complements these techniques in studying protein structures, as well as plasmonic features in metals.

Although SERS and SERRS have been effectively employed in various analytical applications, the fundamental physics of SERS as an optical process is yet to be

understood completely. Various groups around the world are trying build effective microscopic models to understand the electromagnetic and chemical enhancement mechanisms. Attempts have been made to define precisely the Raman cross section of molecules exhibiting SERS. Raman cross section of molecules gives insight into the enhanced interaction between molecule and metal. Calculation of absolute enhancement factors is another important issue with SERS. Single molecule SERS signals can be observed from enhancement factors of 10^7 , although there is literature which predicts that enhancement factors of 10^{14} are required for single molecule SERS. Anti-Stokes and Stokes Raman spectra can be analysed to study second enhancement in surface-enhanced resonance Raman scattering.

There are various issues in SERS, which have to be addressed in future. The rational design and fabrication of SERS hot-spot, effective coupling of magnetic properties of nanoparticle to their surface plasmon resonances, micro-fluidic instrumentation for SERS applications, Raman imaging of sub-cellular components are few of the examples which have direct or indirect implications in various analytical applications. Fabricating SERS substrates by both top-down and bottom-up approaches are needed to be addressed with greater concern. All these issues with SERS can be circumvented in the future, with the help of developing technology and better understanding of physical and chemical processes at the nanoscale.

Despite many hurdles, SERS is rapidly growing into practical research tool for detection. SERS has enormous potential to probe various aspects of materials and molecules alike.

References

- [1] L. Rayleigh, *XXXIV. On the transmission of light through an atmosphere containing small particles in suspension, and on the origin of the blue of the sky*, The London, Edinburgh, and Dublin Philosophical Magazine and Journal of Science **47**, 375 (1899).
- [2] C. V. Raman and K. S. Krishnan, *A new type of secondary radiation*, Nature **121**, 501 (1928).
- [3] L. Mandelstam and G. Landsberg, *Eine neue Erscheinung bei der Lichtzerstreuung in Kristallen*, Naturwissenschaften **16**, 557 (1928).
- [4] C. V. Raman, *A change of wave-length in light scattering*, Nature **121**, 619 (1928).
- [5] M. Fleischmann, P. J. Hendra, and A. J. McQuillan, *Raman spectra of pyridine adsorbed at a silver electrode*, Chem. Phys. Lett. **26**, 163 (1974).
- [6] D. A. Long, *Raman spectroscopy*, New York 1 (1977).
- [7] G. Placzek, *The Rayleigh and Raman Scattering* (Lawrence Radiation Laboratory, , 1959), Vol. 526.

- [8] P. A. Dirac, in *Proceedings of the Royal Society of London A: Mathematical, Physical and Engineering Sciences*, The Royal Society (, , 1927), No. 767, pp. 243–265.
- [9] M. G. Albrecht and J. A. Creighton, *Anomalously intense Raman spectra of pyridine at a silver electrode*, *Journal of the American Chemical Society* **99**, 5215 (1977).
- [10] D. L. Jeanmaire and R. P. Van Duyne, *Surface Raman spectroelectrochemistry: Part I. Heterocyclic, aromatic, and aliphatic amines adsorbed on the anodized silver electrode*, *Journal of Electroanalytical Chemistry and Interfacial Electrochemistry* **84**, 1 (1977).
- [11] P. L. Stiles, J. A. Dieringer, N. C. Shah, and R. P. Van Duyne, *Surface-enhanced Raman spectroscopy*, *Annu. Rev. Anal. Chem.* **1**, 601 (2008).
- [12] E. J. Zeman and G. C. Schatz, *An accurate electromagnetic theory study of surface enhancement factors for silver, gold, copper, lithium, sodium, aluminum, gallium, indium, zinc, and cadmium*, *Journal of Physical Chemistry* **91**, 634 (1987).
- [13] K. Kneipp *et al.*, *Single molecule detection using surface-enhanced Raman scattering (SERS)*, *Physical review letters* **78**, 1667 (1997).
- [14] S. Nie and S. R. Emory, *Probing single molecules and single nanoparticles by surface-enhanced Raman scattering*, *science* **275**, 1102 (1997).
- [15] A. Campion and P. Kambhampati, *Surface-enhanced Raman scattering*, *Chem. Soc. Rev.* **27**, 241 (1998).

- [16] M. N. Siamwiza *et al.*, *Interpretation of the doublet at 850 and 830 cm⁻¹ in the Raman spectra of tyrosyl residues in proteins and certain model compounds*, *Biochemistry* **14**, 4870 (1975).
- [17] S. Krimm and J. Bandekar, *Vibrational spectroscopy and conformation of peptides, polypeptides, and proteins*, *Advances in protein chemistry* **38**, 181 (1986).
- [18] A. Barth and C. Zscherp, *What vibrations tell about proteins*, *Quarterly reviews of biophysics* **35**, 369 (2002).
- [19] G. P. Kumar and C. Narayana, *Adapting a fluorescence microscope to perform surface enhanced*, *Current science* **93**, (2007).
- [20] P. Lee and D. Meisel, *Adsorption and surface-enhanced Raman of dyes on silver and gold sols*, *The Journal of Physical Chemistry* **86**, 3391 (1982).
- [21] M.-E. Aubin-Tam and K. Hamad-Schifferli, *Structure and function of nanoparticle-protein conjugates*, *Biomedical Materials* **3**, 034001 (2008).
- [22] A. Hédoux, Y. Guinet, and L. Paccou, *Analysis of the mechanism of lysozyme pressure denaturation from Raman spectroscopy investigations, and comparison with thermal denaturation*, *The Journal of Physical Chemistry B* **115**, 6740 (2011).
- [23] D. Kurouski *et al.*, *Amide I vibrational mode suppression in surface (SERS) and tip (TERS) enhanced Raman spectra of protein specimens*, *Analyst* **138**, 1665 (2013).
- [24] S. Hazra, A. Gibaud, and C. Sella, *Tunable absorption of Au-Al₂O₃ nanocermet thin films and its morphology*, *Applied Physics Letters* **85**, 395 (2004).

- [25] J. Toudert *et al.*, *Morphology and surface-plasmon resonance of silver nanoparticles sandwiched between Si_3N_4 and BN layers*, Journal of applied physics **98**, 114316 (2005).
- [26] S. Cho *et al.*, *Microstructural effect on optical properties of Au: SiO_2 nanocomposite waveguide films*, Journal of Applied Physics **102**, 123501 (2007).
- [27] J. Okumu *et al.*, *Photochromic silver nanoparticles fabricated by sputter deposition*, Journal of applied physics **97**, 094305 (2005).
- [28] T. Klar *et al.*, *Surface-plasmon resonances in single metallic nanoparticles*, Physical Review Letters **80**, 4249 (1998).
- [29] S. Peng *et al.*, *Reversing the size-dependence of surface plasmon resonances*, Proceedings of the National Academy of Sciences **107**, 14530 (2010).
- [30] K. Kneipp *et al.*, *Single molecule detection using surface-enhanced Raman scattering (SERS)*, Physical review letters **78**, 1667 (1997).
- [31] F. Svedberg, Z. Li, H. Xu, and M. Käll, *Creating hot nanoparticle pairs for surface-enhanced Raman spectroscopy through optical manipulation*, Nano letters **6**, 2639 (2006).
- [32] J. A. Fan *et al.*, *Self-assembled plasmonic nanoparticle clusters*, science **328**, 1135 (2010).
- [33] N. A. Abu Hatab, J. M. Oran, and M. J. Sepaniak, *Surface-enhanced Raman spectroscopy substrates created via electron beam lithography and nanotransfer printing*, Acs Nano **2**, 377 (2008).

- [34] B. D. Piorek *et al.*, *Free-surface microfluidic control of surface-enhanced Raman spectroscopy for the optimized detection of airborne molecules*, Proceedings of the National Academy of Sciences **104**, 18898 (2007).
- [35] E. Hutter and J. H. Fendler, *Exploitation of localized surface plasmon resonance*, Advanced Materials **16**, 1685 (2004).
- [36] C. Fernández-López *et al.*, *Highly Controlled Silica Coating of PEG-Capped Metal Nanoparticles and Preparation of SERS-Encoded Particles*, Langmuir **25**, 13894 (2009).
- [37] M. Jin *et al.*, *Shape-Controlled Synthesis of Copper Nanocrystals in an Aqueous Solution with Glucose as a Reducing Agent and Hexadecylamine as a Capping Agent*, Angewandte Chemie International Edition **50**, 10560 (2011).
- [38] H.-H. Cheng *et al.*, *Light trapping enhancements of inverted pyramidal structures with the tips for silicon solar cells*, Applied Physics Letters **101**, 141113 (2012).
- [39] G. Baraldi *et al.*, *Preventing the degradation of Ag nanoparticles using an ultrathin α -Al₂O₃ layer as protective barrier*, The Journal of Physical Chemistry C **117**, 9431 (2013).
- [40] S. P. Garcia, H. Bao, and M. A. Hines, *Etchant anisotropy controls the step bunching instability in KOH etching of silicon*, Physical review letters **93**, 166102 (2004).
- [41] H. Brune, *Microscopic view of epitaxial metal growth: nucleation and aggregation*, Surface Science Reports **31**, 125 (1998).

- [42] A. Kudelski, *Raman studies of rhodamine 6G and crystal violet sub-monolayers on electrochemically roughened silver substrates: Do dye molecules adsorb preferentially on highly SERS-active sites?*, Chemical physics letters **414**, 271 (2005).
- [43] P. Peng, K.-J. Ling, and W. Tse, *SERS of crystal violet in sandblast roughened silver surface*, Modern Physics Letters B **4**, 531 (1990).
- [44] N. Gupta *et al.*, *Thermally stable plasmonic nanocermets grown on micro-engineered surfaces as versatile SERS sensors for multi-analyte detection*, ACS applied materials & interfaces (2014).
- [45] X. Bao, M. Muhler, T. Schedel-Niedrig, and R. Schlögl, *Interaction of oxygen with silver at high temperature and atmospheric pressure: A spectroscopic and structural analysis of a strongly bound surface species*, Physical Review B **54**, 2249 (1996).
- [46] H. Bi *et al.*, *Optical study of redox process of Ag nanoparticles at high temperature*, Journal of applied physics **92**, 7491 (2002).
- [47] B. Balamurugan and T. Maruyama, *Evidence of an enhanced interband absorption in Au nanoparticles: Size-dependent electronic structure and optical properties*, Applied Physics Letters **87**, 143105 (2005).
- [48] J. A. Thornton, *High rate thick film growth*, Annual review of materials science **7**, 239 (1977).
- [49] P. K. Jain, X. Huang, I. H. El-Sayed, and M. A. El-Sayed, *Noble metals on the nanoscale: optical and photothermal properties and some applications in*

- imaging, sensing, biology, and medicine*, Accounts of Chemical Research **41**, 1578 (2008).
- [50] K. L. Kelly, E. Coronado, L. L. Zhao, and G. C. Schatz, *The optical properties of metal nanoparticles: the influence of size, shape, and dielectric environment*, The Journal of Physical Chemistry B **107**, 668 (2003).
- [51] P. L. Stiles, J. A. Dieringer, N. C. Shah, and R. P. Van Duyne, *Surface-enhanced Raman spectroscopy*, Annu. Rev. Anal. Chem. **1**, 601 (2008).
- [52] K. Kneipp *et al.*, *Single molecule Raman detection of enkephalin on silver colloidal particles*, Journal of Spectroscopy **18**, 433 (2004).
- [53] Y. X. Yeng *et al.*, *Enabling high-temperature nanophotonics for energy applications*, Proceedings of the National Academy of Sciences **109**, 2280 (2012).
- [54] T. Chen, C. Kuo, Y. Chou, and N. Liang, *Surface-enhanced Raman scattering of adenosine triphosphate molecules*, Langmuir **5**, 887 (1989).
- [55] T. Kang *et al.*, *Patterned multiplex pathogen DNA detection by Au particle-on-wire SERS sensor*, Nano letters **10**, 1189 (2010).
- [56] G. von Maltzahn *et al.*, *SERS-coded gold nanorods as a multifunctional platform for densely multiplexed near-infrared imaging and photothermal heating*, Advanced Materials **21**, 3175 (2009).
- [57] E. KyuáLee *et al.*, *Fabrication of SERS-fluorescence dual modal nanoprobe and application to multiplex cancer cell imaging*, Nanoscale **4**, 124 (2012).
- [58] L. Polavarapu *et al.*, *Alkylamine capped metal nanoparticle inks for printable SERS substrates, electronics and broadband photodetectors*, Nanoscale **3**, 2268 (2011).

- [59] Y. S. Hu *et al.*, *Enhanced raman scattering from nanoparticle-decorated nanocone substrates: A practical approach to harness in-plane excitation*, ACS nano **4**, 5721 (2010).
- [60] H. Liang *et al.*, *Highly Surface-roughened Flower-like Silver Nanoparticles for Extremely Sensitive Substrates of Surface-enhanced Raman Scattering*, Advanced Materials **21**, 4614 (2009).
- [61] M. D. Thoreson *et al.*, *Fabrication and realistic modeling of three-dimensional metal-dielectric composites*, Journal of Nanophotonics **5**, 051513 (2011).
- [62] K.-H. Su *et al.*, *Interparticle coupling effects on plasmon resonances of nanogold particles*, Nano Letters **3**, 1087 (2003).
- [63] H. M. Lee, S. M. Jin, H. M. Kim, and Y. D. Suh, *Single-molecule surface-enhanced Raman spectroscopy: a perspective on the current status*, Physical Chemistry Chemical Physics **15**, 5276 (2013).
- [64] P. R. Carey, *Raman spectroscopy, the sleeping giant in structural biology, awakes*, Journal of Biological Chemistry **274**, 26625 (1999).
- [65] A. Barth and C. Zscherp, *What vibrations tell about proteins*, Quarterly reviews of biophysics **35**, 369 (2002).
- [66] J. Z. Zhang and C. Noguez, *Plasmonic optical properties and applications of metal nanostructures*, Plasmonics **3**, 127 (2008).
- [67] , .
- [68] W. A. El-Said, T.-H. Kim, Y.-H. Chung, and J.-W. Choi, *Fabrication of new single cell chip to monitor intracellular and extracellular redox state based on spectroelectrochemical method*, Biomaterials **40**, 80 (2015).

- [69] G. P. Kumar *et al.*, *Surface-enhanced Raman scattering studies of human transcriptional coactivator p300*, *Journal of Physical Chemistry B* **110**, 16787 (2006).
- [70] G. P. Kumar *et al.*, *Surface-enhanced Raman spectroscopic studies of coactivator-associated arginine methyltransferase 1*, *The Journal of Physical Chemistry B* **112**, 6703 (2008).
- [71] S. Siddhanta *et al.*, *Surface enhanced Raman spectroscopy of Aurora kinases: direct, ultrasensitive detection of autophosphorylation*, *RSC Advances* **3**, 4221 (2013).
- [72] H.-N. Hou *et al.*, *Studies on interaction between Vitamin B12 and human serum albumin*, *Journal of pharmaceutical and biomedical analysis* **47**, 134 (2008).
- [73] T. Lemma and J. Pawliszyn, *Human serum albumin interaction with oxaliplatin studied by capillary isoelectric focusing with the whole column imaging detection and spectroscopic method*, *Journal of pharmaceutical and biomedical analysis* **50**, 570 (2009).
- [74] E. Jantratid, N. Janssen, C. Reppas, and J. B. Dressman, *Dissolution media simulating conditions in the proximal human gastrointestinal tract: an update*, *Pharmaceutical research* **25**, 1663 (2008).
- [75] S. Stewart and P. Fredericks, *Surface-enhanced Raman spectroscopy of peptides and proteins adsorbed on an electrochemically prepared silver surface*, *Spectrochimica Acta Part A: Molecular and Biomolecular Spectroscopy* **55**, 1615 (1999).

- [76] E. Podstawka, Y. Ozaki, and L. M. Proniewicz, *Part I: Surface-enhanced Raman spectroscopy investigation of amino acids and their homodipeptides adsorbed on colloidal silver*, Applied spectroscopy **58**, 570 (2004).
- [77] E. Podstawka, Y. Ozaki, and L. M. Proniewicz, *Part III: Surface-enhanced Raman scattering of amino acids and their homodipeptide monolayers deposited onto colloidal gold surface*, Applied spectroscopy **59**, 1516 (2005).
- [78] C. Gullekson, L. Lucas, K. Hewitt, and L. Kreplak, *Surface-sensitive Raman spectroscopy of collagen I fibrils*, Biophysical journal **100**, 1837 (2011).
- [79] I. Razmutė-Razmė, Z. Kuodis, O. Eicher-Lorka, and G. Niaura, *In-situ surface-enhanced Raman spectroscopic investigation of NH site of indole ring-terminated self-assembled monolayer on gold electrode*, Chemija **18**, 16 (2007).
- [80] C. M. Dupureur, *One is enough: insights into the two-metal ion nuclease mechanism from global analysis and computational studies*, Metallomics **2**, 609 (2010).
- [81] C. M. Dupureur, *Roles of metal ions in nucleases*, Current opinion in chemical biology **12**, 250 (2008).
- [82] A. Pingoud, M. Fuxreiter, V. Pingoud, and W. Wende, *Type II restriction endonucleases: structure and mechanism*, Cellular and molecular life sciences **62**, 685 (2005).
- [83] L. M. Bowen and C. M. Dupureur, *Investigation of restriction enzyme cofactor requirements: a relationship between metal ion properties and sequence specificity*, Biochemistry **42**, 12643 (2003).

- [84] K. Vasu, M. Saravanan, and V. Nagaraja, *Endonuclease Active Site Plasticity Allows DNA Cleavage with Diverse Alkaline Earth and Transition Metal Ions*, ACS chemical biology **6**, 934 (2011).
- [85] S. Chandrashekar, M. Saravanan, D. R. Radha, and V. Nagaraja, *Ca²⁺-mediated site-specific DNA cleavage and suppression of promiscuous activity of KpnI restriction endonuclease*, Journal of Biological Chemistry **279**, 49736 (2004).
- [86] K. Vasu, E. Nagamalleswari, and V. Nagaraja, *Promiscuous restriction is a cellular defense strategy that confers fitness advantage to bacteria*, Proceedings of the National Academy of Sciences **109**, E1287 (2012).
- [87] E. Nagamalleswari, K. Vasu, and V. Nagaraja, *Ca²⁺ Binding to the ExDxD Motif Regulates the DNA Cleavage Specificity of a Promiscuous Endonuclease*, Biochemistry **51**, 8939 (2012).
- [88] S. Chandrashekar, P. Babu, and V. Nagaraja, *Characterization of DNA binding activities of over-expressed KpnI restriction endonuclease and modification methylase*, Journal of Biosciences **24**, 269 (1999).
- [89] H. Deng *et al.*, *The study of Turnip Mosaic virus coat protein by surface enhanced Raman spectroscopy*, Spectrochimica Acta Part A: Molecular Spectroscopy **49**, 1709 (1993).
- [90] A. Campion and P. Kambhampati, *Surface-enhanced Raman scattering*, Chem. Soc. Rev. **27**, 241 (1998).
- [91] M. Moskovits and J. Suh, *Surface selection rules for surface-enhanced Raman spectroscopy: calculations and application to the surface-enhanced Raman*

- spectrum of phthalazine on silver*, The Journal of Physical Chemistry **88**, 5526 (1984).
- [92] K. Kneipp *et al.*, *Surface-enhanced Raman scattering and biophysics*, Journal of Physics: Condensed Matter **14**, R597 (2002).
- [93] S. Siddhanta *et al.*, *Surface enhanced Raman spectroscopy of Aurora kinases: direct, ultrasensitive detection of autophosphorylation*, RSC Advances **3**, 4221 (2013).
- [94] S. Liu *et al.*, *High-efficiency polymer solar cells via the incorporation of an amino-functionalized conjugated metallopolymer as a cathode interlayer*, Journal of the American Chemical Society **135**, 15326 (2013).
- [95] Z. He *et al.*, *Enhanced power-conversion efficiency in polymer solar cells using an inverted device structure*, Nature Photonics **6**, 591 (2012).
- [96] M. A. Green *et al.*, *Solar cell efficiency tables (Version 45)*, Progress in photovoltaics: research and applications **23**, 1 (2015).
- [97] D. Gupta, M. Bag, and K. Narayan, *Area dependent efficiency of organic solar cells*, Applied Physics Letters **93**, 163301 (2008).
- [98] D. Gupta, M. Bag, and K. Narayan, *Correlating reduced fill factor in polymer solar cells to contact effects*, Applied Physics Letters **92**, 093301 (2008).
- [99] W.-I. Jeong *et al.*, *Reduction of collection efficiency of charge carriers with increasing cell size in polymer bulk heterojunction solar cells*, Advanced Functional Materials **21**, 343 (2011).
- [100] S. Choi, W. J. Potscavage Jr, and B. Kippelen, *Area-scaling of organic solar cells*, Journal of Applied Physics **106**, 054507 (2009).

- [101] A. J. Das and K. Narayan, *Retention of Power Conversion Efficiency—From Small Area to Large Area Polymer Solar Cells*, *Advanced Materials* **25**, 2193 (2013).
- [102] K. Catchpole and A. Polman, *Plasmonic solar cells*, *Optics express* **16**, 21793 (2008).
- [103] C. F. Guo *et al.*, *Metallic nanostructures for light trapping in energy-harvesting devices*, *Light: Science & Applications* **3**, e161 (2014).
- [104] T. Temple, G. Mahanama, H. Reehal, and D. Bagnall, *Influence of localized surface plasmon excitation in silver nanoparticles on the performance of silicon solar cells*, *Solar Energy Materials and Solar Cells* **93**, 1978 (2009).
- [105] X. Liu *et al.*, *Elucidating the Localized Plasmonic Enhancement Effects from a Single Ag Nanowire in Organic Solar Cells*, *ACS nano* **8**, 10101 (2014).
- [106] A. P. Kulkarni *et al.*, *Plasmon-enhanced charge carrier generation in organic photovoltaic films using silver nanoprisms*, *Nano letters* **10**, 1501 (2010).
- [107] S. Siddhanta, V. Thakur, C. Narayana, and S. Shivaprasad, *Universal metal-semiconductor hybrid nanostructured SERS substrate for biosensing*, *ACS applied materials & interfaces* **4**, 5807 (2012).
- [108] S. Mohapatra *et al.*, *Facile and green synthesis of SERS active and ferromagnetic silver nanorods*, *European Journal of Inorganic Chemistry* **2010**, 4969 (2010).